UNIVERSIDAD CARLOS III DE MADRID
ESCUELA POLITÉCNICA SUPERIOR

Modeling and simulation of a train of kites

Bachelor Thesis

Author
Jose Antonio Serrano Iglesias

Supervisor
Gonzalo Sánchez Arriaga

Leganés, June 2018

Department of Aerospace Engineering
ESCUELA POLITÉCNICA SUPERIOR

Modeling and simulation of a train of kites

Bachelor in Aerospace Engineering

Author
Jose Antonio Serrano Iglesias

Supervisor
Gonzalo Sánchez Arriaga

Leganés, June 2018

Abstract

Nowadays, the greater and greater worldwide population growth combined with the evident drying up of the conventional no renewable energy sources, and the continuous growing global conciliation about searching clean renewable energies, is continuously triggering an exhaustive research of even more advanced and competitive energy extraction technologies. Airborne Wind Energy appears as a new and sophisticated concept in the matter of the renewables, based on harvesting energy from high winds.

This work proposes a dynamical model of a an AWE system, composed by a vertical train of two-line kites attached to the ground. The Lagrangian formulation is used for the obtainment of the equations of motion of the system, yielding a low-order system of ordinary differential equations. The unmanned dynamical response of the system is evluated around its equilibrium position by deploying an exhaustive analysis of the normal modes of the system.

Contents

List of Figures

List of Tables

Nomenclature

Acronyms

AWE	Airborne Wind Energy
AWES	Airborne Wind Energy System
GLG	Ground-Level Generator
GS	Ground Station
IMU	Inertial Measurement Unit
KSU	Kite Steering Unit
LCOE	Levelized Cost Of Energy
OBG	Onboard Generator
TPED	Total Primary Energy Demand

Subscripts

A	point $A^{\pm}$
B	Body frame
C	point $C^{\pm}$
E	Earth frame
G	center of mass
i	state vector variables index
k	kite index
n, i, j	frames of reference indexes
x, y, z	respective coordinates

Symbols

α	angle of attack, [rad]
$\bar{\boldsymbol{\iota}}$	dimensionless moment of inertia tensor, [−]
$\bar{\mathbf{\Phi}}$	angular velocity matrix, [−]

$\bar{\boldsymbol{\Upsilon}}$	linear velocity matrix, [m]
$\bar{\boldsymbol{I}}$	moment of inertia tensor, $\left[\mathrm{kg} \cdot \mathrm{m}^2\right]$
$\bar{\boldsymbol{R}}$	rotation matrix, [−]
β	sideslip angle, [rad]
ℓ	dimensionless line length, [−]
γ, θ	longitudinal state angles, [rad]
$\mathcal{L}$	Lagrangian function
ω_n	natural frequency, $\left[\mathrm{rad} \cdot \mathrm{s}^{-1}\right]$
$\boldsymbol{\Omega}$	angular velocity vector, $\left[^\circ \cdot \mathrm{s}^{-1}\right]$
$\boldsymbol{\omega}$	dimensionless angular velocity vector, $\left[\mathrm{rad} \cdot \sqrt{\mathrm{g/L_1}}\right]$
$\boldsymbol{F}^A$	aerodynamic forces, $\left[\mathrm{kg} \cdot \mathrm{m} \cdot \mathrm{s}^{-2}\right]$
$\boldsymbol{f}^A$	dimensionless aerodynamic forces, [−]
$\boldsymbol{i}, \boldsymbol{j}, \boldsymbol{k}$	unitary vectors in x, y and z directions
$\boldsymbol{J}$	Jacobian matrix
$\boldsymbol{M}$	tensor from Eq. 2.40, [−]
$\boldsymbol{M}^A$	aerodynamic torque about center of mass, $\left[\mathrm{kg} \cdot \mathrm{m}^2 \cdot \mathrm{s}^{-2}\right]$
$\boldsymbol{m}^A$	dimensionless aerodynamic torque about center of mass, [−]
$\boldsymbol{r}$	position vector, [m]
$\boldsymbol{t}$	dimensionless tether tensions, [−]
$\boldsymbol{u}$	extended state vector, $\left[\mathrm{rad}, \mathrm{rad} \cdot \mathrm{s}^{-1}\right]$
$\boldsymbol{v}$	linear velocity vector, $\left[\mathrm{m} \cdot \mathrm{s}^{-1}\right]$
$\boldsymbol{v}^A$	aerodynamic velocity vector, $\left[\mathrm{m} \cdot \mathrm{s}^{-2}\right]$
$\boldsymbol{v}_w$	wind velocity vector, $\left[\mathrm{kg} \cdot \mathrm{m}^{-2}\right]$
$\boldsymbol{x}_s$	state vector [rad]
ρ	air density, $\left[\mathrm{kg} \cdot \mathrm{m}^{-3}\right]$
σ	dimensionless kite mass, [−]
τ	dimensionless time, [−]
φ, η	lateral state angles, [rad]
ζ	damping ratio, [−]
$A^{\pm}$	attachment points for $\{k\}$-tethers
b	span of the wing, [m]

c	chord of the wing, [m]
$C^{\pm}$	attachment points for $\{k+1\}$-tethers
e_k	dimensionless kinetic energy, [−]
e_p	dimensionless potential energy, [−]
G	center of gravity
g	gravitational acceleration, $\left[\mathrm{m}\cdot\mathrm{s}^{-2}\right]$
L	line length, [m]
m	kite mass, [kg]
N_k	number of kites
N_{half}	cycles to halve, [−]
O	origin of coordinates
P, Q, R	components of the angular velocity in roll, pitch and yaw $\left[^{\circ}\cdot\mathrm{s}^{-1}\right]$
Q	dimensionless generalized forces, [−]
S	surface of the wing, $\left[\mathrm{m}^2\right]$
T	period, [s]
t	time, [s]
t_{half}	time to halve, [s]
V_T	reference velocity, $\left[\mathrm{m}\cdot\mathrm{s}^{-2}\right]$

Superscripts

k	kite index
T	transpose matrix

Chapter 1

Introduction

1.1 Fossil fuels and renewable energy sources

Nowadays, the actual world energy situation represents a most of the serious problems on a global scale, being the climate change one of the main concerns of our time. Numerous investigations state about the fact, that the Earth average temperature has been continuous rising every year during the last decades. One of the main pillars of those current studies is the evidence that the North Pole has been reduced to the half of that it used to be 50 years ago.

Climate cycles, known as natural cycles, have been presented in our planet since several millenials ago. They essentially have explained the course followed by the ice ages and warming periods that have been occurred periodically in the past. Although these cycles are responsible in some manner of the actual global warming, they do not explain the huge change suffered in the average planet temperature for a few years. Obviously, these facts brought society to believe that human impact is the main reason boosting these worrisome changes.

Currently, and probably in the near future, due to the relative low prices and production costs, fossil fuels are and will be the main sources used for energy extraction. Today, fossil sources supply about 80% of TPED and although they are produced for a determined restricted number of countries, emerging countries like China and India are increasing their demand of primary energy, thus projecting an expected increase in that value by 50% in the next 20 years [8]. Figure 1.1 the global primary energy supply in the past decade, when it relied on less than 15% of renewable energy resources.

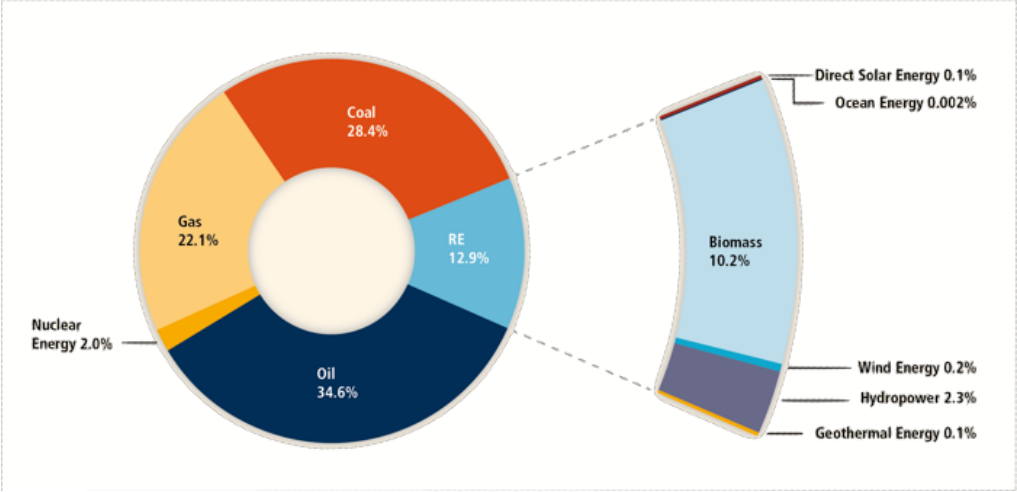

Figure 1.1: Shares of energy sources in total global primary energy supply in 2008. Image from [15].

The threat of availability and environmental risks of fossil fuels have promoted that governments around the world adopt plans and regulations with the aim of reaching “energy security”, improving the sustainability of renewable energy sources and limiting the emissions of greenhouse gases. The two ways followed to reach these goals are: to improve the energy use efficiency and; to

strengthen the shares of renewable energy sources (see [8]). In this way, together with programs aimed to spread the usage of actual renewable energy sources, working on improving their competitiveness against fossil fuels, new "high-impact" renewable energy technological concepts are and have been continuously triggered. Some examples of such efforts are the US Dept. of Energy's ARPA-E agency, the EU Future Emerging Technologies for Energy program as cited in [8] or the Paris Climate Agreement where 195 countries works together for limiting global warming.

Today, environmental and social costs due to innovative renewables and conventional fuels head in opposite directions. While the price of fossil fuels are, and has been fluctuating along the time during decades, renewable energy costs have been reduced sbstantially, continuing to drop at nowadays. Furthermore, the usage of renewables allows to increase the diversity in energy supply markets, mainly covered by fossil fuels; to secure long term sustainable energy sources; to reduce local and global atmospheric emissions and; to provide attractive options to meet specific energy needs.

Source	Minimal estimated ($/MWh)	Maximal estimated ($/MWh)	Average estimated ($/MWh)
Coal	25	50	34
Gas	37	60	47
Nuclear	21	31	29
Wind	35	95	57
Solar	180	500	325
AWE	10	48	20

Table 1.1: Projected cost in 2030 (levelized in 2003) of energy from different sources (data from [8]).

All these facts have triggered many different types of renewable sources since the end of the past century. Among all of them, hydropower, actually accounting for 2% of TPED and almost 16% of the global electricity generation, is the most used one. However, an important inconvenient of hydropower is due to its relative small potential to grow, being the majority of potential sites already exploited. In contrast, as explained in [8], accounting with a growing annual rate of almost 30% in installed capacity and a yearly total investment of more than 50% of the global investment in renewables, wind power is one of the fastest growing renewable energy technologies.

1.2 An introduction to the wind energy

Apart from hydropower, wind industry presents the largest source of renewable energy. Nowadays, although for some many countries the wind power results a pillar in their energy strategies, in a very amount of places, when compared with the relative low cost of energy from coal-power plants, the inflated costs make wind energy to be an inaccessible resource. Concretely, at the end of 2017, it was estimated that all the wind turbines installed around the world, only cover an almost 5% of the global electricity demand.

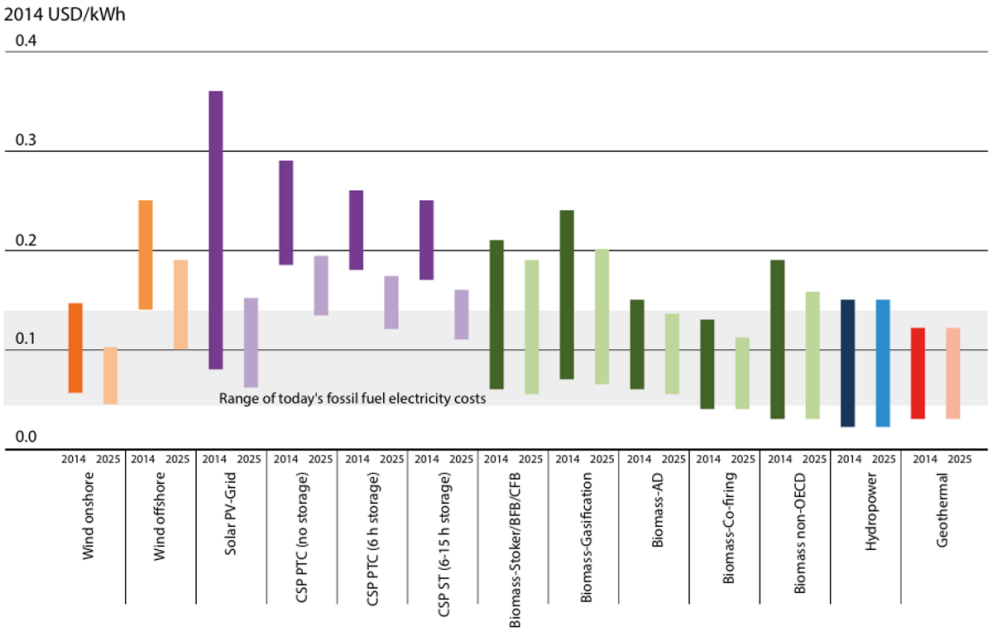

Figure 1.2: LCOE of global renewable energy technologies, 2014 and 2025. Courtesy of [16].

Recent studies and investigations have stated that using only a 20% of the world land sites conceived for the exploitation of actual wind towers technology, the global energy demand could be supplied [9]. At Fig.1.2, the LCOE (USD/kWh) shows that the wind energy generation is one of the cheapest current renewable energies, resulting practically the total cost referred to this type of energy to the construction effort.

However, the actual wind technology presents clear limitations that results too high when comparing with other energy important resources. One of the current wind energy relevant issues has to do with land occupation. Several studies (see [9]) reveals that for generating the same amount of energy, the actual $2-3$ MW rated power tower-based wind farms, presenting an average power density of 3.5–4 MW/km^2, require for almost 200–300 times the land occupied by the large thermal plants.

Together with land sites occupation, another important conventional wind energy disadvantage is due to its relative low efficiency for extracting energy. As stated some lines above, the wind energy is one of the cheapest actual renewables, essentially basing its total costs in the construction effort. The tower turbines structure establish most of the costs, but also impose some restrictions and limitations at the time of extracting energy.

On one hand, since the current conventionaly used tower turbines are based on extracting energy throughout the blades rotation, the outermost part of the blades are practically the unique parts involving energy generation. Concretely, the 80% of the wind energy based generated power is only covered by the outermost 30% of the blades surface. Obviously, the reason is that the effective wind speed is higher at the blade outer part and the generated power grows with the cube of the wind speed.

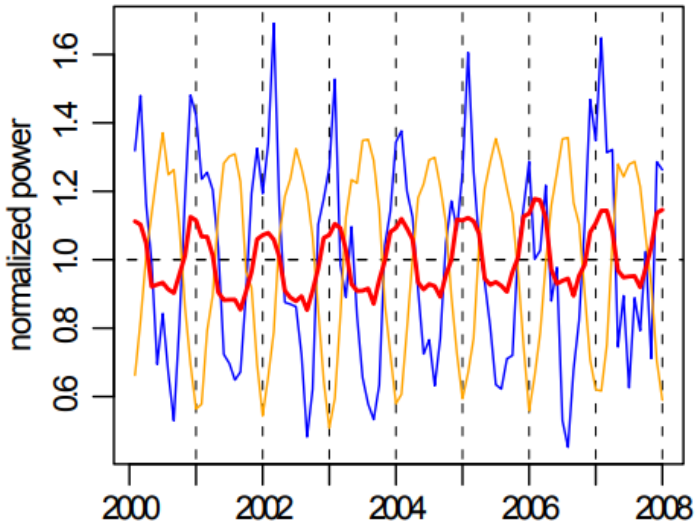

Figure 1.3: Wind energy (blue), solar energy (orange) and total energy consumed in Europe (red) normalized power. The figure shows how wind energy is available mostly in winter, while solar energy in summer. Image from [10].

On the other hand, the towers structure obviously also limit the elevation for the wind harvest. At the ground, the winds are relatively slow when compared with the ones at high altitudes. As covered in [5], the developer of the "ladder-mill" Wubbo Ockels stated, "the wind energy density at 10 km altitude could reach up to 5 MW/km^2". However, to build up a system capable of operating at at an altitude of 10 km for generating electricity from wind can result of extremely high difficulty. Conventional wind turbines operate at about 150 m of altitude. At this altitude, the mean wind power density only covers about the 25% of the one at 1000 m, and only the 2.5% of the one gets at an altitude of 10 km.

Renewable enrgy technologies must demonstrate to result long term power resources as well as low maintainamce costs. Then, although wind energy presents a relative low cost when compared with other energy strategies, the enormous economic effort needed to build up the systems required for the energy extraction together with its relative small efficiency, make to conclude that conventional wind turbines alone might not be the most suitable alternative for clean energy.

Airborne Wind Energy appears as a solution to these problems that conventional wind energy systems present, and thus to increase the wind energy productivity. Essentially, an AWE system is characterized by having a high power-to-mass ratio, high capacity factor and lower installation costs with respect to the ordinary wind turbines.

1.3 Airborne Wind Energy

Airborne wind energy systems are a very promising branch of the wind energy field that deals with airborne devices designed to harvest wind from higher altitudes than conventional wind turbines

by extracting kinetic energy from the wind. Generally, at these altitudes, the wind is stronger and steadier, allowing to capture more energy with higher capacities than conventional wind energy systems; that is the reason why this technology is considered as a good addition to renewable energy systems.

1.3.1 Historical background

The idea of harvesting energy from the high altitude winds comes from centuries back. During the energy crisis in 1970, strong attention was pointed to renewables, being the idea of extracting energy from high altitude winds again revised. In fact, the majority of the ideas which today has been and are continuously implemented in the context of the AWES, were already collected in so many publications in the 70s.

Figure 1.4: Prototype testing the flying electric generators in Australia in May 1986 (Photo by Bryan Roberts, provided by [1]).

In parallel, the well known wind turbines have been developed during the last decades, becoming one of the most succesfull renewable energy harvester system. However, the recent technical and theoretical advances obtained in the field of the AWE technology, summed up to the celebrated series of international conferences together with the fundation of institutions and organizations like the Airborne Wind Energy Consortium, the wind energy industry has started to develop again an important interest about the airborne energy. A big amount of high-tech companies, universities and academic research groups (see Fig. 1.4) have currently developed numerous small-scale prototypes for testing projects and proposed several technologies to harness the power also for naval propulsion and for offshore electric energy generation.

Nowadays, although the the viability of the concept is continuously increasing, several issues remain searching to be solved in order to determine that this technology could be scaled up to an industrial size, principally for meeting the requirements needed and providing the expected performance.

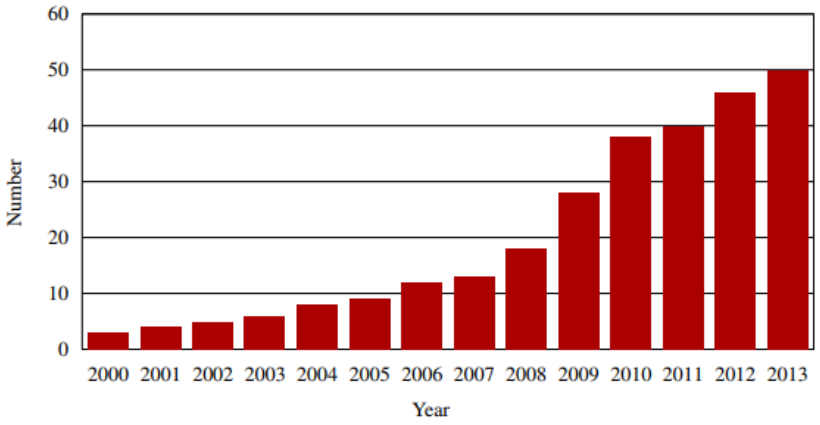

Figure 1.5: Number of airborne wind energy institutions during the first 21st century decade (image from [1]).

1.3.2 Basic AWE concepts

AWES present some important differences with respect to the conventional wind turbines. They use tethers to connect an airborne device to a ground station, which could be mounted on land, at an anchored buoy, at an offshore platform, or on a boat. Here, the lifting device acts as the wind turbine rotor blades, with the evident difference that, while the blades mounted on a conventional turbine are constrained to a rotary motion around its hub, the AWE wings are underpowered.

Moreover, comparing with conventional ones, AWE systems present several advantages. Some of them, covered in [3], are:

- Lower rate of noise pollution and higher effectivity in terms of space usage since they fly at higher altitudes and due to their features;
- Lower material consumption and smaller environmental footprint. Since those systems do not use any tower nor the common installations, thir construction and maintenance efforts lead to a very important cost and mass reduction. At the actual state of the AWES, it is only possible to have a preliminar estimation about the costs of this new energy branch. Different comparisons with the costs get by the conventional technologies, which essentially are related to the amortization of the structures, the electrical equipment, the foundations, authorizations and site use, have revealled that while maintenance costs are almost marginal for both technologies, the main differences has to do with their structures, foundations and required land sites, whose costs are significantly lower for AWE generators;
- High adaptability and larger capacity factor due to the more persistent and stronger wind at high altitudes.

Thanks to all these advantages, AWE has become one of the actual most effective renewable energy resource also for producing electricity in underdeveloped areas or developing countries, where their remote location and the unavailability of technologies are important inconveniences to deploy new energy strategies.

In contrast to the charcteristics above explained, AWES also present some disadvantages. Especially, since these systems are intended to fly at relative low altitudes (in comparison with conventional aircrafts), their interaction with air traffic through different areas, such as special-use airspace, urban environment or even in the open international airspace, should be studied in order to avoid and prevent interferences between AWES and common air traffic. Furthermore, technical problems arise also when taking into account the operation and control of AWE farms, since new methodologies, as well as coordination and maintenance paths, should be designed. In fact, the impossibility of those systems to fly during storms and severe weather conditions suppose to be also an important problem.

Figure 1.6: AWES flight ground visualization. Image from [1].

To develop the AWE control systems, including advanced unmanned vehicle technologies, the search of sophisticated and more durable materials and the requirement for including large energy storage systems, together with the commercialization testings and validations involved and the development of standards of operation and safety, requires an enormous delay in time, resulting another actual important issue of AWES.

All these aspects represent important challenges, but also a lot of future opportunities, multidisciplinary researches and development activities.

1.3.3 AWE power generation

Although different approaches (i.e. type of employed wing) can be used to classify the different AWE technologies branches, the electricity generator position leads to the most important characteristic which allows to further classify those systems. That is because this aspect not only has to do with the design of the whole system, but also with its operating cycle.

Methodologies currently used for power generation by AWE systems follows two different concepts: onboard generators (OBGs) for airborne energy conversion and ground-level generators (GLGs).

Airborne energy conversion

This technology is based on using on-board electric generators mounted directly on the flying device to produce airborne electricity which is sent to the ground through a electrified tether or electric cable. Since those systems must be able of sustaining different systems mounted on, they should present a strong and reliable structure shaped similarly to a glider or small airplane. AWES conceived for airbone energy conversion also include, separately or in combination, rigid wings, gas-filled aerostats or frames with rotating blades.

These systems generate power in a similar way to the one of the tower wind turbines. In contrast, the onboard turbines mounted on these systems do not require to be as large as the ones of the conventional technologies since they are capable of operating at high effective wind speed. Furthermore, apart from other aspects, differently from ground energy conversion AWES, due to the double effect that the aircraft-ground lines realize in this type of systems, they present always the same length, being the aircraft continuously controlled to fly along circular paths.

Figure 1.7: Flying device with wind turbines mounted on. Image by courtesy of Makani.

Ground-based energy conversion. Kite AWE technologies

The ground-based energy conversion systems follows the premise of converting the traction power due to the aerodynamic forces appearing at a lifting device into electricity by a generator on the ground. They ususally works by using tethered wings connected to a control unit at the ground, which is able to fly the system determined flight patterns. Those systems then consist mainly of three parts: a wing itself, a generator on the ground, and the control system joining both.

Solutions with different number of tethers exist. Differently from airborne energy conversion systems, these lines do not transfer electricity, being only on charge of acting as structural and control components. Moreover, looking at Fig. 1.8, where the different parts of a simple ground-based conversion AWES are described, reveals how the tethers are attached to one or more control

units which, at the same time, are linked to the electric generators. The system composed by the the generators and the control system is denoted as Ground Station.

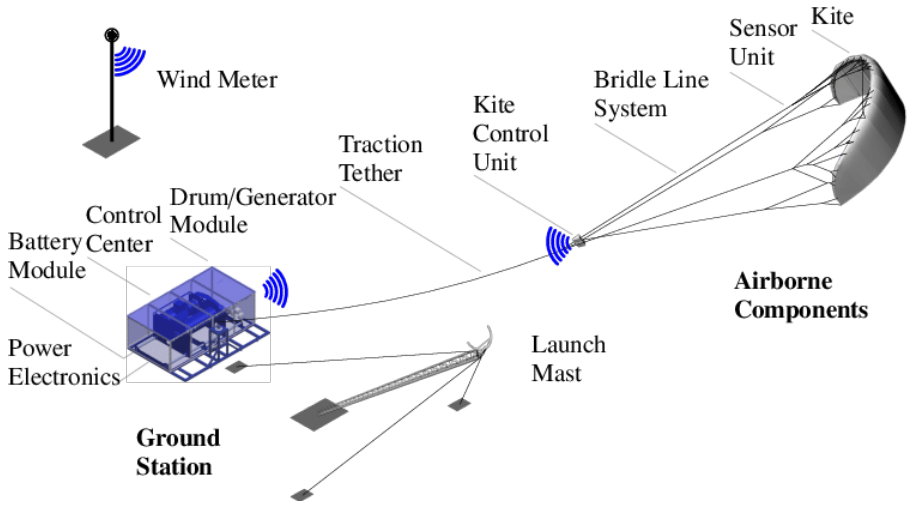

Figure 1.8: Sketch showing a simple ground-based conversion AWES. Image from TU Delft.

In case of the kite AWES, the group of elements conformed by drums, electric drives, onboard sensors, and the hardware needed to control the system, is denoted as Kite Steering Unit. With the aim of extracting as much energy as possible, and depending on how the traction forces are converted into mechanical and electrical power, as described in [9], the KSU can be employed in different ways. Concretely, two different concepts have been further investigated:

1. **Fixed-ground-station systems**. In this configuration, the KSU is fixed with respect to the ground. The energy generation acts in cycles described by means of two phases:

   (a) **Power-generating reel-out phase**. This phase is the one during which the generation of energy takes place. So as to achive that, the aerodynamic forces acting on the lifting device pull off the lines out of the drum, which rotates generating power. Generally in this type of AWES the systems are controlled to fly through figure-eight paths, which, although are slightly less efficient than loops in terms of power generation, they allow to prevent line twisting.

   (b) **Power-consuming reel-in phase**. This phase starts when there is no more cable left on the drum. During this phase, the electric generators acts as motors which, spending some of the energy previously stored, drive the system to a position suitable to start again the traction phase. When the cable is fully retrieved to the minimum length, the cycle is repeated. In fact, during this phase the kites are controlled so that there is minimum tension in the lines. In order to achieve that porpoise, two different ways are considered:

      - *Low power maneuver.* This type of maneuver is based on driving the system to the borbers of the "power zone", where the aerodynamic lift force drops to significant values. This fact allows to recover the kite with evident low energy waste;
      - *Low lift maneuver.* In contrast, this type of maneuver is based on modifying the

angle of attack of the kites by means of onboard actuators, forcing the system to loose its aerodynamic lift force and thus, recovering the lines with special low energy waste. Although the development of that maneuver requires for including onboard actuators to the system, it is more advantageous mesure with respect to the "low power maneuver" in terms of space usage.

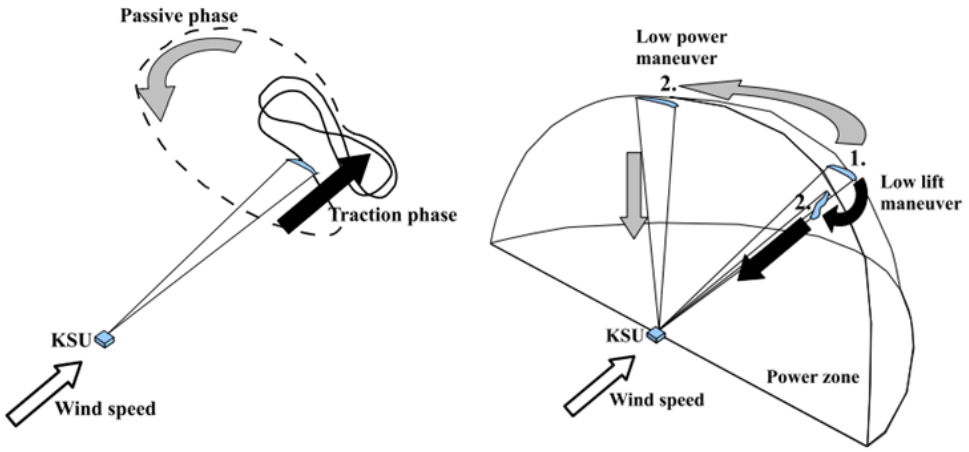

Figure 1.9: Sketch of the operating cycle of an AWE fixed-GS configuration. Left: traction (solid) and passive (dashed) phases. Right: "low power" (gray) and "low lift" (black) maneuvers. Courtesy of [9].

2. **Moving-ground-station systems**. In a moving-GS system, the KSU is located on a vehicle which moves along a determined path. Here, the energy is converted into electricity by means of the vehicle wheels which acts as generators. This concept has been investigated using either lines with variable or constant length.

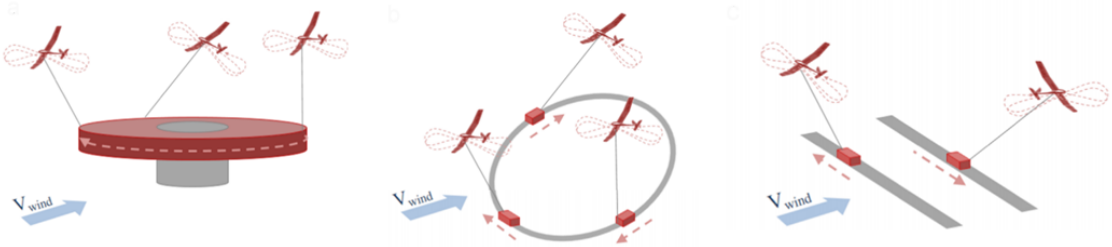

Figure 1.10: Scketch showing three different concepts of moving-GS AWES. Image from [4].

- Constant line length. Systems using lines with constant length generate power by continuously repeating a cycle composed of two phases, namely passive and traction phases, which are now differentiated between them due to the relative position of the KSU with respect to the wind direction.

  During the traction phase, the systms are designed to be pulled by the aerodynamic forces appearing over the lifting device, maximizing the generated power. In the pas-

sive phase, the controller is on charge of placing the kite in a suitable position to begin another traction phase with the minimal energy loss. An example of how this configuration works is shown at Fig. 1.11, where the two phases of the above shown KE-Carousel configuration can be appretiate. Here, due to the circular path, phases are related to the angular position of the control unit with respect to the wind direction.

- Variable line length. This concept comes from the idea of extracting energy also when the vehicle is moving against the wind, being basically centered on mixing both previously seen (fixed-GS and moving-GS with constant lines length) concepts.

  In this case, while the system uses energy for positioning the kites to start a traction phase, the effect of nominal wind pointing in opposite direction to the KSU movement is used to unroll the lines, and then, to generate power in the similar way developed by fixed-GS systems. In parallel, when the KSU starts to move favourable with the nominal wind direction, the traction phase takes place. During this second phase, the kites pulls the vehicle, while the lines are rolled back in order to start the unroll maneuver with the same initial line length. Along each cycle, the net generated power results then from the difference between the energy spent to place the vehicle and to reel-in the lines, and the energy generated by unrolling the lines together with the one generated by the traction kite force.

  As a matter of fact, a variable speed vehicle has been also unerdevelopment with the aim of including an additional degree of freedom to these systems.

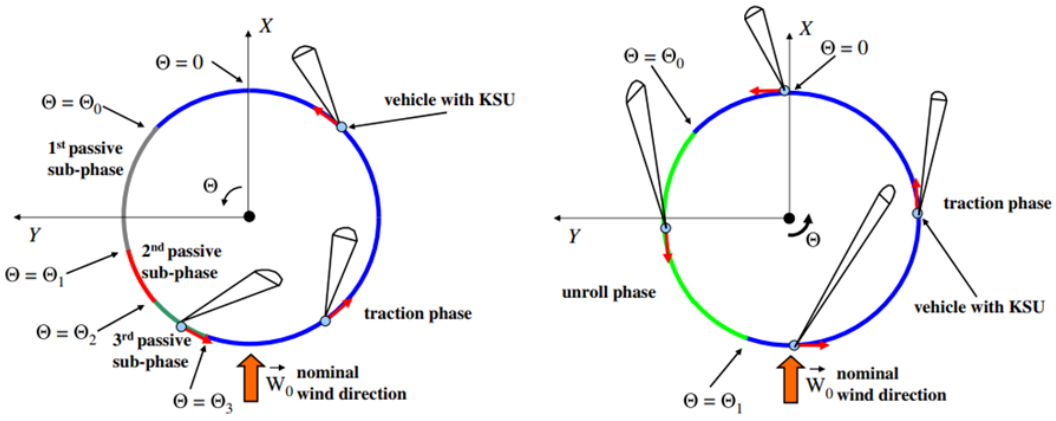

Figure 1.11: General schema showing an example of the working phases of a determined moving-GS system configuration known as KE-Carousel, in which the KSU follows circular paths. Left: fixed line length and; Right: variable line length. Image from [9].

1.3.4 Wings, lines, sensors and actuators

As it was seen, any AWE system is composed by some many important components. Based on the information provided by [8], some of them are described along the following sections.

Wings and lifting devices

AWE concepts use different kinds of flying structures equipped with lifting devices. Usually, those technologies account with glider shaped wings or actually wings like common power kites used for recreational purposes. However, other existing designs are based on rotorcraft-type and aerostatic lifting concepts.

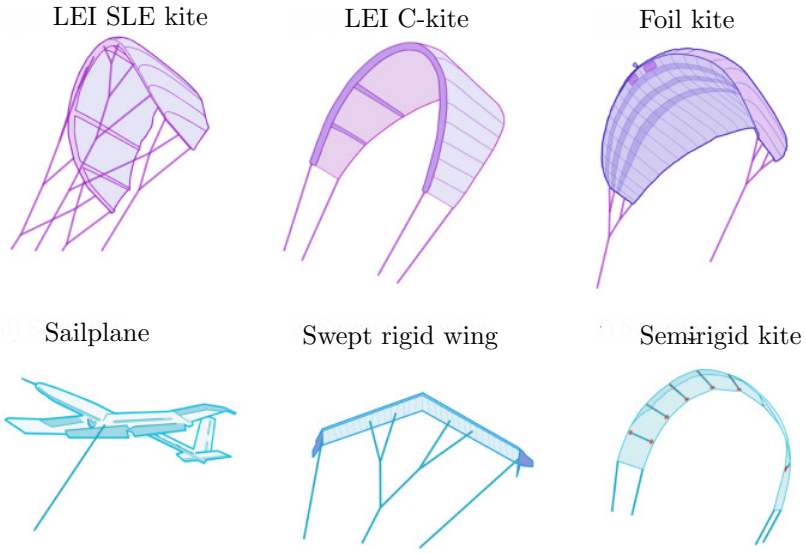

Figure 1.12: Common used lifting-devices for ground conversion AWE technologies. Image obtained from [4].

Essentially, in any case, AWE wings should be controlled to follow determined crosswind flight patterns to produce the aerodynamic force needed for the kinetic energy extraction. In this way, those systems require to present some important structure characteristics like resistance to strain or lightness, both partialy influated by wings design and materials used. Currently the types of employed materials vary from highly flexible membranes to rigid composite materials. Table 1.2 collects the characteristics describing some of the underdeveloped AWE technologies. Here, the fact also shown in figures 1.12 and 1.13, data states that while GLGs use either rigid or flexible wings, OBGs use only rigid devices since they should contain actuators and generators onboard.

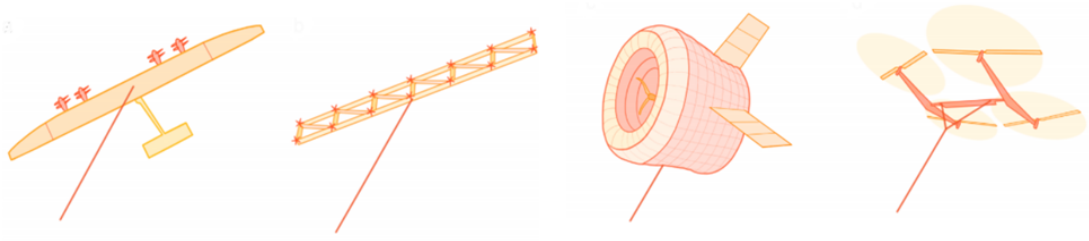

Figure 1.13: Different types of aircrafts used for airborne conversion systems. Courtesy of [4].

Furthermore, being the maneuverability another important aspect for those systems, wings with

Reference	Generator position	Wing	n. of lines
T.U. Delft	GLG	Flexible	1
Politecnico di Torino	GLG	Flexible	2
K.U. Leuven	GLG	Rigid	1
Ampyx Power	GLG	Rigid	1
Joby Energy	OBG	Rigid	1
Kitenergy	GLG	Flexible	2
Makani Power	OBG	Rigid	1
Skysails power	GLG	Flexible	1
Windlift	OBG	Flexible	3

Table 1.2: Features of some AWE technologies. Data from [8].

high aspect ratios are employed as occurs in gliders. At the same time, in terms of efficiency, since depending on the type of employed system, the optimal flight trajectory results to be either a figure-eight or a simple loop, the wingspan should be sized in order to obtain configurations in which, wings can operate close one to the other as much as it would be possible. Thus, searching a high aspect ratio favours the maneuverability of the system, while a low one, do it for the efficiency. In other words, efficiency and maneuverability lead in opposite directions in terms of wing geometry.

Control tethers and lines

As shown in Table 1.2, systems with different number of lines exist. Any way, they are necessary made of strong, durable and light materials. The aerodynamic forces appearing at the lifting device generate a very high tension force on the lines. At the same time, the cables should be as much as light as possible and their diameter contained bellow a certain limit to reduce their weight and aerodynamic drag. All these features should be considered together with the enormous line length required. In shuch a way, to select a material results an issue of paramount difficulty, being commonly constructed of synthetic materials, and also, in case of OBGs, containing inserted conductive materials such as aluminium.

Concretely, the most common material used is a composite nylon or polyethylene fiber, a material which, being lighter than water, presents a traction resistance $8 - 10$ times higher than that of steel lines of the same weight. An example of the minimal breaking load of a cable as a function of its diammeter is presented at Fig. 1.14.

Sensors and actuators

The sensors used in most of the AWE systems are practically expanded to all the tecnologies used. On one hand, sensors on the ground are used to quatify different parameters such as the tension tethers load, wind magnitude and direction as well as line length and speed. On the other

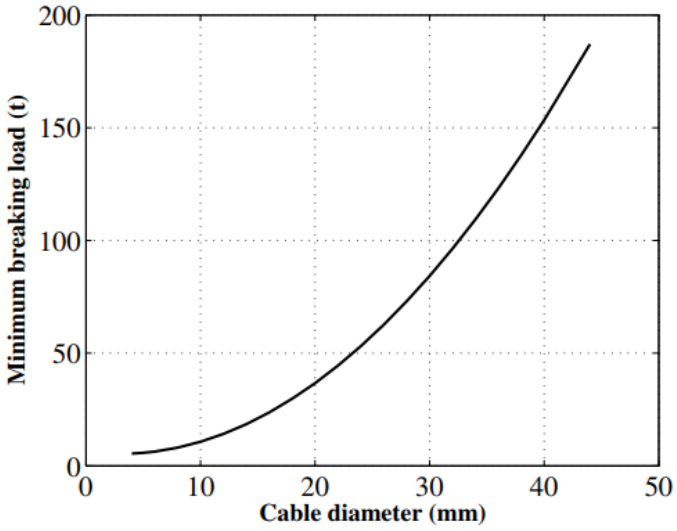

Figure 1.14: Minimum breaking load of a line as a function of its diameter. Courtesy of [8].

hand, flight relevant data such as aircraft position, speed and attitude, is typically obtained by an onboard IMU, including a GPS, a magnetometer, gyroscopes and accelerometers.

Regarding the types of actuators, they are directly related to the type of AWE generator and lifting device used. In first place, AWES with OBGs and GLGs with rigid wings use onboard actuators including conventional aircraft control surfaces (ailerons, elevators, and rudder) and onboard turbines acting as propellers. In contrast, GLGs with flexible wings may present either onboard and/or ground actuators. While the first ones, typically packed in a control unit hung placed bellow the wing, are used in single-line technologies allowing to simplify the GS design and to develop more immediate control actions; in GLG solutions accounting with more than one line, ground actuators are only implemented, yielding a reduction on aircraft weight, an increment in aerodynamic efficiency and higher safety reasons.

1.3.5 Controllability of the AWE generators

AWES make use of its capability of flying determined crosswind flight patterns at high speed in the different possible scenarios to extract as much energy as possible, and obviously, then its power output is directly related to the aerodynamic properties of the used wings. To satisfy this, the flight of the whole system should be driven by an automatic control unit which keeps it flying perpendicular to the direction of the wind. Therefore, a reliable control system is required to fly the wing by following the optimal paths.

As covered in [9], automatic control is then a paramount important aspect of any AWES. The dynamics of those systems is generally nonlinear and tipically unstable in open-loop. Hence, the control unit, while trying to be able to maximize the power generated, it also should be able to counteract the external weather or additional perturbations which could be unstabilize the system. In cases with more than one line, the control system must also avoid line wrapping.

1.4 Thesis objectives and methodology

To analyze the performance of any AWES, many different approaches using analytical techniques have been modeled in the past for the construction of flight simulators. Essentially, there are two objectives in this thesis. To construct a dynamical model of a kite-based AWES named **Train of kites**, and the evaluation of the stability of the uncontrolled motion of this system.

In first place, for the modeling of the AWES, selection of the important features of the system, i.e. components, inertial characteristics, lines attachment points, or some other geometrical reasons are evaluated, including the definition of the degrees of freedom and frames of reference used. Once the model is constructed, the kinematic analysis is performed, with the principal aim to obtain analytical expressions of the position vector and linear, and angular velocities for each individual kite. The introduction of a correct aerodynamic model, and the obtainment of expressions for the kinetic and potential energies, allow to write the Lagrangian equations of motion of the system.

Secondly, the analysis of the system dynamics around its equilibrium position for unmanned control is performed. The introduction of the dimensional parameters into the model, allows to find a stable equilibrium position of the system. Some assumptions implemented to the defined dynamical problem, give place to a simple linear system of equations, which once solved, the normal modes of the system are found. Integration of the complete system of equations of motion allows to get a complete evaluation of the system normal modes. This allow to get first a complete understanding about the normal modes of a simple kite, and then, the final objective based on learning about the dynamics of the whole system.

Chapter 2

Kite train model

2.1 Hypotheses and notation

This section presents the notation used for the modeling of a train of N_k two-line kites. For convenience, an extensive use of dimensionless variables and some shortenings are made to improve the legibility of this work. In particular, the derivative of any variable with respect to the dimensionless time $\tau = t\sqrt{g/L_1}$, will be denoted with a dot. Here, g will be the gravitational acceleration and, L_1 the length of the first kite tethers. For brevity, the sine and cosine of an angle α will be written as $s\alpha$ and $c\alpha$. Most of the lower case and capital letters denote variables without and with dimensions respectively. The unitary vectors for any frame of reference will be denoted as $\boldsymbol{i}_n^k$, $\boldsymbol{j}_n^k$ and $\boldsymbol{k}_n^k$, being the superscript k referred to the kite involved, and n, referred to the system S_n^k in current use. Bold letters are used to denote vectors and tensors.

The rotation matrices relating the vector components in different basis will be written as $\bar{\boldsymbol{R}}_{ij}$. For instance, calling vector $\boldsymbol{a} = x_1\boldsymbol{i}_1 + y_1\boldsymbol{j}_1 + z_1\boldsymbol{k}_1 = x_2\boldsymbol{i}_2 + y_2\boldsymbol{j}_2 + z_2\boldsymbol{k}_2$,

$$\begin{pmatrix} x_2 \\ y_2 \\ z_2 \end{pmatrix} = \bar{\boldsymbol{R}}_{21} \cdot \begin{pmatrix} x_1 \\ y_1 \\ z_1 \end{pmatrix} \tag{2.1}$$

where $\bar{\boldsymbol{R}}_{21}$ is the rotation matrix that relates the components in the frames S_1 and S_2. All the rotation matrices appearing satisfy $\det\left(\bar{\boldsymbol{R}}_{ij}\right) = 1$ and $\bar{\boldsymbol{R}}_{ij} \cdot \bar{\boldsymbol{R}}_{ji} = \bar{\boldsymbol{I}}$ where $\bar{\boldsymbol{R}}_{ji} = \bar{\boldsymbol{R}}_{ij}^T = \bar{\boldsymbol{R}}_{ij}^{-1}$ for whatever the possible values of i and j.

The wind velocity will be considered of constant magnitude and direction. This property is used to introduce an inertial frame of reference, named the Earth frame S_E with origin at point O_E and, whose O_Ex_E axis is opposed to the wind velocity vector. The plane spanned by O_Ex_E and O_Ey_E axes coincides with the flat ground, while the O_Ez_E axis points downwards to the Earth center.

The model considers N_k rigid symmetric kites, each with mass m_k, surface S_k, chord c_k, and wingspan b_k. The kites are positioned in the configuration shown at Fig. 2.1, locating each one over the previous in ascend order. For convenience, we enumerate them from 1 to N_k starting from the lowest one. Being $k \in \{1, 2, \cdots N_k\}$, the $\{k\}$-kite is linked to two rigid massless tethers of constant length L_k at points $A_k^{\pm}$, which connect it with the $\{k-1\}$-kite. The position of these points is given as

$$\overrightarrow{G_kA_k^{\pm}} = L_1\left(x_A^k\boldsymbol{i}_B^k \pm y_A^k\boldsymbol{j}_B^k + z_A^k\boldsymbol{k}_B^k\right) \tag{2.2}$$

The $\{k\}$-kite is linked to the $\{k+1\}$-kite through the points $C_k^{\pm}$ where the tethers with length L_{k+1} are attached. The position of those points reads

$$\overrightarrow{G_kC_k^{\pm}} = L_1\left(x_C^k\boldsymbol{i}_B^k \pm y_C^k\boldsymbol{j}_B^k + z_C^k\boldsymbol{k}_B^k\right) \tag{2.3}$$

A reference frame, named the body frame S_B^k, linked to the $\{k\}$-kite and attached to its center of mass G_k, is introduced. The S_B^k axes coincide with the kite principal axes of inertia about point G_k. Therefore, the moment of inertia tensor of each kite about its center of gravity in its body

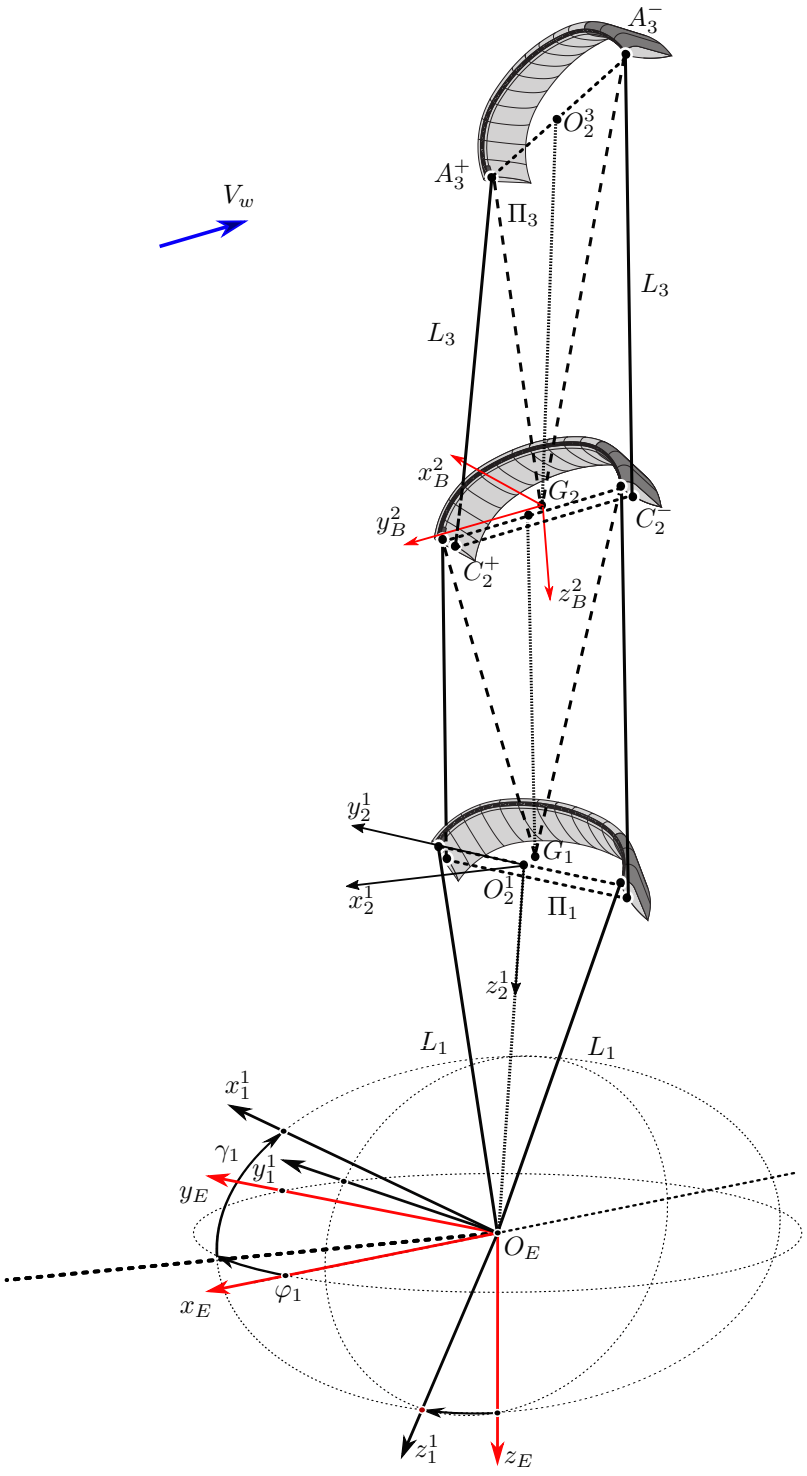

Figure 2.1: Sketch showing the position of the model of a reduced system of three two-line kites with respect to the S_E reference frame, the frames S_E, S_1^1, S_2^1 and S_B^2 and the definition of the state angles γ_1 and φ_1.

frame is a diagonal matrix, $\bar{\boldsymbol{I}}_G^k = m_1 L_1^2 \bar{\boldsymbol{\iota}}_G^k$, with $\bar{\boldsymbol{\iota}}_G^k$ the diamensionless matrix,

$$\bar{\boldsymbol{\iota}}_G^k = \begin{pmatrix} \iota_x^k & 0 & 0 \\ 0 & \iota_y^k & 0 \\ 0 & 0 & \iota_z^k \end{pmatrix} \tag{2.4}$$

2.2 DoFs and frames of references

Neglecting the flexibility effects lets to consider each kite as a rigid body. In general, a mechanical system made of N_k rigid bodies has $6N_k$ degrees of freedom. However, since each kite is attached to two inelastic tethers which constrain its motion, the train of kites involves $2N_k$ geometrical constraints, thus meaning, the system presents $6N_k - 2N_k = 4N_k$ degrees of freedom.

The state vector of each kite will be composed by four angles. That means that, those ones are able to define not only the orientation of the kite, but also the position of the kite with respect to the inertial reference frame, S_E, by means of four rotations.

A key geometrical element is the plane Π_k. This plane is defined for each kite by means of the points A_k^+, A_k^- and G_{k-1} (or point O_E for the first kite). For convenience, an auxiliary frame named S_1^k with origin at O_E and axes $O_1^k y_1^k$ and $O_1^k z_1^k$ spanning the Π_k plane is introduced. The precise orientation of that frame with respect to S_E is given by two consecutive rotations. The first one is a rotation of value $\varphi_k(\tau)$ about $\boldsymbol{k}_E^k$, and the second is a rotation of value $\gamma_k(\tau)$ about $\boldsymbol{j}_1^k$. Therefore the rotation matrix that transforms vector components from S_E^k to S_1^k is

$$\bar{\boldsymbol{R}}_{1E}^k = \begin{pmatrix} c\varphi_k c\gamma_k & s\varphi_k c\gamma_k & -s\gamma_k \\ -s\varphi_k & c\varphi_k & 0 \\ c\varphi_k s\gamma_k & s\varphi_k s\gamma_k & c\gamma_k \end{pmatrix} \tag{2.5}$$

and the angular velocity of S_1^k with respect to S_E^k, $\boldsymbol{\Omega}_{1E}^k = \sqrt{g/L_1}\,\boldsymbol{\omega}_{1E}^k = \sqrt{g/L_1}\left(\dot{\varphi}_k \boldsymbol{k}_E + \dot{\gamma}_k \boldsymbol{j}_1^k\right)$.

Being known the position of the points A_k^+, A_k^- and G_{k-1} (or point O_E in the case of the first kite) defining a triangle whose one its vertex is coincident with the point O_1^k, just one coordinate is required to locate this triangle within the plane Π_k. A reference frame S_2^k with origin O_2^k at the midpoint of the segment $\overline{A_k^+ A_k^-}$ and linked to this triangle is introduced. Its axis $O_2^k y_2^k$ points from A_k^- to A_k^+, while $O_2^k z_2^k$ and $O_2^k x_2^k$ are, contained in, and normal to the plane Π_k respectively. The relative position of S_2^k with respect to S_1^k is given by the angle $\eta_k(\tau)$ between $O_1^k y_1^k$ and $O_2^k y_2^k$. The rotation matrix that transforms vector components from S_1^k to S_2^k, is

$$\bar{\boldsymbol{R}}_{21}^k = \begin{pmatrix} 1 & 0 & 0 \\ 0 & c\eta_k & s\eta_k \\ 0 & -s\eta_k & c\eta_k \end{pmatrix} \tag{2.6}$$

and the angular velocity of S_2^k with respect to S_1^k reads $\boldsymbol{\Omega}_{21}^k = \sqrt{g/L_1}\,\boldsymbol{\omega}_{21}^k = \sqrt{g/L_1}\,\dot{\eta}_k \boldsymbol{i}_2^k$.

The location of the kite with respect to S_2^k just requires a last additional coordinate. Since points A_k^- and A_k^+ are symmetric with respect to the symmetry plane of the kite, axes $O_2^k y_2^k$ and $O_B^k y_B^k$

are parallel, thus being the orientation of S_B^k with respect to S_2^k fully determined by the angle $\theta_k(\tau)$ between $O_B^k x_B^k$ and $O_2^k x_2^k$. The rotation matrix reads

$$\bar{\boldsymbol{R}}_{B2}^k = \begin{pmatrix} c\theta_k & 0 & -s\theta_k \\ 0 & 1 & 0 \\ s\theta_k & 0 & c\theta_k \end{pmatrix} \tag{2.7}$$

while the angular velocity is $\boldsymbol{\Omega}_{B2}^k = \sqrt{g/L_1}\,\boldsymbol{\omega}_{B2}^k = \sqrt{g/L_1}\,\dot{\theta}_k \boldsymbol{j}_B^k$.

(a)

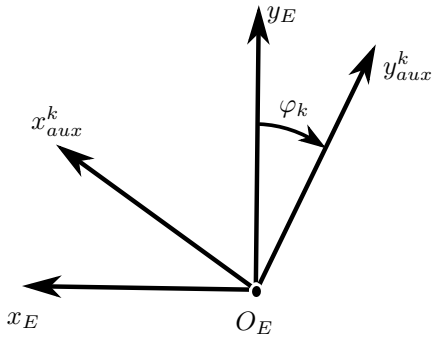

Table 2.1: Sketch showing the definition of the angle φ_k.

(b)

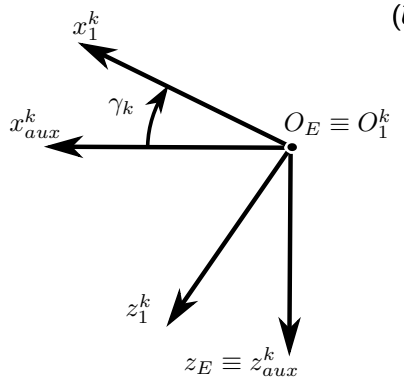

Table 2.2: Sketch showing the definition of the angle γ_k.

(c)

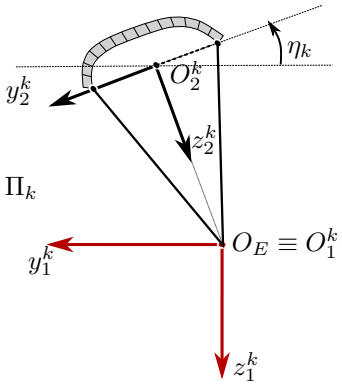

Table 2.3: Sketch showing the plane Π_k including the definition of the angle η_k.

(d)

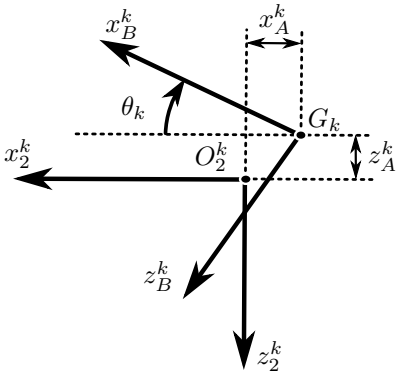

Table 2.4: Sketch showing the definition of the angle θ_k.

Let $\boldsymbol{x}_s^k = [\varphi_k \;\; \gamma_k \;\; \eta_k \;\; \theta_k]^T$ be then the state vector of the $\{k\}$-kite, while the state vector of the entire system reads

$$\boldsymbol{x}_s = [\boldsymbol{x}_s^1 \;\; \boldsymbol{x}_s^2 \cdots \boldsymbol{x}_s^{N_k}]^T \tag{2.8}$$

Hereafter, it is useful to define the matrices $\bar{\boldsymbol{R}}_{BE}^k = \bar{\boldsymbol{R}}_{B2}^k \cdot \bar{\boldsymbol{R}}_{21}^k \cdot \bar{\boldsymbol{R}}_{1E}^k$, $\bar{\boldsymbol{R}}_{B1}^k = \bar{\boldsymbol{R}}_{B2}^k \cdot \bar{\boldsymbol{R}}_{21}^k$ and $\bar{\boldsymbol{R}}_{2E}^k = \bar{\boldsymbol{R}}_{21}^k \cdot \bar{\boldsymbol{R}}_{1E}^k$.

2.3 Kinematic calculations

This section searches to find the kinematic relationships which will allow to deploy then the system Lagrangian equations of motion. The Lagrangian mechanics takes advantage of the potential and kinetic energies. In this way, an expression for the angular and linear velocities as well as the vector position should be developed.

2.3.1 Angular velocity

Remembering from previous advances, the absolute angular velocity of a kite is

$$\boldsymbol{\Omega}_{BE}^{k} = \boldsymbol{\Omega}_{B2}^{k} + \boldsymbol{\Omega}_{21}^{k} + \boldsymbol{\Omega}_{1E}^{k} = \sqrt{g/L_1}\left(\dot{\varphi}_k \boldsymbol{k}_E + \dot{\gamma}_k \boldsymbol{j}_1^k + \dot{\eta}_k \boldsymbol{i}_2^k + \dot{\theta}_k \boldsymbol{j}_B^k\right) \tag{2.9}$$

which would be interesting to be projected in the body frame axes. Due to this, making use of the rotational matrices previously developed, one can write

$$\boldsymbol{\Omega}_{BE}^{k}\Big|_{S_B^k} = \sqrt{g/L_1}\ \boldsymbol{\omega}_{BE}^{k}\big|_{S_B^k} = \sqrt{g/L_1}\left(\dot{\varphi}_k \bar{\boldsymbol{R}}_{BE}^{k} \cdot \boldsymbol{k}_E + \dot{\gamma}_k \bar{\boldsymbol{R}}_{B1}^{k} \cdot \boldsymbol{j}_1^k + \dot{\eta}_k \bar{\boldsymbol{R}}_{B2}^{k} \cdot \boldsymbol{i}_2^k + \dot{\theta}_k \boldsymbol{j}_B^k\right) \tag{2.10}$$

where explicitly, the S_B-components, $\boldsymbol{\omega}_{BE}^{k}\big|_{S_B^k} = \omega_x^k \boldsymbol{i}_B^k + \omega_y^k \boldsymbol{j}_B^k + \omega_z^k \boldsymbol{k}_B^k$ are given by

$$\begin{pmatrix} \omega_x^k \\ \omega_y^k \\ \omega_z^k \end{pmatrix} = \bar{\boldsymbol{\Phi}}_k\left(\varphi_k, \gamma_k, \eta_k, \theta_k\right) \cdot \dot{\boldsymbol{x}}_s^k \tag{2.11}$$

being

$$\bar{\boldsymbol{\Phi}}_k = \begin{pmatrix} -c\gamma_k c\eta_k s\theta_k - s\gamma_k c\theta_k & s\eta_k s\theta_k & c\theta_k & 0 \\ c\gamma_k s\eta_k & c\eta_k & 0 & 1 \\ c\gamma_k c\eta_k c\theta_k - s\gamma_k s\theta_k & -s\eta_k c\theta_k & s\theta_k & 0 \end{pmatrix} \tag{2.12}$$

2.3.2 Position vector

The position vector of the center of mass of the $\{k\}$-kite is given as

$$\boldsymbol{r}_k = \boldsymbol{r}_1 + \sum_{n=2}^{k} \frac{\overrightarrow{G_{n-1}G_n}}{L_1} = \frac{1}{L_1}\left[\overrightarrow{O_E O_2^1} + \overrightarrow{O_2^1 G_1} + \sum_{n=2}^{k} \overrightarrow{G_{n-1}O_2^n} + \overrightarrow{O_2^n G_n}\right] =$$

$$= \sum_{n=1}^{k} \left(\zeta_n \boldsymbol{j}_2^n + \xi_n \boldsymbol{k}_2^n\right) - \left(x_A^n \boldsymbol{i}_B^n + z_A^k \boldsymbol{k}_B^n\right) \tag{2.13}$$

In Eq. 2.13, the fact that the vector $\overrightarrow{G_{k-1}O_2^k}$ (or $\overrightarrow{O_E O_2^1}$ in case of the first kite) belongs to the Π_k plane, spanned by the axes $O_2^k y_2^k$ and $O_2^k z_2^k$, is used. Because of that, the vector is written as

$\overrightarrow{G_{k-1}O_2^k} = L_1\left(\zeta_k \boldsymbol{j}_2^k + \xi_k \boldsymbol{k}_2^k\right)$. Using the rotation matrices, then one finds

$$\begin{aligned}\boldsymbol{r}_k = -\sum_{n=1}^{k} &\left[\left(x_A^n c\theta_n + z_A^n s\theta_n\right) c\gamma_n c\varphi_n + \left(\xi_n - x_A^n s\theta_n + z_A^n c\theta_n\right)\left(c\eta_n s\gamma_n c\varphi_n + s\eta_n s\varphi_n\right)\right.\\ &\left.+\zeta_n\left(s\eta_n s\gamma_n c\varphi_n - c\eta_n s\varphi_n\right)\right]\boldsymbol{x}_E\\ &+\left[\left(x_A^n c\theta_n + z_A^n s\theta_n\right) c\gamma_n s\varphi_n + \left(\xi_n - x_A^n s\theta_n + z_A^n c\theta_n\right)\left(c\eta_n s\gamma_n s\varphi_n - s\eta_n c\varphi_n\right)\right.\\ &\left.+\zeta_n\left(s\eta_n s\gamma_n s\varphi_n + c\eta_n c\varphi_n\right)\right]\boldsymbol{y}_E\\ &-\left[\left(x_A^n c\theta_n + z_A^n s\theta_n\right) s\gamma_n - \left(\xi_n - x_A^n s\theta_n + z_A^n c\theta_n\right) c\eta_n c\gamma_n - \zeta_n s\eta_n c\gamma_n\right]\boldsymbol{z}_E\end{aligned} \tag{2.14}$$

Computation of ζ_k and ξ_k

Variables ζ_k and ξ_k are determined by solving the constraints imposed by the inextensible tethers. Being ℓ_k the non dimensional length of the $\{k\}$-tethers, these constraints are

$$\ell_k = \frac{|\,\overline{C_{k-1}^{\pm}A_k^{\pm}}\,|}{L_1} = \frac{|\,\overline{C_{k-1}^{\pm}G_{k-1}} + \overline{G_{k-1}O_2^k} + \overline{O_2^k A_k^{\pm}}\,|}{L_1} \tag{2.15}$$

For convenience, one can write, $\overline{C_{k-1}^{\pm}G_{k-1}} + \overline{O_2^k A_k^{\pm}} = L_1\left(c_{x_k}^{\pm}\boldsymbol{i}_2^k + c_{y_k}^{\pm}\boldsymbol{j}_2^k + c_{z_k}^{\pm}\boldsymbol{k}_2^k\right)$ with

$$\begin{pmatrix} c_{x_k}^{\pm} \\ c_{y_k}^{\pm} \\ c_{z_k}^{\pm} \end{pmatrix} = -\bar{\boldsymbol{R}}_{2E}^k \cdot \bar{\boldsymbol{R}}_{EB}^{k-1} \cdot \begin{pmatrix} +x_C^{k-1} \\ \pm y_C^{k-1} \\ +z_C^{k-1} \end{pmatrix} \pm \begin{pmatrix} 0 \\ y_A^k \\ 0 \end{pmatrix}, \tag{2.16}$$

and with $x_C^0 = y_C^0 = z_C^0 = 0$. The two constraints in Eq. 2.15 then become two circumferences defined as

$$\ell_k^2 - {c_{x_k}^{\pm}}^2 \equiv {\kappa_k^{\pm}}^2 = \left(\zeta_k - c_{y_k}^{\pm}\right)^2 + \left(\xi_k - c_{z_k}^{\pm}\right)^2 \tag{2.17}$$

The intersection of these two circumferences contained in the same plane (see Fig. 2.2), reads

$$\begin{aligned}(\zeta_k, \xi_k) =& \frac{1}{2}\left(c_{y_k}^{+} + c_{y_k}^{-}, c_{z_k}^{+} + c_{z_k}^{-}\right) + \frac{{\kappa_k^{+}}^2 - {\kappa_k^{-}}^2}{2R^2}\left(c_{y_k}^{-} - c_{y_k}^{+}, c_{z_k}^{-} - c_{z_k}^{+}\right) +\\ &+ \frac{1}{2R^2}\sqrt{\left[\left(\kappa_k^{+} + \kappa_k^{-}\right)^2 - R^2\right]\left[R^2 - \left(\kappa_k^{+} - \kappa_k^{-}\right)^2\right]}\left(c_{z_k}^{-} - c_{z_k}^{+}, c_{y_k}^{+} - c_{y_k}^{-}\right)\end{aligned} \tag{2.18}$$

where

$$R = \sqrt{\left(c_{y_k}^{+} - c_{y_k}^{-}\right)^2 + \left(c_{z_k}^{+} - c_{z_k}^{-}\right)^2} \tag{2.19}$$

For $k = 1$, one simply has $\xi_1 = \sqrt{1 - {y_A^1}^2}$ and $\zeta_1 = 0$.

2.3.3 Linear velocity

Taking the τ-derivative of Eq. 2.14, one finds that the S_E-components of the $\{k\}$-kite normalized velocity, $\boldsymbol{v}_k = v_x^k \boldsymbol{i}_E + v_y^k \boldsymbol{j}_E + v_z^k \boldsymbol{k}_E$, can be written as

$$\begin{pmatrix} v_x^k \\ v_y^k \\ v_z^k \end{pmatrix} = -\sum_{n=1}^{k} \bar{\boldsymbol{\Upsilon}}_n^C\left(\dot{\boldsymbol{x}}_s^n, \zeta_n, \xi_n, x_A^n, z_A^n\right) \cdot \dot{\boldsymbol{x}}_s^n + \bar{\boldsymbol{\Upsilon}}_n^D\left(\dot{\boldsymbol{x}}_s, \xi_n, \zeta_n\right) \cdot \dot{\boldsymbol{x}}_s \equiv \boldsymbol{\Upsilon}_k \cdot \dot{\boldsymbol{x}}_s \tag{2.20}$$

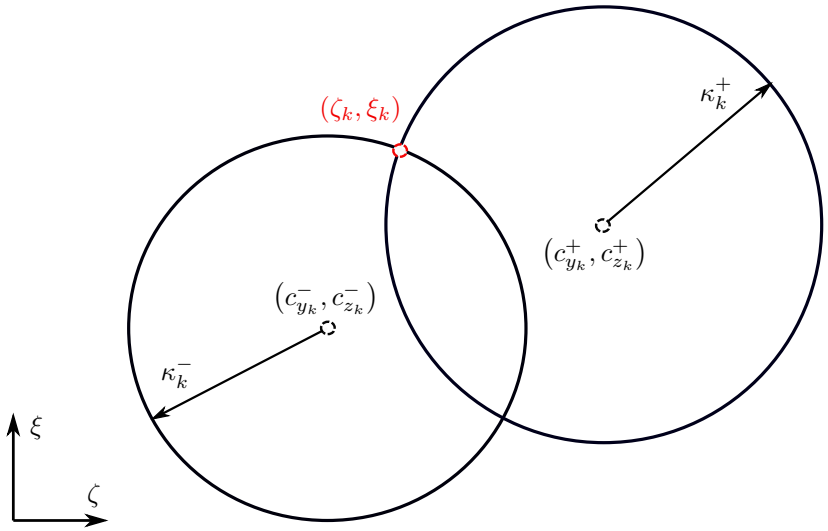

Figure 2.2: Sketch in the $\zeta\xi$ plane showing the intersection of the two circunferences determining the values of ζ_k and ξ_k.

where the components of tensor $\bar{\boldsymbol{\Upsilon}}_n^C$ are given by

$$\begin{aligned}
\Upsilon_n^C(1,1) =&(x_A^n c\theta_n + z_A^n s\theta_n)c\gamma_n s\varphi_n + (\xi_n - x_A^n s\theta_n + z_A^n c\theta_n)(c\eta_n s\gamma_n s\varphi_n - s\eta_n c\varphi_n)+\\
&+ \zeta_n\left(c\eta_n c\varphi_n + s\eta_n s\gamma_n\right) && (2.21)\\
\Upsilon_n^C(1,2) =&(x_A^n c\theta_n + z_A^n s\theta_n)s\gamma_n c\varphi_n - (\xi_n - x_A^n s\theta_n + z_A^n c\theta_n)c\eta_n c\gamma_n c\varphi_n - \zeta_n s\eta_n c\gamma_n c\varphi_n && (2.22)\\
\Upsilon_n^C(1,3) =&(\xi_n - x_A^n s\theta_n + z_A^n c\theta_n)(s\eta_n s\gamma_n c\varphi_n - c\eta_n s\varphi_n) - \zeta_n\left(s\eta_n s\varphi_n + c\eta_n s\gamma_n c\varphi_n\right) && (2.23)\\
\Upsilon_n^C(1,4) =&(x_A^n s\theta_n - z_A^n c\theta_n)c\gamma_n c\varphi_n + (x_A^n c\theta_n + z_A^n s\theta_n)(c\eta_n s\gamma_n c\varphi_n + s\eta_n s\varphi_n) && (2.24)\\
\Upsilon_n^C(2,1) =&-(x_A^n c\theta_n + z_A^n s\theta_n)c\gamma_n c\varphi_n - (\xi_n - x_A^n s\theta_n + z_A^n c\theta_n)(c\eta_n s\gamma_n c\varphi_n + s\eta_n s\varphi_n)+\\
&+ \zeta_n\left(c\eta_n s\varphi_n - s\eta_n s\gamma_n c\varphi_n\right) && (2.25)\\
\Upsilon_n^C(2,2) =&(x_A^n c\theta_n + z_A^n s\theta_n)s\gamma_n s\varphi_n - (\xi_n - x_A^n s\theta_n + z_A^n c\theta_n)c\eta_n c\gamma_n s\varphi_n - \zeta_n s\eta_n c\gamma_n s\varphi_n && (2.26)\\
\Upsilon_n^C(2,3) =&(\xi_n - x_A^n s\theta_n + z_A^n c\theta_n)(s\eta_n s\gamma_n s\varphi_n + c\eta_n c\varphi_n) + \zeta_n\left(s\eta_n c\varphi_n - c\eta_n s\gamma_n s\varphi_n\right) && (2.27)\\
\Upsilon_n^C(2,4) =&(x_A^n s\theta_n - z_A^n c\theta_n)c\gamma_n s\varphi_n + (x_A^n c\theta_n + z_A^n s\theta_n)(c\eta_n s\gamma_n s\varphi_n - s\eta_n c\varphi_n) && (2.28)\\
\Upsilon_n^C(3,1) =&0 && (2.29)\\
\Upsilon_n^C(3,2) =&(x_A^n c\theta_n + z_A^n s\theta_n)c\gamma_n + (\xi_n - x_A^n s\theta_n + z_A^n c\theta_n)c\eta_n s\gamma_n + \zeta_n s\eta_n s\gamma_n && (2.30)\\
\Upsilon_n^C(3,3) =&(\xi_n - x_A^n s\theta_n + z_A^n c\theta_n)s\eta_n c\gamma_n - \zeta_n c\eta_n c\gamma_n && (2.31)\\
\Upsilon_n^C(3,4) =&-(x_A^n s\theta_n - z_A^n c\theta_n)s\gamma_n + (x_A^n c\theta_n + z_A^n s\theta_n)c\eta_n c\gamma_n && (2.32)
\end{aligned}$$

and

$$\bar{\boldsymbol{\Upsilon}}_n^D = -\begin{pmatrix} c\eta_n s\gamma_n c\varphi_n + s\eta_n s\varphi_n \\ c\eta_n s\gamma_n s\varphi_n - s\eta_n c\varphi_n \\ c\eta_n c\gamma_n \end{pmatrix}\nabla_{\boldsymbol{x}_s}\xi_n - \begin{pmatrix} s\eta_n s\gamma_n c\varphi_n - c\eta_n s\varphi_n \\ s\eta_n s\gamma_n s\varphi_n + c\eta_n c\varphi_n \\ s\eta_n c\gamma_n \end{pmatrix}\nabla_{\boldsymbol{x}_s}\zeta_n \tag{2.33}$$

The terms $\nabla_{\boldsymbol{x}_s}\xi_n$ and $\nabla_{\boldsymbol{x}_s}\zeta_n$ in Eq. 2.33 are found by taking the gradient operator

$$\nabla_{\boldsymbol{x}_s} = \begin{bmatrix} \dfrac{\partial}{\partial\varphi_1} & \dfrac{\partial}{\partial\gamma_1} & \dfrac{\partial}{\partial\eta_1} & \dfrac{\partial}{\partial\theta_1} \cdots \dfrac{\partial}{\partial\varphi_{N_k}} & \dfrac{\partial}{\partial\gamma_{N_k}} & \dfrac{\partial}{\partial\eta_{N_k}} & \dfrac{\partial}{\partial\theta_{N_k}} \end{bmatrix} \tag{2.34}$$

to Eq. 2.18. Such operation involves the gradients of $c^{\pm}_{x_n}$, $c^{\pm}_{y_n}$, and $c^{\pm}_{z_n}$, which are computed easily by noting that the only terms depending on the state vector in Eq. 2.16 are included in the matrix

$$\bar{\boldsymbol{R}}^{n}_{2E} \cdot \bar{\boldsymbol{R}}^{n-1}_{EB} = \bar{\boldsymbol{R}}^{n}_{21}\left(\eta_n\right) \cdot \bar{\boldsymbol{R}}^{n}_{1E}\left(\varphi_n, \gamma_n\right) \cdot \bar{\boldsymbol{R}}^{n-1}_{E1}\left(\varphi_{n-1}, \gamma_{n-1}\right) \cdot \bar{\boldsymbol{R}}^{n-1}_{12}\left(\eta_{n-1}\right) \cdot \bar{\boldsymbol{R}}^{n-1}_{2B}\left(\theta_{n-1}\right) \tag{2.35}$$

Therefore, the only non-zero elements of the gradients of $c^{\pm}_{x_n}$, $c^{\pm}_{y_n}$, and $c^{\pm}_{z_n}$ are the ones involving the derivatives with respect to φ_n, γ_n, η_n, φ_{n-1}, γ_{n-1}, η_{n-1}, and θ_{n-1}. Two examples are

$$\frac{\partial}{\partial \eta_n}\begin{pmatrix} c^{\pm}_{x_n} \\ c^{\pm}_{y_n} \\ c^{\pm}_{z_n} \end{pmatrix} = -\frac{\partial \bar{\boldsymbol{R}}^{n}_{21}}{\partial \eta_n} \cdot \bar{\boldsymbol{R}}^{n}_{1E} \cdot \bar{\boldsymbol{R}}^{n-1}_{E1} \cdot \bar{\boldsymbol{R}}^{n-1}_{12} \cdot \bar{\boldsymbol{R}}^{n-1}_{2B} \begin{pmatrix} +x^{n-1}_{C} \\ \pm y^{n-1}_{C} \\ +z^{n-1}_{C} \end{pmatrix} \tag{2.36}$$

$$\frac{\partial}{\partial \varphi_{n-1}}\begin{pmatrix} c^{\pm}_{x_n} \\ c^{\pm}_{y_n} \\ c^{\pm}_{z_n} \end{pmatrix} = -\bar{\boldsymbol{R}}^{n}_{21} \cdot \bar{\boldsymbol{R}}^{n}_{1E} \cdot \frac{\partial \bar{\boldsymbol{R}}^{n-1}_{E1}}{\partial \varphi_{n-1}} \cdot \bar{\boldsymbol{R}}^{n-1}_{12} \cdot \bar{\boldsymbol{R}}^{n-1}_{2B} \begin{pmatrix} +x^{n-1}_{C} \\ \pm y^{n-1}_{C} \\ +z^{n-1}_{C} \end{pmatrix} \tag{2.37}$$

2.4 Equations of motion

In order to find the equations of motion of the system, the Langrangian formulation is used. Since the constrain forces appearing in the system (i.e. tension line forces) are holonomic, Langrangian mechanics allows to write a very compact form for the equations of motion of each kite without containing explicity these forces into the equations. Along the following sections, the procedures followed to develop the system equation of motion are covered.

2.4.1 Lagrangian function and generalized forces

Calling x_{s_i} to the i-component of the system state vector in Eq. 2.8, Lagrange's equations read

$$\frac{\mathrm{d}}{\mathrm{d}\tau}\left(\frac{\partial \mathcal{L}}{\partial \dot{x}_{s_i}}\right) - \frac{\partial \mathcal{L}}{\partial x_{s_i}} = Q_i, \qquad i = 1, \ldots, 4N_k. \tag{2.38}$$

being $\mathcal{L} = e_k - e_p$ the Lagrangian function, which includes the normalized kinetic and potential energies of the system, and Q_i the generalized forces. The kinetic energy of the system, normalized over the term $m_1 g L_1$ reads

$$e_k = \sum_{k=1}^{N_k}\left(\frac{1}{2}\sigma_k \boldsymbol{v}^{T}_{k} \cdot \boldsymbol{v}_k + \frac{1}{2}{\boldsymbol{\omega}^{k}_{BE}}^{T} \cdot \bar{\boldsymbol{\iota}}^{k}_{G} \cdot \boldsymbol{\omega}^{k}_{BE}\right) = \frac{1}{2}\dot{\boldsymbol{x}}^{T}_{s} \cdot \bar{\boldsymbol{M}} \cdot \dot{\boldsymbol{x}}_s \tag{2.39}$$

where $\sigma_k = m_k/m_1$ and the tensor $\bar{\boldsymbol{M}} \in \mathbb{R}^{4N_k \times 4N_k}$,

$$\bar{\boldsymbol{M}} = \sum_{k=1}^{N_k}\left(\bar{\boldsymbol{\Upsilon}}^{T}_{k} \cdot \bar{\boldsymbol{\Upsilon}}_k + \bar{\boldsymbol{\Phi}}^{T}_{k} \cdot \bar{\boldsymbol{\iota}}^{k}_{G} \cdot \bar{\boldsymbol{\Phi}}_k\right) \tag{2.40}$$

Similarly, the normalized potential energy is

$$e_p = -\sum_{k=1}^{N_k} \sigma_k \boldsymbol{r}_k \cdot \boldsymbol{k}_E, \tag{2.41}$$

where the term $\boldsymbol{r}_k \cdot \boldsymbol{k}_E$ is found by taking the third component of the Eq. 2.14,

$$\boldsymbol{r}_k \cdot \boldsymbol{k}_E = -\left[\left(x_A^k c\theta_k + z_A^k s\theta_k\right) s\gamma_k - \left(\xi_k - x_A^k s\theta_k + z_A^k c\theta_k\right) c\eta_k c\gamma_k - \zeta_k s\eta_k c\gamma_k\right] \tag{2.42}$$

The aerodynamic forces of the $\{k\}$-kite, $\boldsymbol{F}_k^A \equiv m_1 g \boldsymbol{f}_k^A$, and its torque about point G_k, $\boldsymbol{M}_k^A \equiv m_1 g L_1 \boldsymbol{m}_k^A$, are non-conservative, and they should be incorporated to the equations of motion. Then the generalized forces in Eq. 2.38 reads

$$Q_i = \sum_{n=1}^{N_k} \left(\boldsymbol{f}_n^A \cdot \frac{\partial \boldsymbol{v}_n}{\partial \dot{x}_{s_i}} + \boldsymbol{m}_n^A \cdot \frac{\partial \boldsymbol{\omega}_{BE}^n}{\partial \dot{x}_{s_i}} \right), \qquad i = 1, \ldots, 4N_k. \tag{2.43}$$

A simple linear aerodynamic model, already implemented in previous airborne wind energy simulators (see [14]), is used to introduce the normalized aerodynamic force, $\boldsymbol{f}_k^A$, and torque about G_k, $\boldsymbol{m}_k^A$. The model then writes the S_E-components of the aerodynamic force as

$$\boldsymbol{f}_k^A = \mu_k {v_k^A}^2 \left[\left(C_{x0} + C_{x\alpha}\alpha_k\right) \boldsymbol{i}_B^k + C_{y\beta}\beta_k \boldsymbol{j}_B^k + \left(C_{z0} + C_{z\alpha}\alpha_k\right) \boldsymbol{k}_B^k \right] \tag{2.44}$$

and of the torque as

$$\begin{aligned} \boldsymbol{m}_k^A = \mu_k {v_k^A}^2 \Big[& \epsilon_k^b \left(C_{l\beta}\beta_k + C_{lp} p_k\right) \boldsymbol{i}_B^k + \\ & + \epsilon_k^c \left(C_{m0} + C_{m\alpha}\alpha_k + C_{mq} q_k\right) \boldsymbol{j}_B^k + \epsilon_k^b \left(C_{n\beta}\beta_k + C_{nr} r_k\right) \boldsymbol{k}_B^k \Big] \end{aligned} \tag{2.45}$$

with $\boldsymbol{v}_k^A = \boldsymbol{v}_k - \boldsymbol{v}_w$ the aerodynamic velocity, $\mu_k \equiv \rho S_k L_1 / 2m_1$, $\epsilon_k^b = b_k / L_1$, $\epsilon_k^c = c_k / L_1$, $p_k = P_k b_k / 2V_T$, $q_k = Q_k c_k / V_T$, $r_k = R_k b_k / 2V_T$, ρ the air density, and V_T a reference velocity. Here, P_k, Q_k and R_k are the respective roll, pitch and yaw components of the angular velocity of the $\{k\}$-kite. The attack and sideslip angles are given by

$$\alpha_k = \arctan\left(\frac{\boldsymbol{v}_A^k \cdot \boldsymbol{k}_B^k}{\boldsymbol{v}_A^k \cdot \boldsymbol{i}_B^k}\right), \quad \beta_k = \arcsin\left(\frac{\boldsymbol{v}_A^k \cdot \boldsymbol{j}_B^k}{|\boldsymbol{v}_A^k|}\right) \tag{2.46}$$

It is of significant interest to sated that the model has been implemented over the premise that all the kites are similar and presents the same stability derivatives.

2.4.2 Equations of motion

Making use of the Einstein summation convention, Eq. 2.38 becomes

$$M_{ij}\ddot{x}_{s_j} + \frac{\partial M_{ij}}{\partial x_{s_l}} \dot{x}_{s_l} \dot{x}_{s_j} - \frac{1}{2} \frac{\partial M_{jl}}{\partial x_{s_i}} \dot{x}_{s_j} \dot{x}_{s_l} + \frac{\partial e_p}{\partial x_{s_i}} = \sum_{k=1}^{N_k} \left(f_{k_l}^A \Upsilon_{k_l i} + m_{k_l}^A \Phi_{k_l i} \right) \tag{2.47}$$

where $f_{k_l}^A$ and $m_{k_l}^A$ are the l-components of vectors $\boldsymbol{f}_k^A$ and $\boldsymbol{m}_k^A$ respectively. As can be appreciated, the Einstein formulation allows to write down all the $4N_k$ equations describing the motion of the system, each one referred to each of the state variables x_{s_i}, in a very compact form.

All these equations are written in terms of the state vector variables and their derivatives, so for convenience, an extended state vector is introduced as

$$\boldsymbol{u} = [\boldsymbol{x}_s \; \dot{\boldsymbol{x}}_s] \tag{2.48}$$

and the system of first order differential equations covered in Eq. 2.47 is written in the form,

$$\frac{d\boldsymbol{u}}{d\tau} = \boldsymbol{f}\left(\boldsymbol{u}, \tau; \boldsymbol{p}\right) \tag{2.49}$$

where vector $\boldsymbol{p}$ gathers all the dimensionless parameters of the model. This set of differential equations obtained is very appropriate to make complex calculations like the determination of periodic orbits or to study the system stability. Because τ appears explicitly in the right hand side of Eq. 2.49, the system is non-autonomous.

2.4.3 Limitations and verification of the model

Tethers tensions

Once the equations of motion are integrated and $\boldsymbol{x}_s$, $\dot{\boldsymbol{x}}_s$ and $\ddot{\boldsymbol{x}}_s$ are known, the system should satisfy a set of conditions to be valid from a physical point of view. Essentially, these conditions has to do with the tethers, which should be under traction at any instant, that is, the constraint tension forces should be positive along the time.

As stated, the Langrangian formulation allows us to deploy a system in the form covered in Eq. 2.49, where the constrain forces, used to deploy the previous kinematic calculations, do not appear explicity. This fact suggests that, for validating the model, the classical Newton´s dynamic formulation should be implemented.

In this way, the S_E and S_B^k components of the linear and angular acceleration respectively are computed as

$$\dot{\boldsymbol{v}}_k = \bar{\boldsymbol{\Upsilon}}_k \cdot \ddot{\boldsymbol{x}}_s + \frac{\partial \bar{\boldsymbol{\Upsilon}}_k}{\partial \boldsymbol{x}_s^k} \cdot \dot{\boldsymbol{x}}_s^k \cdot \dot{\boldsymbol{x}}_s \tag{2.50}$$

$$\dot{\boldsymbol{\omega}}_{BE}^k = \bar{\boldsymbol{\Phi}}_k \cdot \ddot{\boldsymbol{x}}_s + \frac{\partial \bar{\boldsymbol{\Phi}}_k}{\partial \boldsymbol{x}_s^k} \cdot \dot{\boldsymbol{x}}_s^k \cdot \dot{\boldsymbol{x}}_s \tag{2.51}$$

The tether tensions normalized over $m_1 g$ are

$$\boldsymbol{t}_{A_\pm}^k = \lambda_{A_\pm}^k \boldsymbol{u}_{A_\pm}^k, \qquad \boldsymbol{t}_{C_\pm}^k = \lambda_{C_\pm}^k \boldsymbol{u}_{C_\pm}^k \tag{2.52}$$

with $\boldsymbol{u}_{A_\pm}^k \equiv \overrightarrow{A_k^\pm C_{k-1}^\pm} / \mid \overrightarrow{A_k^\pm C_{k-1}^\pm} \mid$ and $\boldsymbol{u}_{C_\pm}^k \equiv \overline{C_k^\pm A_{k+1}^\pm} / \mid \overline{C_k^\pm A_{k+1}^\pm} \mid$ the unitary vectors in the direction of the k and $k+1$ pair of lines respectively, and $\lambda_{A_\pm}^k$ and $\lambda_{C_\pm}^k$ the magnitudes of the normalized tensions.

A physically valid trajectory should verify that the tethers tensions are positive at every time, that is $\boldsymbol{t}_A^\pm(\tau) > 0 \; \forall \; \tau$. Applying then, the Newton´s Second law, equations of motion reads

$$\sigma_k \dot{\boldsymbol{v}}_k = \sigma_k \boldsymbol{k}_E + \boldsymbol{f}_k^A + \sum_{j=\pm} \left(\boldsymbol{t}_{A_j}^k + \boldsymbol{t}_{C_j}^k \right) \tag{2.53}$$

$$\bar{\boldsymbol{\iota}}_G^k \cdot \dot{\boldsymbol{\omega}}_{BE}^k + \boldsymbol{\omega}_{BE}^k \times \left(\bar{\boldsymbol{\iota}}_G^k \cdot \boldsymbol{\omega}_{BE}^k \right) = \boldsymbol{m}_k^A + \sum_{j=\pm} \left(\overline{G_k A_k^j} \times \boldsymbol{t}_{A_j}^k + \overline{G_k C_k^j} \times \boldsymbol{t}_{C_j}^k \right) \tag{2.54}$$

Here, appears then the influence of the aerodynamic model, the inertia of the kites and also the constraint forces due to the lines. The correct implementation of the simulator requires then to

solve, separately from Eq. 2.49, the classical Newton–Euler equations of motion above together with the constraints of the tethers. These two formulations should be checked then to provide the same trajectories up to the error of the numerical integrators.

Kite positioning and aerodynamic limitations

The selected aerodynamic model given by Eqs. 2.44 and 2.45 is not very accurate since its linearity condition makes it does not account for stall and for the maximum sideslip angle. The limitations of the model then state that, obviously, it is only valid for angles of attack below stall, $\alpha_k(\tau) < \alpha_k^{stall}$, and for values of the sideslip angle modulus below certain maximum, $|\beta_k(\tau)| < \beta_k^{max}$.

Furthermore, regarding the kites positioning, the model requires that the kites should be inside the wind window, meaning that $\boldsymbol{r}_k \cdot \boldsymbol{i}_E < 0$ and $\boldsymbol{r}_k \cdot \boldsymbol{k}_E < 0 \; \forall \; k$.

Chapter 3

Equilibrium positions and stability analysis

3.1 Introduction

This chapter searchs to show that a train of N_k kites can fly in cross-wind conditions in a stable way without implementing any type of control strategy. Concretely, among the following sections, different system configurations depending on the number of kites, are going to be studied. As stated in [14], the model involving only one kite is an interesting matter since such a configuration is very simple and robust. Hence, it is decided to study first the one-kite configuration, allowing to understand first the dynamics of an unique kite, to then recognize the system normal modes, and to get a more precise understanding of the dynamics of the entire system.

Anyway, in this chapter, for the different model configurations adopted, the AWES stability is evaluated from two points of view. On the one hand, using an approach in which the equations of motion are reduced to a first-order system of linear equations, allowing to obtain the eigenmodes of the system just by solving an eigenvalues and eigenvectors problem. As it will be seen, the development of the solution to this problem, also allows to calculate different features which will assess for the system stability. On the other hand, solving the non-linear equations of motion covered in Eq. 2.49 by means of a mathematical tool like *ode45* function from MATLAB®.

The work aims to match these two parallel studies to recognize the system normal modes, and to compare the results with the well-known ones of a conventional aircraft. To evaluate this fact, a brief description of the aircraft normal modes should be introduced. Remembering, the normal modes of a common aircraft are the so-called, *Phugoid* and *Short Period* modes for the longitudinal motion, and *Rolling Convergence*, *Spiral* and *Dutch Roll* modes for the lateral-directional one.

In first place, regarding the longitudinal motion of the aircraft, the *Phugoid* mode results to be a lightly damped low-frequency oscillation in the longitudinal component of the speed, which couples into pitch attitude and height leading to a continuous exchange of kinetic and potential energy. During the disturbance, the angle of attack remains substantially constant. At the same time, the *Short Period* is a heavily damped oscillation in pitch, in which the velocity is remained approximately constant, and the angle of attack oscillates with amplitude and phase not much different from that of the pitch angle.

On the other hand, regarding the lateral-directional modes, the *Rolling Convergence* is a non-oscillatory mode in which the disturbance in roll angle makes differences in effective angle of attack, with a substainable change in differential lift and rolling moment. The *Spiral* represents another non-oscillatory mode as a complex coupled motion in roll, yaw and sideslip, and finally, the *Dutch Roll* represents a damped oscillation in yaw coupled into roll and also, but less, into sideslip.

3.2 Equilibrium position

To develop an appropriate study about the stability of the system without controls, it is required to find a stable equilibrium position of the system since the stability should be evaluated very close near to this equilibrium point. Under steady wind conditions (v_w is constant), the system admits a

symmetric equilibrium state (lateral-directional variables are zero), i.e. a system state, $\boldsymbol{u}(\tau) = \boldsymbol{u}^*$ that makes $\boldsymbol{f}(\boldsymbol{u}^*) = 0$. Such a condition is verified by the implementation of a Newton´s method with initial conditions in the form of an state vector like $\boldsymbol{x}_s^* = [0\ \gamma_1^*\ 0\ \theta_1^*\ \cdots\ 0\ \gamma_{N_k}^*\ 0\ \theta_{N_k}^*]$, where the longitudinal variables are constants ($\dot{\boldsymbol{x}}_s^* = 0$).

The definition of the system given by Eq. 2.49, is obviously related to the nondimensional parameters defining the wing geometry, inertia properties, stability derivatives, and weather conditions among other parameters provided by the vector $\boldsymbol{p}$. Hence, the equilibrium state is also influated by these characteristics. Furthermore, the difficulty of the problem is increased when one takes into account that the solution obtained should be a physical solution. That means that the state equilibrium should be inside the ranges defined by the model limitations (see Section 2.4.3). So then, a correct configuration in terms of system dimensional parameters should be selected. Tables 3.1 and 3.2 shows the parameters, common for all the kites, selected for finding a stable equilibrium for one and two-kites configurations.

Symbol	Value	Symbol	Value	Symbol	Value
x_A	0.17 m	y_A	2.9 m	z_A	2 m
x_C	0 m	y_C	2.83 m	z_C	2 m
I_x	21.1 $\mathrm{kg \cdot m^2}$	I_y	4.66 $\mathrm{kg \cdot m^2}$	I_z	18.0 $\mathrm{kg \cdot m^2}$
m	4.0 kg	h	3.2 m	h_G	2 m
A	14.4 $\mathrm{m^2}$	c	1.5 m	b	5.8 m
β_{max}	15°	α_s	25°	V_T	3 $\mathrm{m \cdot s^{-1}}$
L	50 m	ρ	1.225 $\mathrm{kg \cdot m^3}$	v_w	7 $\mathrm{m \cdot s^{-1}}$

Table 3.1: Dimensional parameters used in the simulations giving.

Here, L is a reference value of the line length. It was decided to evaluate the system with lines of different length depending on the kite which they attach. Then, the length of the tethers is defined as, $L_k = L + k,\ \forall\ k$. For the cases evaluated within this document, there is no too much difference between the lines length, since the number of kites is small.

Symbol	Value	Symbol	Value	Symbol	Value
C_{x0}	-0.065	$C_{x\alpha}$	0.18	$C_{y\beta}$	-1.57
C_{m0}	0.4	$C_{m\alpha}$	-0.8	C_{mq}	-0.5
$C_{l\beta}$	0.7	C_{lp}	-0.85	$C_{n\beta}$	-0.046
C_{nr}	-0.34	C_{z0}	0.116	$C_{z\alpha}$	-2.97

Table 3.2: Non-dimensional stability coefficients.

The current model developed in Chapter 2 is valid for any system of N_k rigid bodies towed to the ground by two tethers. A large list of different lifting devices like aircraft-like kites, acrobatic kites, and power kites, could be simulated. The particular shape of the body enters in the model through the value of the aerodynamic coefficients, and through the values of the normalized moments of inertia. This work analyzes the case of power kites and uses reference values from [2]. Despite, a parametric survey (not shown in this work) varying the position of the tether attachment points,

the wind velocity and some stability coefficients from values of [2] revealed that the symmetric equilibrium of the system with one and two kites, is stable for a certain combination. Although it would result interesting to get a configuration which also makes stable the symmetric equilibrium position for systems with more than two kites, it is out of the scope of this work, resulting of evident difficulty to get it by simple parametric survey.

To find an stable equilibrium state is a very important feature for AWES applycations. Furthermore, the evaluation of the system stability should be performed around a stable equilibrium solution. Once the implemented Newton´s method finds a system equilibrium state fulfilling $\boldsymbol{f} = 0$, in order to study the stability of the solution, the system should be perturbed around it by adding a small perturbation $\boldsymbol{u}_1$ to the equilibrium steady state, substituting $\boldsymbol{u}(\tau) = \boldsymbol{u}^* + \boldsymbol{u}_1(\tau)$ in Eq. 2.49 and, deploying a Taylor expansion, dropping high order terms. In this way, one finds the linear system,

$$\frac{d\boldsymbol{u}_1}{d\tau} = \boldsymbol{J}|_{\boldsymbol{u}^*} \cdot \boldsymbol{u}_1 \tag{3.1}$$

where $\boldsymbol{J}|_{\boldsymbol{u}^*}$ is the Jacobian matrix of the flux $\boldsymbol{f}$ evaluated at the equilibrium state. From flight dynamics for uncontrolled motion covered in [7], it is extracted that this kind of linear system admits solutions of the type $\boldsymbol{u}_1(\tau) \propto \boldsymbol{v}e^{\lambda\tau}$, where λ represents the combination of all the system eigenvalues, and $\boldsymbol{v}$ their related eigenvectors. Both are obtained by solving the problem defined by the characteristic determinant

$$det\left(\boldsymbol{J}|_{\boldsymbol{u}^*} - \lambda\boldsymbol{I}\right) = 0, \tag{3.2}$$

which, once solved, states for the equilibrium stability if all the eigenvalues, $\lambda = n \pm \omega i$, have negative real part, $n < 0,\ \forall\ \lambda$.

Similarly to the aircraft flight dynamics, thanks to the selection of the coordinates and the aerodynamic model used, for such a system, the state variables are decoupled near to the equilibrium position. In other words, the longitudinal and lateral-directional variables can be separated, and then, their correspondent respective eigenmodes. Due to this fact, the Jacobian matrix of the system can be written in the following form,

$$\boldsymbol{J}|_{\boldsymbol{u}^*} = \boldsymbol{J}|^{long}_{\boldsymbol{u}^*} + \boldsymbol{J}|^{lat}_{\boldsymbol{u}^*} \tag{3.3}$$

Along the following sections, this fact will allow to separate the primitive problem in two different ones, due to longitudinal and lateral-directional motions.

3.3 Normal modes

Once obtained separately the system normal modes for the longitudinal and lateral motions, some stability features should evaluated. So as to do that, different parameters must be intruduced. They are:

- Natural frequency, ω_n. Frequency at which the system tends to oscillate in the abscense of any damping force. It is defined for each eigenmode as,

$$\omega_n = \sqrt{\omega^2 + n^2} \tag{3.4}$$

- Period, T. Being referred to the disturbance quantities of any oscillatory mode, it is the time spent by the disturbance to accomplish with one oscillation. It is given as,

$$T = \frac{2\pi}{\omega} \tag{3.5}$$

- Damping ratio, ζ. Dimensionless parameter describing how any quantity decay or not after a disturbance. It is defined as,

$$\zeta = -\frac{n}{\omega_n} \tag{3.6}$$

- Time to half, t_{half}. Time for any disturbance quantity to double or halve itself. It reads

$$t_{half} = \frac{ln\ 2}{|n|} = \frac{ln\ 2}{|\zeta|\,\omega_n} \tag{3.7}$$

- Cycles to half, N_{half}. Number of cycles for any oscillatory disturbance quantity to double or halve itself. Its expression reads

$$N_{half} = \frac{ln\ 2}{2\pi}\ \frac{\omega}{|n|} = \frac{ln\ 2}{2\pi}\ \frac{\sqrt{1-\zeta^2}}{|\zeta|} \tag{3.8}$$

The calculation and discussion of those parameters, principally allow to assess for different stability features and system characteristics, as well as to recognize the physical motion of the system due to the different eigenmodes.

3.4 One-kite configuration

As an initial approach, in order to understand individually the dynamics of the kites selected for the simulations, the one-kite configuration is studied.

3.4.1 Equilibrium state

Before entering to discuss the eigenmodes of such as configuration, the equilibrium state achived by terms of the Newton´s method should be evauated. Here, this state vector is given as,

$$\boldsymbol{x}_s^* = [0 \quad 0.43387 \quad 0 \quad -0.02754] \tag{3.9}$$

where the state variables are given in radians. Making more visual the information resultant from this equilibrium state vector $\boldsymbol{x}_s^*$, one can propose to write its components in degrees. In this way, the longitudinal variables result as $\gamma_1 = 24.9°$ and $\theta_1 = -1.6°$. By simple inspection to those values, and noticing that, for the current model the AoA of each kite is written as the sum of its both longitudinal state variables, γ and θ, then, the attack and sideslip angles result to be $\alpha_1 = 23.6°$ and $\beta_1 = 0°$ respectively. Since they are contained into the ranges defined by the limitations of the model and, being both physical solutions (the kite does not adopt state variables greater than $\pi/2$ radians), it can be stated that they assess for a correct equilibrium state. Together with this information, the simulation implemented in MATLAB® provides the sketch shown in Fig. 3.1, where a visualization of the kite equilibrium position is shown.

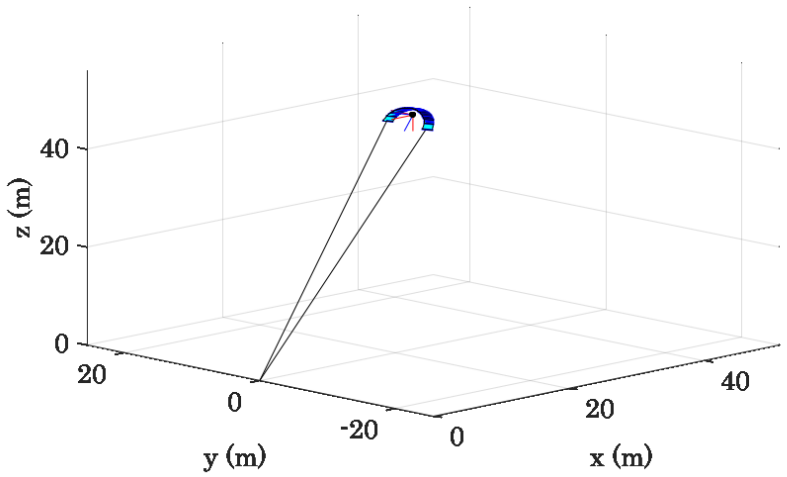

Figure 3.1: Sketch of the AWES one-kite configuration 3D equilibrium state.

3.4.2 Longitudinal dynamics

Linear stability analysis close to the equilibrium state

In this section, the longitudinal stability of the system is evaluated by solving the eigenvalues and eigenvectors problem defined as

$$det\left(\boldsymbol{J}\big|_{\boldsymbol{u}^*}^{long} - \lambda \boldsymbol{I}\right) = 0, \tag{3.10}$$

which results from the system of linear equations that is obtained when dropping the higher-than-one order terms from the Taylor expansion of $\boldsymbol{f}$, in 2.49.

Four eigenvalues are obtained from this problem, all of them, resulting as subsidence or convergence modes denoted by their real negative values. In Table 3.3, those eigenvalues are collected, together with some of their relevant features described in Sec. 3.3. Before discussing any of these features, it is interesting to remember the aircraft dynamics. Making a comparison, it can be stated that in longitudinal motion, the analyzed model does not present any important similarity with the longitudinal motion of an aircraft.

Mode	*Eigenvalue*	*Natural Frequency,* ω_n $[rad \cdot s^{-1}]$	*Period,* T $[s]$	*Time to half,* t_{half} $[s]$	*Cycles to half,* N_{half} $[cycles]$
λ_1	-55.21511	55.21511	–	0.01255	–
λ_2	-0.91806	0.91806	–	0.75501	–
λ_3	-16.13033	16.13033	–	0.04297	–
λ_4	-12.28617	12.28617	–	0.05642	–

Table 3.3: Eigenvalues from longitudinal dynamics.

Data covered in Table 3.3 secures the system longitudinal stability, since $n < 0,\ \forall\ \lambda$. Moreover, one can also appreciate the relevant relation between the values of ω_n and t_{half}. For greater values of the natural frequency, lower values of the time to halve are adopted. This fact was predicted

by Equation 3.7. However, not too much more information can be extracted from this data. Due to this, in order to achive a more accurate knowledge about the normal modes, one should make attention to their relative eigenvectors. Those ones are given in Table 3.4.

	$\boldsymbol{v}_1$		$\boldsymbol{v}_2$		$\boldsymbol{v}_3$		$\boldsymbol{v}_4$	
	Magn.	*Phase*	*Magn.*	*Phase*	*Magn.*	*Phase*	*Magn.*	*Phase*
γ_1	0.00062	180°	0.72741	0°	0.00004	180°	0.0024	180°
θ_1	0.0181	0°	0.11626	0°	0.06188	180°	0.08109	180°
$\dot{\gamma}_1$	0.0345	0°	0.66781	180°	0.00058	0°	0.02945	0°
$\dot{\theta}_1$	0.99924	180°	0.10673	180°	0.99808	0°	0.99627	0°

Table 3.4: Longitudinal eigenvectors (polar form).

Here, it can be extracted how for each eigenmode, the dominant variables are different, fact which qualitatively explain the physical meaning of each of the modes. In this matter, as much as in the first mode, as in the third and fourth ones, the influence of $\dot{\theta}_1$ results of paramount relevance. Matching this information with the one extracted from the eigenvalues, one can predict the relative similarity between these three modes, being the relevant factor which distinguish them, the assumed relevance by secondary variables. Anyway, the rest of variables are, at least two orders of magnitude smaller than $\dot{\theta}_1$.

Regarding the eigenvector referred to the second mode, an important fact is due to the difference in magnitude assessed between γ_1 and θ_1, as well as between their relative derivatives. The variables γ_1 and its derivative are the predominant ones, meanwhile θ_1 and $\dot{\theta}_1$ also present some, but smaller, relevance. Essentially, this mode can be physically understood as a very fast convergent rotational motion of the kite around its pitch axis, as a coupling between their two longitudinal variables.

Non-linear stability analysis close to the equilibrium state

This section covers the results obtained by the direct integration of Eq. 2.49. In order to find a solution for each different eigenmode by means of *ode45*, the system equilibrium state is perturbed in the direction of each of the eigenvectors previously collected. Hence, the initial conditions are written as,

$$\boldsymbol{u}_0 = \boldsymbol{u}^* + \epsilon\, \boldsymbol{v}_i \tag{3.11}$$

where ϵ is a real infinitesimal value, in this case, concretely $\epsilon = 10^{-2}$, and $\boldsymbol{v}_i$ represents the vector containing the real part of the eigenvector (with also lateral state variables) referred to the i-eigenmode. The transient evolution of the longitudinal state variables when the system equilibrium state is perturbed in the direction of the different modes is graphically represented in figures 3.2 and 3.3.

Making attention to the first, third and fourth modes, as it was forecasted, the longitudinal variables transients reveal how these modes gather similar characteristics. The results assess also for the fact that relates them with the phase angle of their respective eigenvectors. Meanwhile for phase angles with values between 90° and 270°, the perturbation value is smaller than the equilibrium one, for phase angles inside the remaining range, the perturbation contrarily adopt

higher values than the equilibrium. In parallel, as described by data from Table 3.4, for the third and fourth modes, θ_1 and $\dot{\theta}_1$ behave in very similar ways. That is related to their quite similar perturbation values gathered by their respective eigenvectors. In rough outlines, the results obtained match with the data collected from the linear approach.

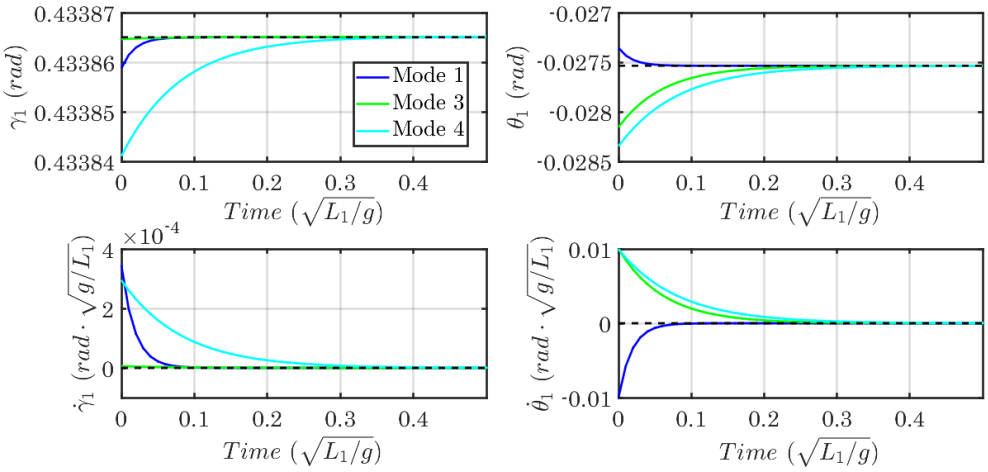

Figure 3.2: Transient disturbances of the longitudinal state variables.

The same occurs with the second mode. This mode is shown separately from the others since in its direction, the kite motion stabilizes for a period of time with one order of magnitude greater than the previous ones, fact which was predicted when obtaining t_{half} values shown in Table 3.3.

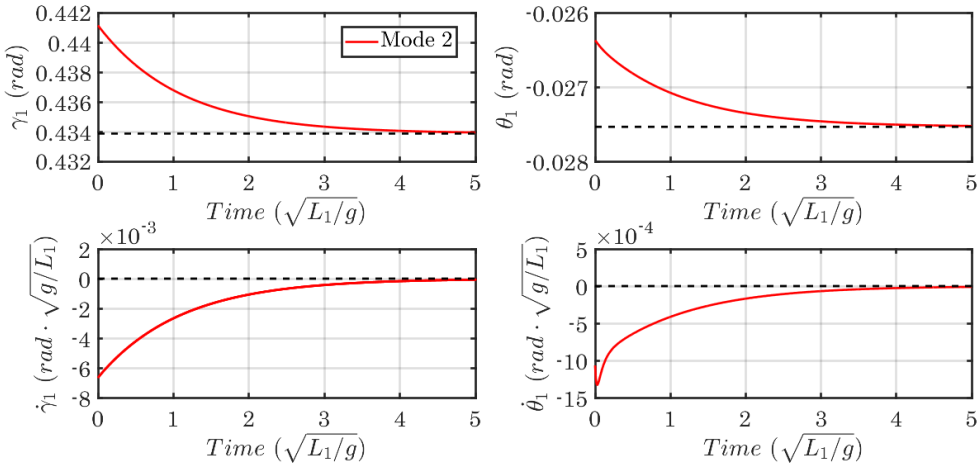

Figure 3.3: Transient disturbances of the longitudinal state variables.

Comparing both figures, perturbations for angular velocities $\dot{\gamma}_1$ and $\dot{\theta}_1$, account for a big difference between them in terms of its order of magnitude. This fact was also predicted during the first linear analysis. Obviously, due to the importance of $\dot{\theta}_1$ in the faster convergence modes of Fig.

3.2, and due to its relative low relevance in the second mode, significant differences are accounted principally for this variable.

3.4.3 Lateral-directional dynamics

Linear stability analysis close to the equilibrium state

As in previous section, in order to study the lateral-directional stability following the linear approach, the problem of eigenvalues and eigenvectors defined as

$$det\left(\boldsymbol{J}|_{\boldsymbol{u}^*}^{lat} - \lambda \boldsymbol{I}\right) = 0, \tag{3.12}$$

is proposed. Once solved, again four subsidence modes, whose eigenvalues are shown in Table 3.5, are obtained. Similarly to the analysis of the AWES longitudinal stability, a comparison with the aircraft motion should be performed. In this way, by simple inspection, one can assess for certain similarities since, although the kite lateral dynamics do not present any oscillatory mode as a solution, two of its four convergence modes could be related to the aircraft lateral *Spiral* and *Rolling Convergence* modes. However, in order to correctly discuss this features, due to the shortage of information provided by the eigenvalues, one must make attention to their related eigenvectors. Here, for the correct and accurate evaluation of the results as well as to understood correctly the physical meanings of the obtained eigenmodes, it requires to be stated that, for the kinematic model developed in this work, the angles φ and η, account respectively for the vector state yaw and roll angles.

Mode	*Eigenvalue*	*Natural Frequency*, $\omega_n\ [rad \cdot s^{-1}]$	*Period*, $T\ [s]$	*Time to half*, $t_{half}\ [s]$	*Cycles to half*, $N_{half}\ [cycles]$
λ_1	-104.82069	104.82069	–	0.00661	–
λ_2	-52.40111	52.40111	–	0.01323	–
λ_3	-0.09083	0.09083	–	7.63126	–
λ_4	-0.03521	0.03521	–	19.6861	–

Table 3.5: Eigenvalues from lateral-directional dynamics.

Looking at the eigenvectors collected in Table 3.6, one can extract the fact that they seems to follow certain duality, since the state variables behave in similar ways for the first and second pair of modes repectively. In this way, the first and second modes behave as modes with only two degrees of freedom (angular velocities in yaw and roll components), being $\dot{\varphi}_1$ their dominant variable. Trying to make an intensive study about the physics, one can state that, when perturbed the state equilibrium position in the direction of one of these two modes, the kite motion is based on a coupling of the yawing and rolling components of the angular velocity.

On the other hand, the third and fourth modes are presented as ones in which the dominant variable is the roll angle. Concretely, the third one, being a mode for which all the other variables adopt values with at least one order of magnitude smaller than η_1, presents significant similarities with the *Rolling Convergence* mode. Due to this, the physical understanding of this mode results

easy to explain, being a mode that consist of an almost pure rotation around the longitudinal axis of the kite. The fourth mode seems to behave as one with only two degrees of freedom. However, in this case the mode can be explained as a disturbance in roll angle which, due to the change in differential lift, couples with a yaw motion. In other words, in this mode, the kite behaves similarly to the aircraft when perturbed in the direction of the *Dutch Roll* mode, but without acquiring any oscillation feature, more than a convergent behaviour.

	$\boldsymbol{v}_1$		$\boldsymbol{v}_2$		$\boldsymbol{v}_3$		$\boldsymbol{v}_4$	
	Magn.	*Phase*	*Magn.*	*Phase*	*Magn.*	*Phase*	*Magn.*	*Phase*
φ_1	0.00878	0°	0.01822	0°	0.07081	0°	0.25196	180°
η_1	0.00373	0°	0.00565	180°	0.99338	0°	0.9671	180°
$\dot{\varphi}_1$	0.92033	180°	0.9549	180°	0.00643	180°	0.00887	0°
$\dot{\eta}_1$	0.39102	180°	0.2963	0°	0.09023	180°	0.03406	0°

Table 3.6: Lateral-directional eigenvectors (polar form).

Non-linear stability analysis close to the equilibrium state

The results obtained by the direct integration of the equations of motion, now for lateral dynamics, are covered in this section. Here, as before, the mathematical tool *ode45* from MATLAB® is used for getting the transients of the lateral state vector variables when the equilibrium state is perturbed in the direction of each of the previously obtained eigenmodes. Those transients of the lateral-directional state variables are graphically represented in figures 3.4 and 3.5.

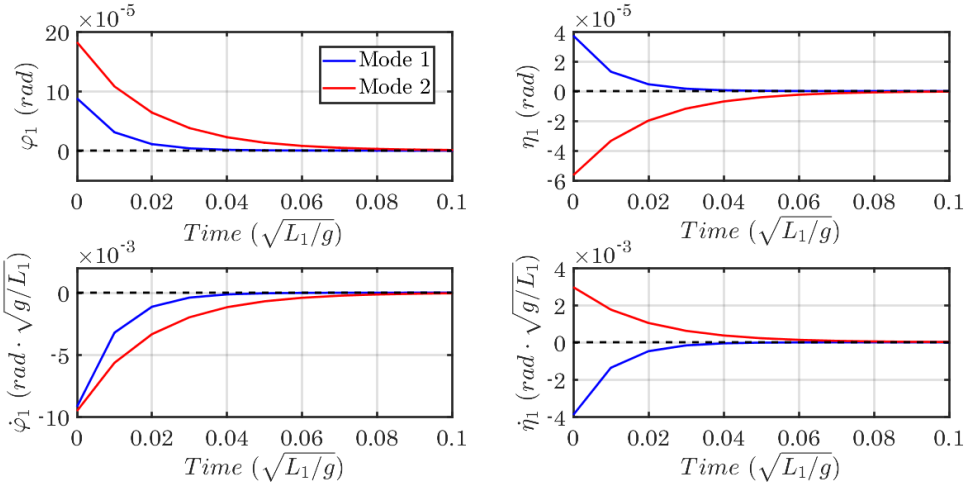

Figure 3.4: Transient disturbances of the lateral-directional state variables.

Here, the results are consistent with the ones obtained from the linearized problem, showing the forecasted very marked duality in the resultant four modes, as well as, like in previous section, their relation with the phase angle of their respective eigenvectors. In first instance, the first pair of modes is shown in Fig. 3.4, where the also predicted characteristic assessing for their very fast convergence features (see values for t_{half} in Table 3.5), can be appreciated.

Regarding the second pair of modes, the influence of the roll angle becomes visible when comparing the order of magnitudes of the different variables. Furthermore, their very long time to converge is contrasted with the modes represented in figure above. This fact, was also accounted by the values of t_{half} get by the linear approach.

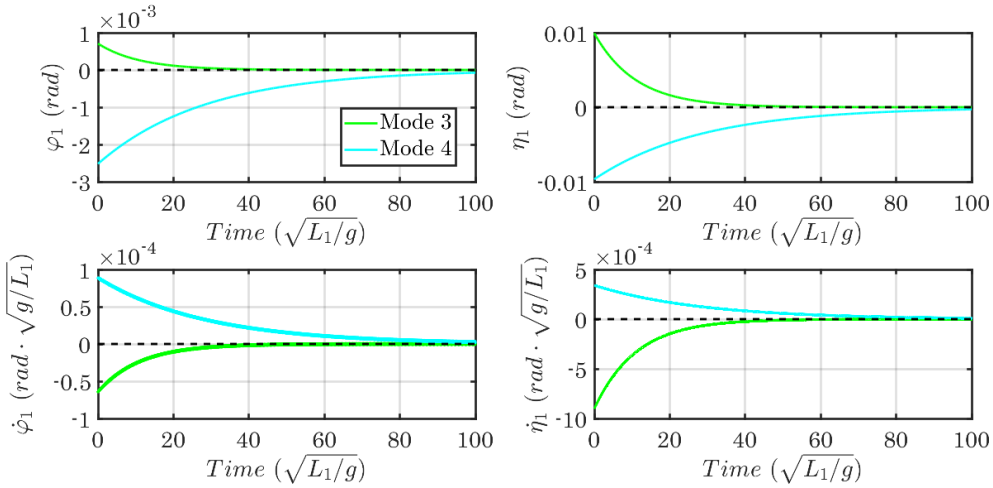

Figure 3.5: Transient disturbances of the lateral-directional state variables.

3.5 Two-kites configuration

Until here, the dynamics of the system involving only one kite has been studied, fact which allowed to evaluate the similarities of the system dynamics with the well-known aircraft conventional one. Despite, from this point on, it is not useful to introduce any comparison with the aircraft dynamics, since, although forecasting processes could predicted that different modes appearing could be decoupled for each of the kites, now the system starts to be composed by different rigid bodies whose state variables depend and affect to the whole system. In other words, for systems with more than one kite, the evident extension of the state vector does not allow to compare the stability features with the ones of the aircraft.

3.5.1 Equilibrium state

The equilibrium state for this configuration is given by the state vector

$$\boldsymbol{x}_s^* = [0 \;\; 0.40536 \;\; 0 \;\; -0.08728 \;\; 0 \;\; 0.43848 \;\; 0 \;\; -0.03216 \;\; 0] \tag{3.13}$$

where the variables, belonging to the ranges proposed by the limitations of the model, are given in radians. To visualize better such as information, longitudinal variables are written in degrees as, $\gamma_1 = 23.23°$, $\theta_1 = -5°$, $\gamma_2 = 25.12°$ and $\theta_2 = -1.84°$. The attack and sideslip angles of each kite result to be then $\alpha_1 = 18.23°$, $\beta_1 = 0°$, and $\alpha_2 = 23.28°$, $\beta_2 = 0°$ respectively. Those values assess

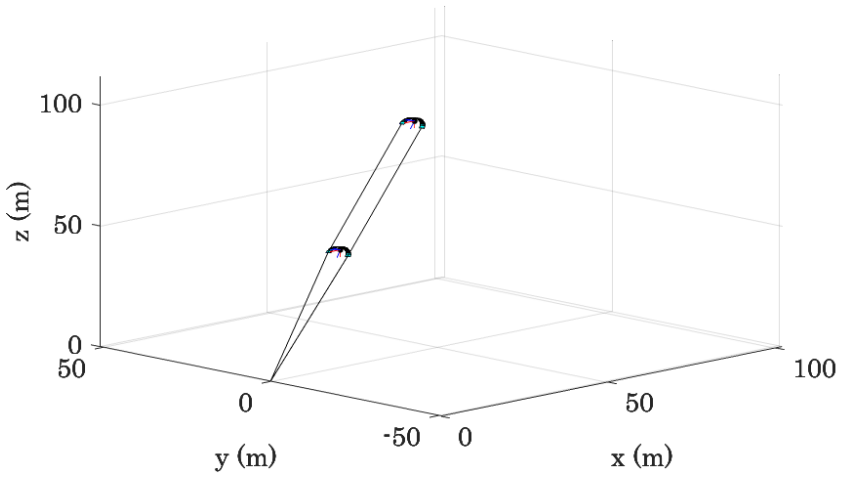

Figure 3.6: Sketch of the AWES two-kite configuration 3D equilibrium state.

for the for a correct AWES equilibrium state. As for the one-kite configuration, the visualization of the system equilibrium is shown at Fig. 3.6.

3.5.2 Longitudinal dynamics

Linear stability analysis close to the equilibrium state

The stability of the system is evaluated in this section by solving the eigenvalues and eigenvectors problem obtained from the linearization of the longitudinal equations of motion. In this case, due to the extension of the state vector, the Jacobian of the system results to be a square matrix with sixteen dimensions. This fact leads to the existance of sixteen eigenvalues, eight of them being longitudinal ones. In this way, the group of solutions for the longitudinal problem is the one collected in Table 3.7.

Mode	*Eigenvalue*	*Nat. Frequency,* ω_n $[rad \cdot s^{-1}]$	*Period,* T $[s]$	*Time to half,* t_{half} $[s]$	*Cycles to half,* N_{half} $[cycles]$
$\lambda_{1,2}$	$-59.51309 \pm 8.65194i$	60.13871	0.10447	0.01165	0.01604
$\lambda_{3,4}$	$-14.19789 \pm 10.20032i$	17.48218	0.35941	0.04882	0.07926
λ_5	-0.54115	0.54115	–	1.28088	–
λ_6	-3.6584	3.6584	–	0.18947	–
$\lambda_{7,8}$	$-7.96668 \pm 3.60923i$	8.74612	0.7184	0.08701	0.04998

Table 3.7: Eigenvalues from longitudinal dynamics.

The found solutions are three oscillatory modes, and two non-oscillatory ones. The longitudinal stability is accounted by the real negative part of those found eigenvalues. Regarding the oscillatory modes, they all result in underdamped oscillations ($\zeta < 1$). An important feature is also their short period of oscillation, fact which, matched together with the small values achieved for t_{half} and N_{half}, states for their very fast convergence nature. Concretely, these modes behave like

almost citically damped convergence modes, presenting similar absolute values for n and ω_n, fact which leads to a damping ratio close to the unity. In parallel, a relevant particularity is due to the two pure subsidence modes, which present values of t_{half} of at least one order of magnitude greater than the oscillatory ones, leading to a slow convergence behaviour.

	$\boldsymbol{v}_{1,2}$		$\boldsymbol{v}_{3,4}$		$\boldsymbol{v}_{7,8}$	
	Magn.	*Ph.*	*Magn.*	*Ph.*	*Magn.*	*Ph.*
γ_1	0.00032	116.83°	0.0016	185.97°	0.00531	289.28°
θ_1	0.00881	297.69°	0.04585	35.69°	0.10867	204.37°
γ_2	0.00051	186.58°	0.00074	54.4°	0.00666	44.58°
θ_2	0.01409	8.27°	0.03401	309.24°	0.03197	252.66°
$\dot{\gamma}_1$	0.01945	288.56°	0.02789	330.27°	0.04643	84.9°
$\dot{\theta}_1$	0.52966	109.42°	0.80149	180°	0.95046	0°
$\dot{\gamma}_2$	0.03067	358.31°	0.01299	198.71°	0.05826	200.21°
$\dot{\theta}_2$	0.84727	180°	0.59449	93.54°	0.27961	48.29°

Table 3.8: Longitudinal eigenvectors (polar form) for oscillatory modes.

Analyzing the eigenvectors for the oscillatory modes, certain similarities between them can be appreciated. These are principally related to the fact that all of them behave as modes with only two degrees of freedom, being $\dot{\theta}_1$ and $\dot{\theta}_2$ their dominant variables. For the first one, the pitch angular velocity of the second kite governs the motion, as can be appreciated in Fig. 3.7. Here, the evident difference in magnitude between variables, is shown. The fact that γ-variables and their derivatives, as well as θ_1 and θ_2, are not visible for the image scaling, accounts for the insignificant weights they present in this mode.

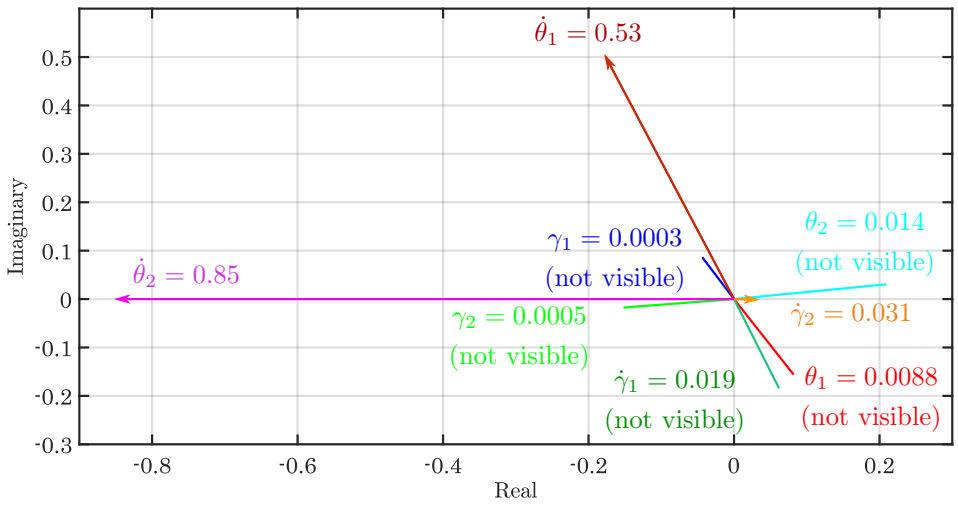

Figure 3.7: Vector diagram for $\boldsymbol{v}_{1,2}$.

Similarly occurs for the second mode. Fig. 3.8 represents the polar of this eigenmode. Comparing the first and second modes vector diagrams, the parallelism between them becomes clear. These

both behaves in quite similar ways, but with the main difference that, while the first one has $\dot{\theta}_2$ as dominant variable, the second one is dominated by $\dot{\theta}_1$.

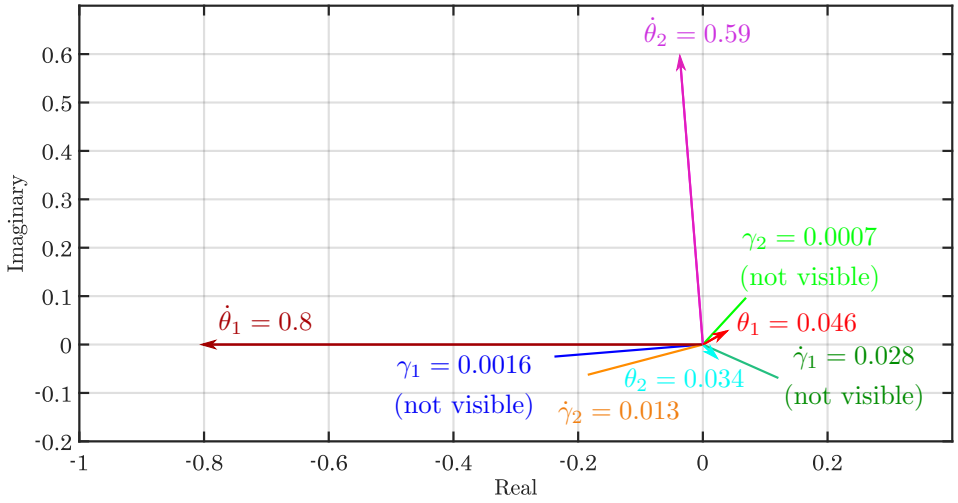

Figure 3.8: Vector diagram for $\boldsymbol{v}_{3,4}$.

Finally, for the third mode referred to $\boldsymbol{v}_{7,8}$, the angular velocity $\dot{\theta}_1$ again becomes the most relevant variable. Here, the difference between this variable with the rest of them, is greater than in the other cases. However, θ_1, probably due to the effect of its derivative, gains some relevance. Such is it, that this mode could be considered as a motion with mainly three DoFs, in which, the high magnitudes of the two coupled variables $\dot{\theta}_1$ and $\dot{\theta}_2$, leads to a significant disturbance in θ_1.

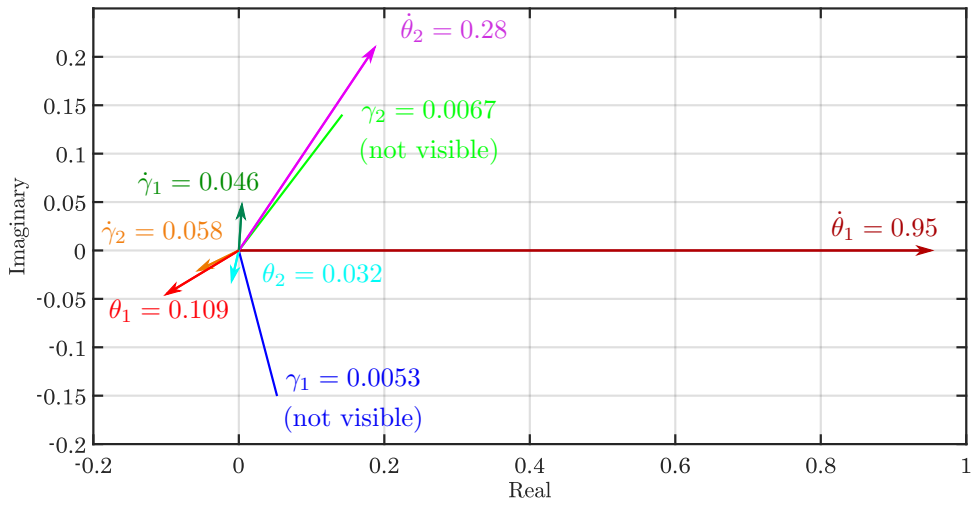

Figure 3.9: Vector diagram for $\boldsymbol{v}_{7,8}$

The eigenvectors of the subsidence modes are collected in Table 3.9. The first of these two modes present one interesting fact that has to do with the evident relevance of practically all the

variables. This fact is denoted by their orders of magnitudes. In that way, while γ-variables are the predominant ones, θ_2 and its derivative are the ones which do not account with too much influence in the motion. The second convergence mode is clearly denoted by the influence of $\dot{\theta}_1$, although variables like θ_1 and $\dot{\gamma}_2$ present also some relevance.

	$\boldsymbol{v}_5$		$\boldsymbol{v}_6$	
	Magnitude	*Phase*	*Magnitude*	*Phase*
γ_1	0.46131	180°	0.02562	0°
θ_1	0.36431	0°	0.25789	0°
γ_2	0.65128	180°	0.04812	180°
θ_2	0.06166	180°	0.00654	180°
$\dot{\gamma}_1$	0.24964	0°	0.09375	180°
$\dot{\theta}_1$	0.19715	180°	0.94347	180°
$\dot{\gamma}_2$	0.35244	0°	0.17604	0°
$\dot{\theta}_2$	0.03337	0°	0.02392	0°

Table 3.9: Longitudinal eigenvectors (polar form) for non-oscillatory modes.

Non-linear stability analysis close to the equilibrium state

This section covers the results obtained by the direct integration of Eq. 2.49. Again, the same procedure is implemented, based on perturbing the equilibrium state of the system in the direction of the eigenvectors previously obtained. The transients of the longitudinal state variables are collected in following figures. In order to make easier the understanding of those graphs, the variables for each of the two kites are separated in different figures.

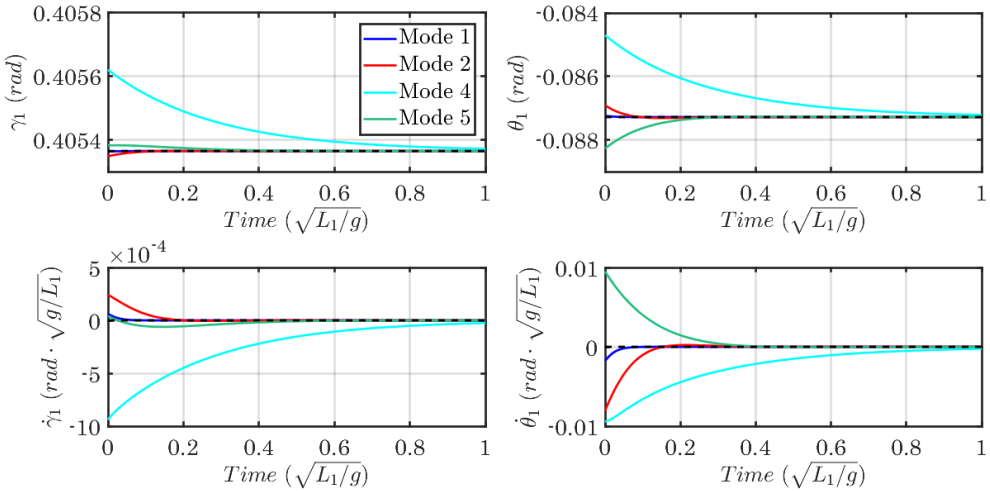

Figure 3.10: Transient disturbances of the longitudinal state variables for the first kite.

On the one hand, the discussion of the first kite is performed. The results are consequent with the ones obtained for the linear approach. Oscillatory modes, as it was predicted, are very damped

modes, almost behaving like critically damped solutions. Furthermore, their rapid convergence features assessed by values of t_{half} contained in Tab. 3.7, are also described.

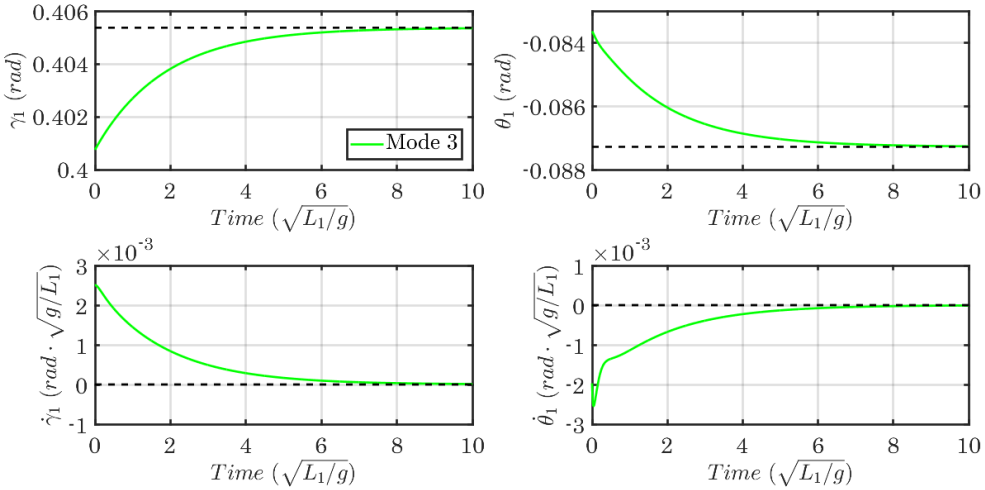

Figure 3.11: Transient disturbances of the longitudinal state variables for the first kite.

The non-oscillatory modes (third and fourth modes) converge respectively for periods of time two and one orders of magnitude higher than previous modes. This fact obligates to draw the transient of the disturbances referred to the first of these two, in a separated figure. Anyway, the fact that those modes converge for relative long periods (in comparison with the oscillatory ones), was also covered by the linear study, thus leading to a good matching of the two solutions.

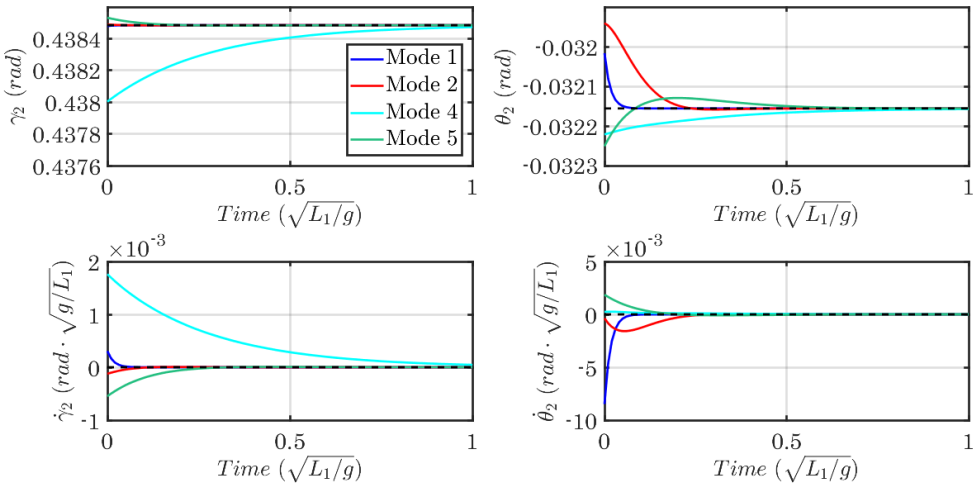

Figure 3.12: Transient disturbances of the longitudinal state variables for the second kite.

On the other hand, the second kite disturbances are evaluated. In Fig. 3.12 and 3.13, the same perturbations behaviour appreciated for the first kite is shown. The values of t_{half} contained in

Tab. 3.7, as well as the close to critically damped behaviour of the oscillatory modes are againg ratified. However, in this case, the underdamped nature of these modes is appreciated for variables θ_2 and its derivative for fifth and second modes respectively.

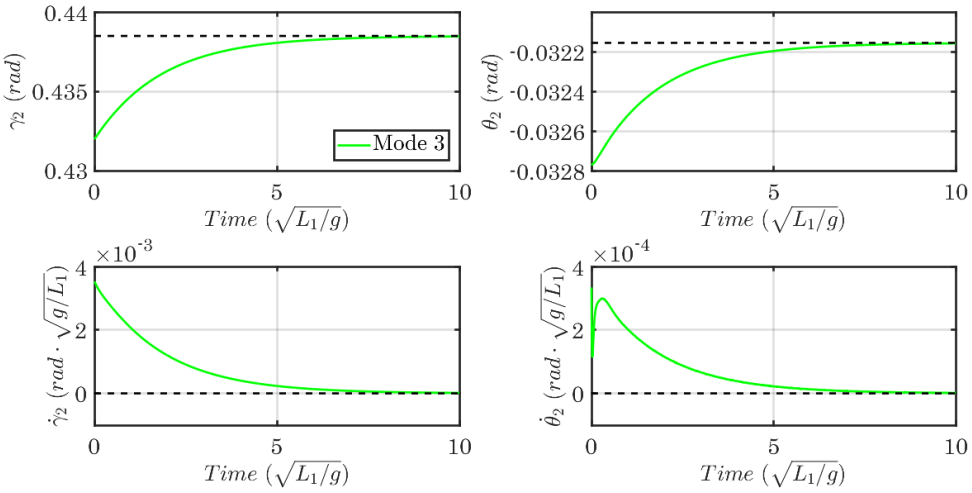

Figure 3.13: Transient disturbances of the longitudinal state variables for the first kite.

As a general instance, looking at Figures 3.11 and 3.13 covering the transient evolution of the first subsidence mode (Mode 3), it is interesting to notice the behaviour of $\dot{\theta}_1$ and $\dot{\theta}_2$ close to the initial perturbation instant. As appreciated, those variables behave with oscillatory behaviours during the first period of time, for almost half a second, then recovering its convergence performance. This fact, curiously contrast with the magnitude of those variables obtained when evaluating the eigenvectors in Tab. 3.9, being these two, the less relevant variables for this mode.

3.5.3 Lateral-directional dynamics

Linear stability analysis close to the equilibrium state

The problem of eigenvalues and eigenvectors defined by the linear approach now finds seven stable modes, six of them non-oscillatory ones. The obtained eigenvalues are shown in Table 3.10. Here a significant fact is extracted from the feature that, although being convergent eigenmodes, the first four modes seems to be paired between them. While first and second modes present similar eigenvalues, the third and fourth ones perform in similar way, presenting all of them performances which stabilize to the equilibrium for significant short periods of time. The two remaining non-oscillatory modes are, however, not paired, and their relative t_{half}, at least one order of magnitude greater.

Regarding the oscillatory and last mode, its relative high damping ratio ($\zeta \approx 0.73$) assess for its very damped performance. Besides, the fact that T and t_{half} adopt large values, while the number of cycles is very low, states for the similarity of the mode with a convergence one.

Mode	*Eigenvalue*	*Nat. Frequency,* $\omega_n \ [rad \cdot s^{-1}]$	*Period,* $T \ [s]$	*Time to half,* $t_{half} \ [s]$	*Cycles to half,* $N_{half} \ [cycles]$
λ_1	-105.19193	105.19193	–	0.00659	–
λ_2	-104.57603	104.57603	–	0.00663	–
λ_3	-54.089	54.089	–	0.01281	–
λ_4	-53.36604	53.36604	–	0.01299	–
λ_5	-0.78046	0.78046	–	0.88813	–
λ_6	-0.27489	0.27489	–	2.52154	–
$\lambda_{7,8}$	$-0.01838 \pm 0.01718i$	0.02516	249.73877	37.71203	0.10312

Table 3.10: Eigenvalues from lateral-directional dynamics.

The predicted two pairs of modes referred to the first four convergence ones, can be exhaustive evaluated in terms of their eigenvectors. Those are collected in Table 3.11. The first pair is given by the first two modes. Their eigenvectors state for a significant difference due to the order of magnitude of disturbances referring different kites. Then, in comparison, for the first mode, variables of the first kite adopt higher magnitudes than the same ones for the second mode, and viceversa. In this way, they act as similar modes, which although they act as coupled motions of variables from both kites, they separately affect, principally, one of the two kites respectively.

	$\boldsymbol{v}_1$		$\boldsymbol{v}_2$		$\boldsymbol{v}_3$		$\boldsymbol{v}_4$	
	Magn.	*Phase*	*Magn.*	*Phase*	*Magn.*	*Phase*	*Magn.*	*Phase*
φ_1	0.00873	0°	0.00461	0°	0.00894	180°	0.00799	0°
η_1	0.00347	0°	0.00183	0°	0.01194	180°	0.01333	0°
φ_2	0.00141	0°	0.0075	180°	0.00493	180°	0.00203	0°
η_2	0.00039	0°	0.00326	180°	0.00974	180°	0.01027	0°
$\dot{\varphi}_1$	0.91835	180°	0.48233	180°	0.48374	0°	0.4263	180°
$\dot{\eta}_1$	0.36456	180°	0.19162	180°	0.64577	0°	0.71115	180°
$\dot{\varphi}_2$	0.14813	180°	0.78393	0°	0.2667	0°	0.10857	180°
$\dot{\eta}_2$	0.04119	180°	0.34058	0°	0.5268	0°	0.54808	180°

Table 3.11: Lateral-directional eigenvectors (polar form).

In addition, making an individual evaluation for each mode, while the first one can be understood like a one with three degrees of freedom, being $\dot{\varphi}_1$ the dominant variable, and $\dot{\eta}_1$ and $\dot{\varphi}_2$ the other two relevant ones respectively, the second mode has mainly four degrees of freedom instead, being $\dot{\varphi}_2$ the dominant variable, and $\dot{\varphi}_1$, $\dot{\eta}_2$ and $\dot{\eta}_1$ the other three ones, written in descendent order of relevance. Trying to understood the physics, the second mode behaves as a motion in which the yaw component of the angular velocity of the second kite couples with the angular velocity magnitudes around $O_2^1 x_2^1$ and $O_1^1 z_1^1$ axes for the first and second kites respectively. Furthermore, regarding the first mode, it represents a rotary motion of the first kite around its $O_1^1 z_1^1$ axis at high angular velocity, which essentially couples with an also fast rotation in roll for the same kite.

The second pair is shaped by the third and fourth modes. These two are modes in which the first-order derivatives are the predominant variables. Concretely, while $\dot{\eta}_1$ and $\dot{\varphi}_2$ are the most and less

relevant ones respectively, $\dot{\varphi}_1$ and $\dot{\eta}_2$ occupy the second place in terms of relevance. Another also important feature of these modes is how the phase angles are decoupled, meaning that, while the third mode presents phase angles of 180° and 0° for angles and angular derivatives respectively, the opposite occurs for the fourth mode. Summarizing, modes 3 and 4 can be understood as motions in which the first kite rotates with a high rolling and yawing angular velocity components, motion which couples with the rapid rotation of the second kite around its $O_2^2 x_2^2$ axis.

	$\boldsymbol{v}_5$		$\boldsymbol{v}_6$		$\boldsymbol{v}_{7,8}$	
	Magnitude	*Phase*	*Magnitude*	*Phase*	*Magnitude*	*Phase*
φ_1	0.38166	0°	0.19397	0°	0.19239	198.71°
η_1	0.40348	180°	0.61479	0°	0.67694	180.48°
φ_2	0.06389	180°	0.67947	180°	0.19931	194.61°
η_2	0.5558	180°	0.22907	0°	0.68146	180°
$\dot{\varphi}_1$	0.29787	180°	0.05332	180°	0.00484	335.64°
$\dot{\eta}_1$	0.3149	0°	0.169	180°	0.01703	317.41°
$\dot{\varphi}_2$	0.04986	0°	0.18678	0°	0.00501	331.53°
$\dot{\eta}_2$	0.43378	0°	0.06297	180°	0.01715	316.92°

Table 3.12: Lateral-directional eigenvectors (polar form).

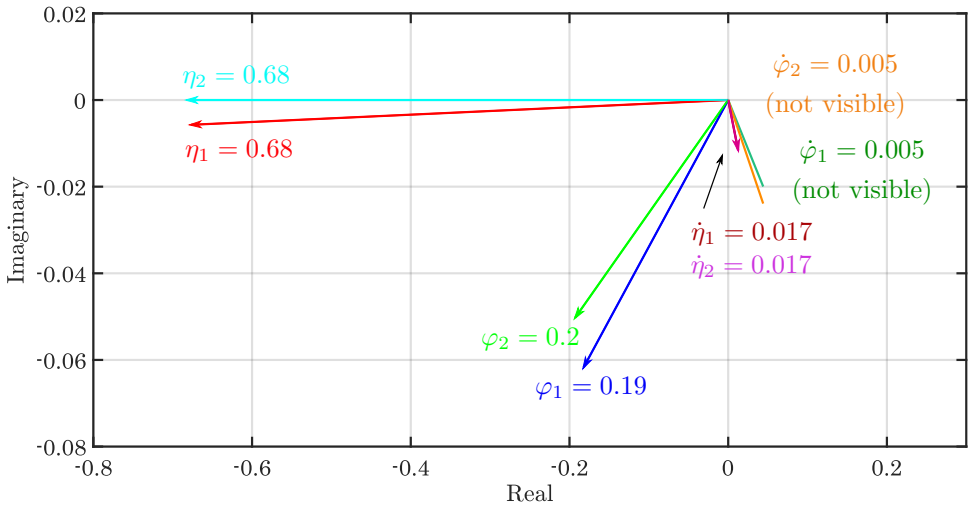

Figure 3.14: Vector diagram for $\boldsymbol{v}_{7,8}$.

The eigenvalues of the last two convergence modes are shown both in Table 3.12. Here the fifth mode accounts for a motion in which all the variables present some relevance with exception of φ_2 and its derivative. Although all the remaining variables present similar magnitudes, η_2 and $\dot{\eta}_1$ are the ones with more and less relevance respectively. Sixth mode presents also only two variables without relevance, being those $\dot{\varphi}_1$ and $\dot{\eta}_2$. Besides, while φ_1, η_2, $\dot{\eta}_1$, $\dot{\varphi}_2$ have comparable magnitude, η_1 and φ_2 are the two dominant variables of that mode.

Finally, the eigenvector of the oscillatory mode stated that this mode affects in the same way

both kites, being, the different state variables practically equal disturbed for these both. This fact can be easily appreciated at Fig. 3.15 where the only not appreciable variables due to their insignificant magnitudes, are the ones referred to the φ-derivatives, although the predominant state variables are the angular components.

Non-linear approach close to the equilibrium state

At the time of evaluating the modes by means of the non-linear approach, figures covered along this section are obtained. Here, as for the longitudinal motion analysis was done, variables for different kites are separated in different figures. Moreover, due to the difference in time spent to converge to the equilibrium state, three figures are required for plotting the different modes.

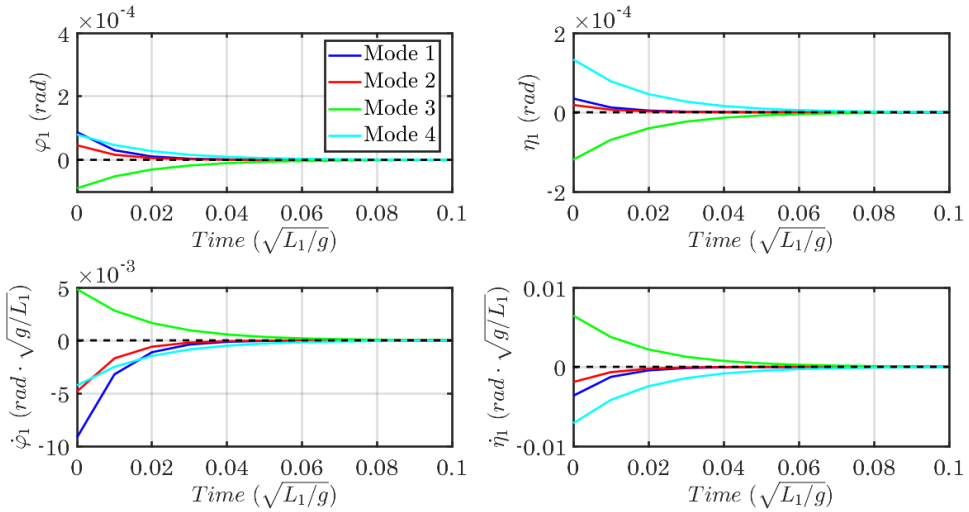

Figure 3.15: Transient disturbances of the lateral-directional state variables for the first kite.

In first place, figures 3.15 and 3.16 cover the disturbances of the state variables of the first and second kite respectively, for the paired modes shown in Table 3.11. Here the very fast convergence of the disturbances, predicted by values of t_{half} collected in Table 3.10, is shown, being all the variables stabilized for its equilibrium values for a very short period of time. In addition, the results act as it was forecasted, like paired modes. This fact is appreciated by looking at the two first modes (drawn with blue and red lines respectively), which, showing similar disturbance magnitudes, they have for the first kite the same phase angles, but different ones for the second kite, fact which was also assessed by data obtained during the linear analysis. However, an important feature is due to, although similar, the disturbances of the first mode are more relevant for the first kite, while the ones of the second mode, adopt more importance for the second kite. In parallel, the paired behavior of shuch as modes, principally is observed in these two for the second pair, composed by the third and fourth modes (represented with cyan and green lines respectively). These two present almost the same magnitudes for the different disturbances but opposite phase angles for all of them, fact which has to do with the vertical symmetry represented by their referred lines.

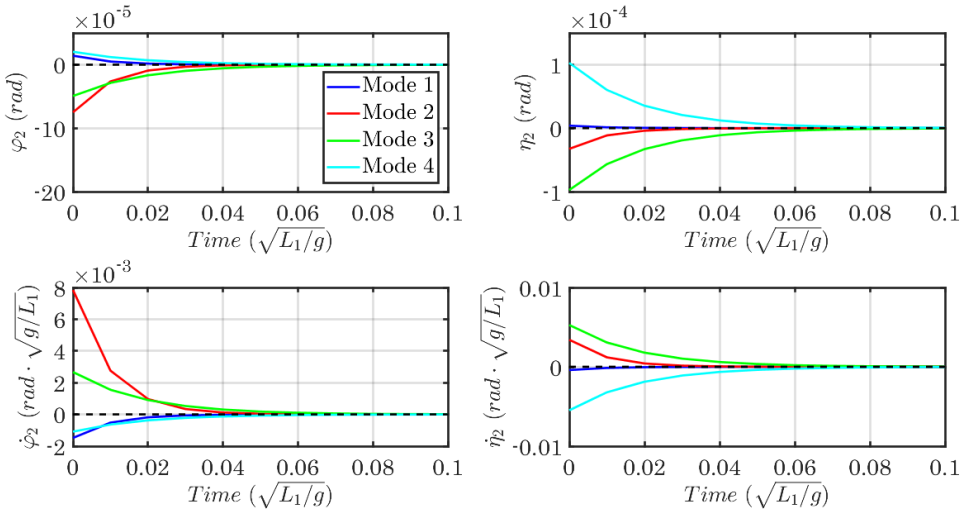

Figure 3.16: Transient disturbances of the lateral-directional state variables for the second kite.

Summarizing, the paired behaviour of shuch as modes, can be phisically understood as a combination of, two coupled similar modes affecting to a greater extent both kites respectively, where, while first mode presents more relevance in the motion of the first kite, the second mode does it for the second one and; two coupled modes presenting equal disturbance magnitudes for both kites, but perturbing their motion in opposite directions.

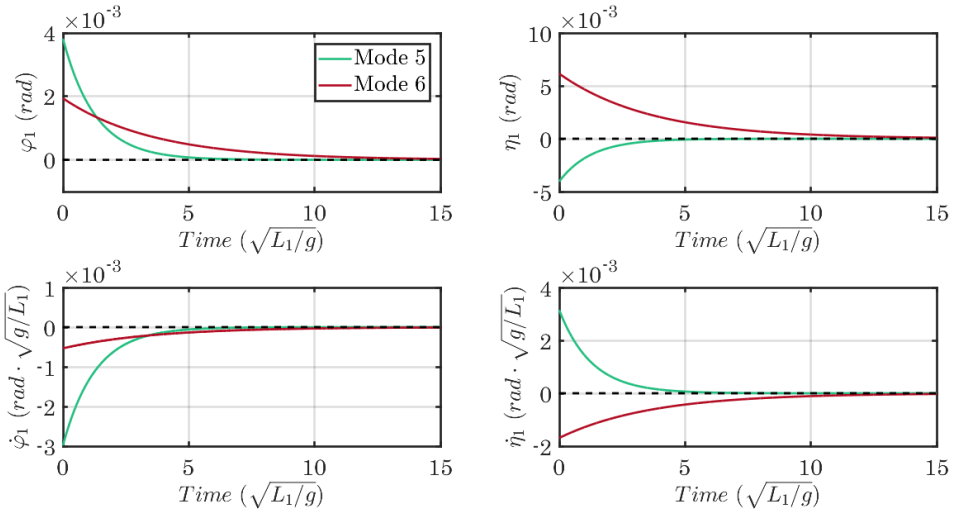

Figure 3.17: Transient disturbances of the lateral-directional state variables for the first kite.

Figures 3.17 and 3.18 show respectively the lateral variable disturbances regarding the other two remaining non-oscillatory modes, for the first and second kites. They assess for their higher convergence times in comparison with the previous analyzed subsidence modes, as forecasted by the linear approach. Both figures also represent how these two modes have the same disturbance

phase angles for yawing variables (angles and angular velocities), while opposite ones for rolling ones.

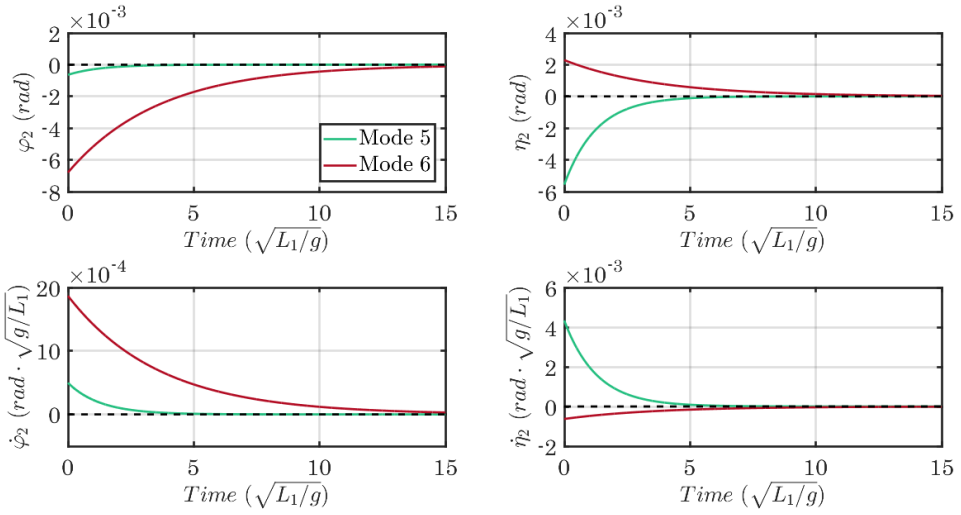

Figure 3.18: Transient disturbances of the lateral-directional state variables for the second kite.

Finally, the only one oscillatory mode is represented. Here, the results shown how the first order derivatives transients have very reduced-scale fast oscillations at the same time that they stabilize for their equilibrium values at macroscopic level. Moreover, the results show, the also predicted, highly damped behaviour of the variable transients.

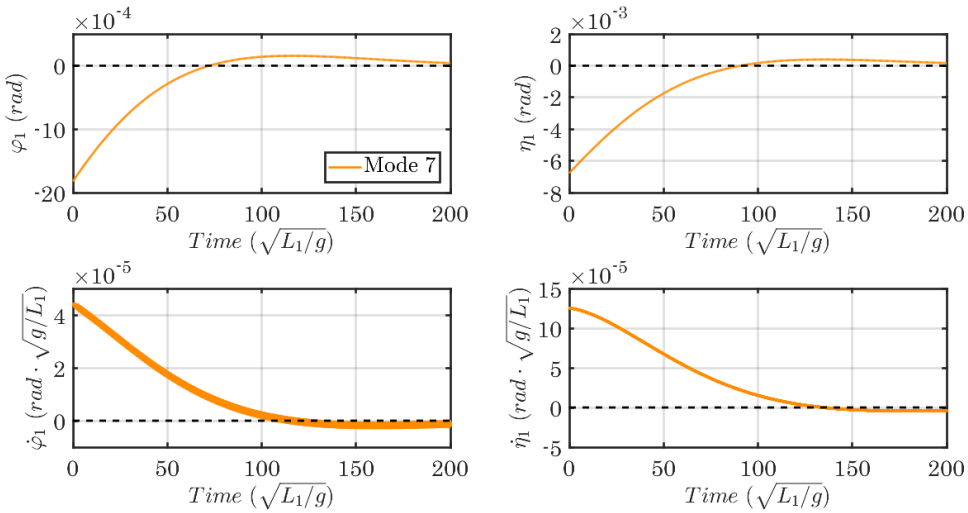

Figure 3.19: Transient disturbances of the lateral-directional state variables for the first kite.

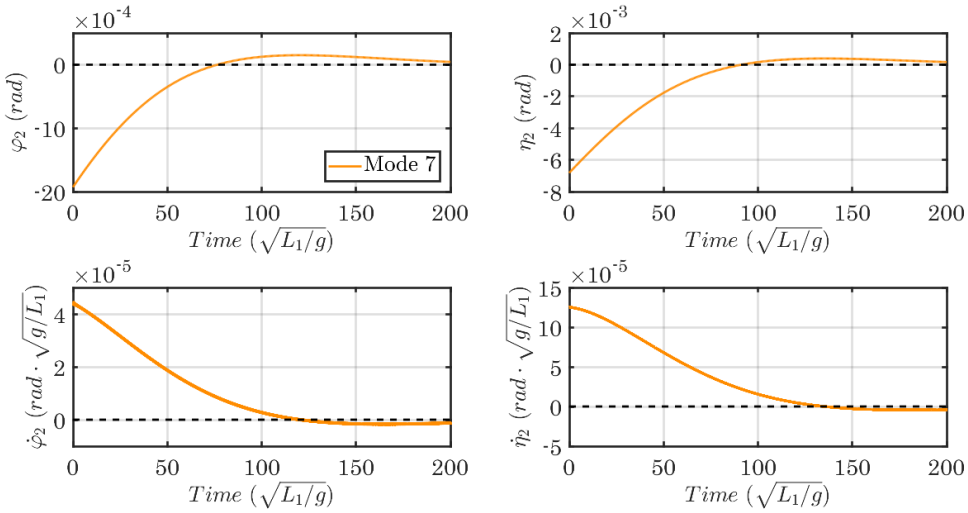

Figure 3.20: Transient disturbances of the lateral-directional state variables for the second kite.

3.6 Three-kites configuration

3.6.1 Equilibrium state

The equilibrium state achived for this onfiguration is given by the state vector,

$$\boldsymbol{x}_s^* = [0 \;\; 0.38736 \;\; 0 \;\; -0.13374 \;\; 0 \;\; 0.41141 \;\; 0 \;\; -0.09333 \;\; 0 \;\; 0.43839 \;\; 0 \;\; -0.03207] \quad (3.14)$$

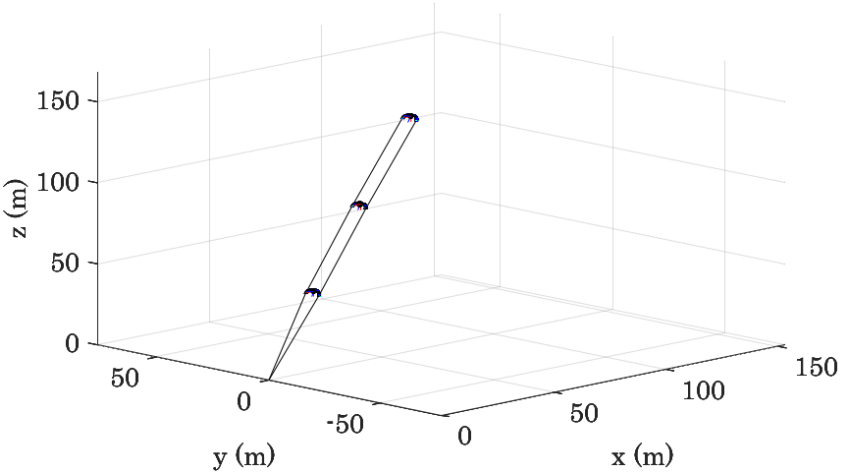

Figure 3.21: Sketch of the AWES three-kites configuration 3D equilibrium state.

Here, the respective summation of the longitudinal variables (in degrees) for each kite, leads to the following values of the angle of attack: $\alpha_1 = 14.5°$, $\alpha_2 = 18.2°$ and $\alpha_3 = 23.3°$. Those ones together with the symmetry aspect of the equilibrium state ($\beta = 0$), being the state variables

contained into the limitations of the model, assess for the correct physical equilibrium state. However, remembering that, due to the difficulties that arise, data in tables 3.1 and 3.2 was selected for achieving only stable equilibrium solutions for the configurations with one and two kites, the equilibrium solution is not any more stable, as it is explained in following sections. In Fig. 3.21, a 3D visualization of the kite equilibrium position is shown.

3.6.2 Longitudinal dynamics

Linear stability analysis close to the equilibrium state

Again, this section covers the longitudinal analysis of the system by solving the eigenvalues and eigenvectors problem obtained when linearizing the longitudinal equations of motion. In this case, the Jacobian of the whole system results to be a square matrix with twenty-four dimensions. Half of the total eigenvectors obtained when solving the problem are due to longitudinal modes. Those are collected in Table 3.13.

Mode	*Eigenvalue*	*Nat. Frequency,* $\omega_n \ [rad \cdot s^{-1}]$	*Period,* $T \ [s]$	*Time to half,* $t_{half} \ [s]$	*Cycles to half,* $N_{half} \ [cycles]$
$\lambda_{1,2}$	$-63.91835 \pm 11.73469i$	64.9866	0.53544	0.01084	0.02025
λ_3	-55.19223	55.19223	–	0.01256	–
$\lambda_{4,5}$	$-13.21619 \pm 11.81370i$	17.72657	0.53186	0.05245	0.09861
λ_6	-0.37924	0.37924	–	1.82773	–
$\lambda_{7,8}$	$-10.59361 \pm 5.02147i$	11.72347	1.25126	0.06543	0.05229
$\lambda_{9,10}$	$-4.61246 \pm 4.9406i$	6.75902	1.27174	0.15028	0.11817
λ_{11}	-2.6375	2.6375	–	0.2628	–
λ_{12}	-7.65221	7.65221	–	0.09058	–

Table 3.13: Eigenvalues from longitudinal dynamics.

Here, four oscillatory modes are found, together with another four non-oscillatory ones, all of them assessing for the longitudinal stability of the system ($n < 0, \ \forall \ \lambda$). A priori, looking for the similiraties with previous results, one can indicate that all these eigenmodes seem to behave in similar ways to the eigenmodes found for the systems with one and two kites respectively. Concretely, making an exhaustive comparative analysis between the eigenvalues obtained for the different systems, one can find certain parallelism in the results. All of them converge for short periods of time, adopting small values for t_{half} and N_{half}. Furthermore, regarding the oscillatory modes, those are presented as very damped oscillations. Anyway, the eigenvectors directly show certain relation with the ones obtained in previous sections. This type of relationships could be extrapolated to the different modes apperaring here. This fact, however, should be evaluated by analyzing also their relative eigenvectors (tables 3.14 and 3.15).

The related eigenvectors state also for the forecasted relationships. The first and second modes seems to behave like ones with three degrees of freedom, being those ones, the three θ-derivative variables relative for each kite, and concretely, the dominant one, $\dot{\theta}_3$. The third mode, being oscillatory, behaves in a similar way, but in this case, being $\dot{\theta}_2$ the dominant state variable instead.

The fourth mode is shown a little more complicated, being a mode in which the angular variables adopt, in general terms, higher disturbance values than their derivatives. An exception of this feature, is the case of θ_3, which together with $\dot{\theta}_2$ and $\dot{\theta}_3$, is the less relevant variable. Contrarily, γ-variables, as well as, θ_1 and θ_2 present dominant behaviours, leading to the consequent importance of their derivatives.

	$\boldsymbol{v}_{1,2}$		$\boldsymbol{v}_3$		$\boldsymbol{v}_{4,5}$		$\boldsymbol{v}_6$	
	Magn.	*Phase*	*Magn.*	*Phase*	*Magn.*	*Phase*	*Magn.*	*Phase*
γ_1	0.00021	278.07°	0.00033	0°	0.00126	103.79°	0.37192	0°
θ_1	0.00557	98.28°	0.00865	180°	0.03235	293.74°	0.44932	180°
γ_2	0.0003	326.02°	0.00028	180°	0.00129	8.92°	0.44681	0°
θ_2	0.00817	145.93°	0.00743	0°	0.03662	221.79°	0.21157	180°
γ_3	0.00042	8.87°	0.00048	0°	0.00062	299.92°	0.535577	0°
θ_3	0.01178	190.40°	0.01406	180°	0.02794	163.67°	0.05298	0°
$\dot{\gamma}_1$	0.01383	87.67°	0.01796	180°	0.02226	242°	0.14105	180°
$\dot{\theta}_1$	0.36172	267.88°	0.47767	0°	0.57352	71.95°	0.1704	0°
$\dot{\gamma}_2$	0.01967	135.61°	0.01556	0°	0.02288	147.13°	0.16945	180°
$\dot{\theta}_2$	0.53104	315.53°	0.41023	180°	0.64912	0°	0.08023	0°
$\dot{\gamma}_3$	0.02753	178.46°	0.02657	180°	0.01101	78.13°	0.20311	180°
$\dot{\theta}_3$	0.76524	0°	0.77585	0°	0.49539	301.87°	0.02009	180°

Table 3.14: Longitudinal eigenvectors (polar form).

The fifth and eighth modes, although being oscillatory and non-oscillatory modes respectively, are in some way paired. Both are presented as modes with three degrees of freedom, in which the predominant variables are $\dot{\theta}_1$ and $\dot{\theta}_2$, being the last of them, but with less significant relevance, $\dot{\theta}_3$. Meanwhile, the magnitude of the rest of derivatives and angular variables are at least one order of magnitude smaller.

	$\boldsymbol{v}_{7,8}$		$\boldsymbol{v}_{9,10}$		$\boldsymbol{v}_{11}$		$\boldsymbol{v}_{12}$	
	Magn.	*Phase*	*Magn.*	*Phase*	*Magn.*	*Phase*	*Magn.*	*Phase*
γ_1	0.00174	4.09°	0.0078	322.55°	0.02829	0°	0.00329	0°
θ_1	0.06576	205.36°	0.14041	226.97°	0.06622	0°	0.09652	180°
γ_2	0.00136	145.75°	0.00705	114.98°	0.01991	0°	0.00441	0°
θ_2	0.0489	61.63°	0.03814	146.12°	0.33484	0°	0.08439	0°
γ_3	0.00285	276.68°	0.00406	5.48°	0.0891	180°	0.00545	180°
θ_3	0.02226	170.3°	0.01119	232.24°	0.00663	180°	0.01711	0°
$\dot{\gamma}_1$	0.0204	158.73°	0.05275	95.58°	0.0746	180°	0.0252	180°
$\dot{\theta}_1$	0.7709	0°	0.949	0°	0.17466	180°	0.73862	0°
$\dot{\gamma}_2$	0.0159	300.39°	0.04762	248.02°	0.05252	180°	0.03377	180°
$\dot{\theta}_2$	0.57326	216.27°	0.25776	279.16°	0.88315	180°	0.64575	180°
$\dot{\gamma}_3$	0.03346	71.32°	0.02745	138.52°	0.23501	0°	0.04174	0°
$\dot{\theta}_3$	0.26092	324.94°	0.07566	5.28°	0.01748	0°	0.13091	180°

Table 3.15: Longitudinal eigenvectors (polar form).

Finally, the sixth and seventh modes result to behave like ones with only one dominant variable, $\dot{\theta}_1$ and $\dot{\theta}_2$ respectively. Furthermore, in these modes, some other disturbance quantities reveal some importance, as occurs with $\dot{\theta}_2$ for the sixth mode, and θ_2 and $\dot{\gamma}_3$ for the seventh one. Fig. 3.22 covers the graphical polar representation of the sixth mode.

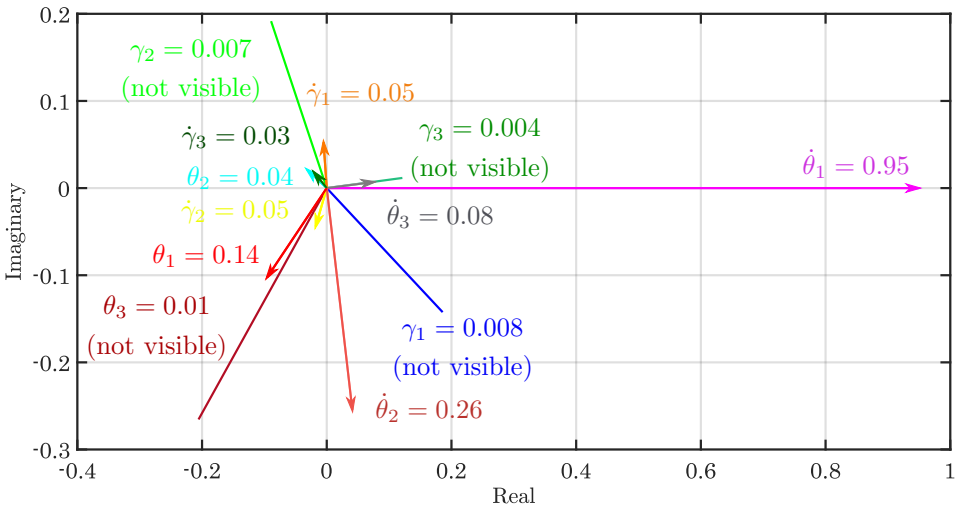

Figure 3.22: Vector diagram for $\boldsymbol{v}_{9,10}$.

Non-linear stability analysis close to the equilibrium state

In this section, where the results of the direct integration of the longitudinal equations of motion are collected only for the sixth mode, the variables describing the motion are covered separately in three figures, referred each one to each kite involved. The results shown are consequent with the ones obtained during the linear approach.

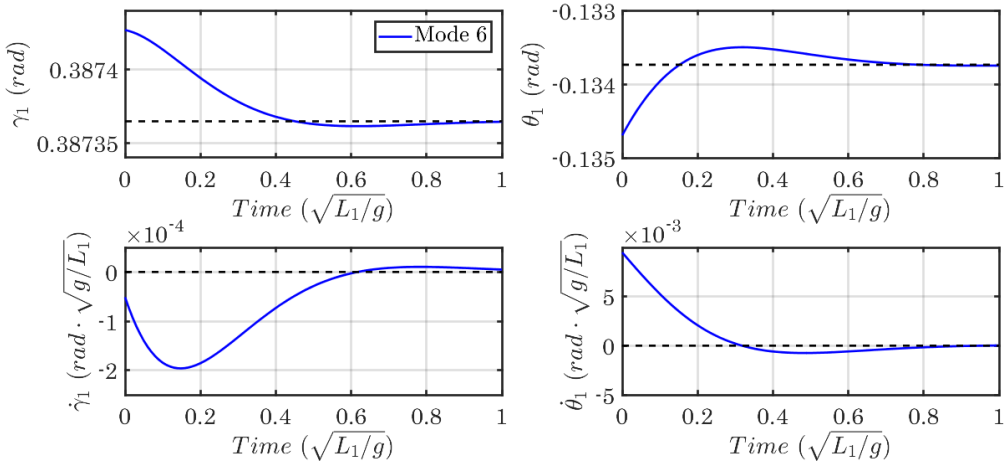

Figure 3.23: Transient disturbances of the longitudinal state variables for the first kite.

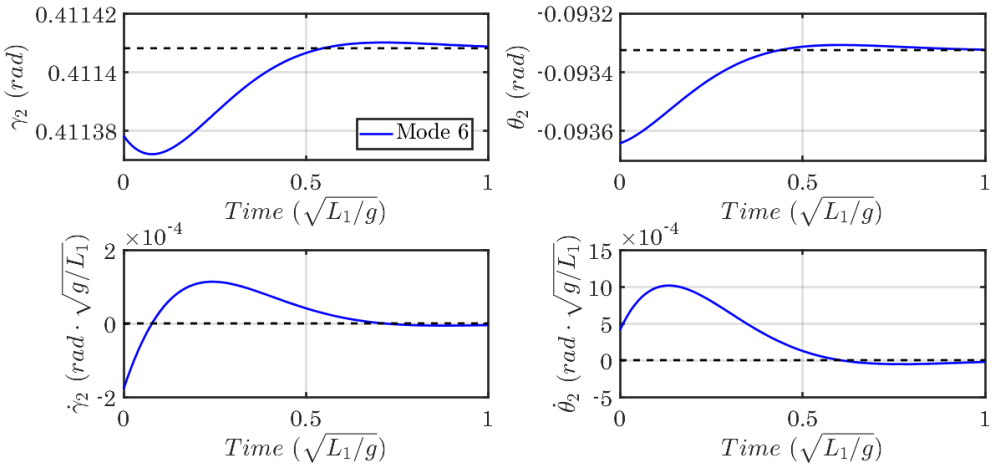

Figure 3.24: Transient disturbances of the longitudinal state variables for the second kite.

The disturbance quatities referred to this mode present a very fast convergence behaviour, as it was predicted by the linear analysis. It is also an interesting matter, how the different longitudinal variables are more or less damped depending on the kite involved. Anyway, the mode results to present a 'lighly' damped performace in comparison with the rest of modes appearing until now, having a damping ratio given by the linear approximation, of almost $\zeta \simeq 0.68$.

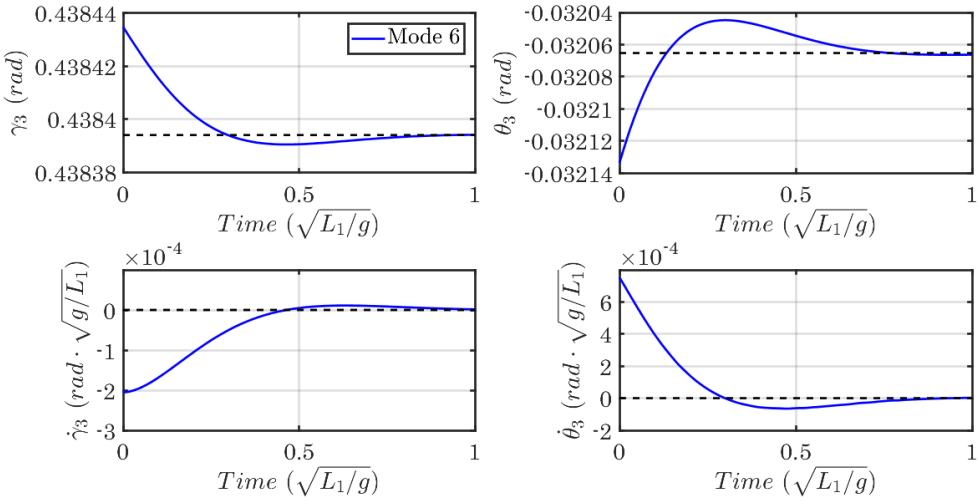

Figure 3.25: Transient disturbances of the longitudinal state variables for the third kite.

Due to the homogeneity in the results achieved by solving both, linear and non-linear problems for previous configurations, to avoid redundancy in the explanations, and since analyses state that so many of the modes collected above behave like modes previously described, it has been decided to further evaluate only the sixth longitudinal mode along these two last sections.

3.6.3 Lateral-directional dynamics

Linear stability analysis close to the equilibrium state

The lateral-directional dynamic analysis of the system equations of motion, provides now the eigenvalues shown in Table 3.16. Here, while only one mode is oscillatory, eleven modes are non-oscillatory. As it was introduced, the dimensional parameters of the kites, as well as the non-dimensional coefficients selected for the construction of the simulation, result as a good approach to assess the stability of the equilibrium position for both configuration with one and two kites. However, although longitudinal stability is also achieved for the current case of three kites, lateral instability takes place. That issue is given by the nineth mode appearing here, since, being a non-oscillary mode, its eigenvalue present only positive real part ($n > 0$, for λ_{10}). It should be noticed here the fact that for the unstable mode, the value of t_{half} in Table 3.16, being equally obtained by means of the same expression developed in Eq. 3.7, is instead known as time to double.

Mode	*Eigenvalue*	*Nat. Frequency*, $\omega_n \ [rad \cdot s^{-1}]$	*Period*, $T \ [s]$	*Time to half*, $t_{half} \ [s]$	*Cycles to half*, $N_{half} \ [cycles]$
λ_1	-105.95261	105.95261	–	0.00654	–
λ_2	-104.861	104.861	–	0.00661	–
λ_3	-104.50897	104.50897	–	0.00663	–
λ_4	-54.22995	54.22995	–	0.01278	–
$\lambda_{5,6}$	$-54.25194 \pm 0.4639i$	54.25392	13.54	0.01278	0.00094
λ_7	-1.11507	1.11507	–	0.62162	–
λ_8	-0.85694	0.85694	–	0.80886	–
λ_9	-0.43217	0.43217	–	1.60388	–
λ_{10}	0.04023	0.04023	–	17.22961	–
λ_{11}	-0.02299	0.02299	–	30.14994	–
λ_{12}	-0.17699	0.17699	–	3.91631	–

Table 3.16: Eigenvalues from lateral-directional dynamics.

Looking at the eigenvalues, again similiraties with previous configurations take place. As it occurs during the longitudinal analysis, one can indicate that some of the modes appearing behave in similar ways to the eigenmodes found for the systems of two and one kites respectively. With the exception of the nineth and tenth modes (those referred to λ_9 and λ_{10}), all the rest of them converge fastly, adopting small values for t_{half}. Moreover the oscillatory mode also accounts with short value of N_{half}, resulting again to behave as a critically damped solution, being its damping ratio close to the unity. Anyway, as occurred in previous sections, the lateral-directional eigenvectors show certain relation with the ones obtained for previous configurations. This fact, however, should be exahustive evaluated by analyzing also the related eigenvectors (tables 3.17, 3.18 and 3.19).

Just looking at the eigenvectors, in first place, the first three modes seem to show similar behaviours, being modes for which the angular variables do not acquire important effects, and for

which their most relevant variables are due to the yawing angular velocites. The first of these modes presents as predominant variable, the yawing angular velocity of the first kite which couples with the rolling component one of this same kite. On contrary, for the second and third modes, adopting all the first derivative parameters some relevance, the dominant variables are essentially the yawing angular velocity, but in this case for the second kite.

	$\boldsymbol{v}_1$		$\boldsymbol{v}_2$		$\boldsymbol{v}_3$		$\boldsymbol{v}_4$	
	Magn.	*Phase*	*Magn.*	*Phase*	*Magn.*	*Phase*	*Magn.*	*Phase*
φ_1	0.00872	180°	0.00299	0°	0.00139	180°	0.01321	180°
η_1	0.0033	180°	0.00113	0°	0.00053	180°	0.01067	180°
φ_2	0.00131	180°	0.00761	180°	0.00713	0°	0.00393	0°
η_2	0.00039	180°	0.00305	180°	0.00283	0°	0.00357	180°
φ_3	0.00035	0°	0.00344	180°	0.00503	180°	0.00121	0°
η_3	0.00031	0°	0.0013	180°	0.00228	180°	0.00467	180°
$\dot{\varphi}_1$	0.92404	0°	0.31308	180°	0.14578	0°	0.71656	0°
$\dot{\eta}_1$	0.35011	0°	0.11873	180°	0.0552	0°	0.57889	0°
$\dot{\varphi}_2$	0.13911	0°	0.79829	0°	0.74503	180°	0.21294	180°
$\dot{\eta}_2$	0.04093	0°	0.3195	0°	0.2961	180°	0.19338	0°
$\dot{\varphi}_3$	0.03716	180°	0.36054	0°	0.52567	0°	0.06587	180°
$\dot{\eta}_3$	0.03275	180°	0.13585	0°	0.23778	0°	0.253	0°

Table 3.17: Lateral-directional eigenvectors (polar form).

	$\boldsymbol{v}_{5,6}$		$\boldsymbol{v}_7$		$\boldsymbol{v}_8$		$\boldsymbol{v}_9$	
	Magn.	*Phase*	*Magn.*	*Phase*	*Magn.*	*Phase*	*Magn.*	*Phase*
φ_1	0.01318	180.49°	0.24344	180°	0.07824	0°	0.60676	180°
η_1	0.01065	182.52°	0.31877	0°	0.36461	180°	0.20078	0°
φ_2	0.00279	330.03°	0.13989	180°	0.46046	0°	0.16347	0°
η_2	0.00428	193.32°	0.3339	0°	0.19347	180°	0.50554	0°
φ_3	0.00052	270.91°	0.00861	0°	0.1051	180°	0.278	180°
η_3	0.00512	186.32°	0.39211	0°	0.42074	180°	0.27307	0°
$\dot{\varphi}_1$	0.71496	0°	0.27145	0°	0.06704	180°	0.26223	0°
$\dot{\eta}_1$	0.57771	2.03°	0.35548	180°	0.31245	0°	0.08677	180°
$\dot{\varphi}_2$	0.15598	149.54°	0.15598	0°	0.39459	180°	0.07065	180°
$\dot{\eta}_2$	0.23198	12.83°	0.37232	180°	0.16579	0°	0.21848	180°
$\dot{\varphi}_3$	0.02803	90.42°	0.0096	180°	0.09006	0°	0.12014	0°
$\dot{\eta}_3$	0.27795	5.83°	0.43723	180°	0.36055	0°	0.11802	180°

Table 3.18: Lateral-directional eigenvectors (polar form).

The fourth and fifth modes behave in very similar ways between them, both having as predominant variables the rolling and yawing angular velocity components of the first kite. Moreover, in this coupled motion, with exception of the $\dot{\varphi}_3$, the rest of agular velocity state vector components present some relevance. The sixth and seventh modes behave like ones in which practically all

the variables are uniform in terms of their order of magnitude. Furthermore these modes seem to be decoupled between them in terms of phase angles. While the different variables for one of these two modes, adopt a determined phase angle values, the opposite values are adopted by the other mode. Similar to what happens with these two modes in terms of magnitude of the state variables, almost the same occurs for the eighth mode. This mode, however, shows certain coupled performance between the yawing and rolling angles of the first and second kites respectively.

	$\boldsymbol{v}_{10}$		$\boldsymbol{v}_{11}$		$\boldsymbol{v}_{12}$	
	Magn.	*Phase*	*Magn.*	*Phase*	*Magn.*	*Phase*
φ_1	0.28811	0°	0.12013	0°	0.00271	0°
η_1	0.51636	0°	0.56783	0°	0.47549	0°
φ_2	0.29276	0°	0.11209	0°	0.11	180°
η_2	0.51661	0°	0.56499	0°	0.42802	0°
φ_3	0.23694	0°	0.10958	0°	0.72369	180°
η_3	0.48992	0°	0.56464	0°	0.1565	0°
$\dot{\varphi}_1$	0.01159	0°	0.00276	180°	0.00048	180°
$\dot{\eta}_1$	0.02077	0°	0.01305	180°	0.08416	180°
$\dot{\varphi}_2$	0.00258	0°	0.00258	180°	0.01947	0°
$\dot{\eta}_2$	0.02078	0°	0.01299	180°	0.07576	180°
$\dot{\varphi}_3$	0.00953	0°	0.00252	180°	0.12809	0°
$\dot{\eta}_3$	0.01971	0°	0.01298	180°	0.0277	180°

Table 3.19: Lateral-directional eigenvectors (polar form).

The nineth mode accounts for the instability of the system. However, this mode present some similarities with the tenth one, being for both modes, the angular variables the dominant ones, while their first derivatives significantly smaller in terms of order of magnitude. These modes can be physically understood as a very fast coupled motion in rolling for each kite, which leads to the apparison of smaller perturbations in the yawing component of the angular velocity. To conclude, the eleventh and last mode shows mainly three degrees of freedom affecting the motion, which has to do with φ_3 and η-variables for the first and second kites. Between these three, being φ_3 the dominant variable, their magnitude values assess for the phisycs of the system, stating that the yawing motion of the third kite leads to generate an induced rotation in roll for the two previous kites.

Non-linear stability analysis close to the equilibrium state

The results of the direct integration of the lateral equations of motion are collected in this section. As it was done for the longitudinal analysis, here the variables describing the motion are covered separately in three figures, referred each one to each kite involved. Furthermore, only the eighth and nineth lateral modes are studied, since it is found that the rest of the appearing modes behave in similar ways than those ones previously analyzed for configurations with one and two kites. In this way, and, in order to avoid redundancy in the explanations, it results more usefull to cover only the integration of the equations of motion when perturbed in the direction of these two modes

since, while the eighth mode apparently seems different from previous analized modes, the nineth one assess for the lateral instability aspect of the system.

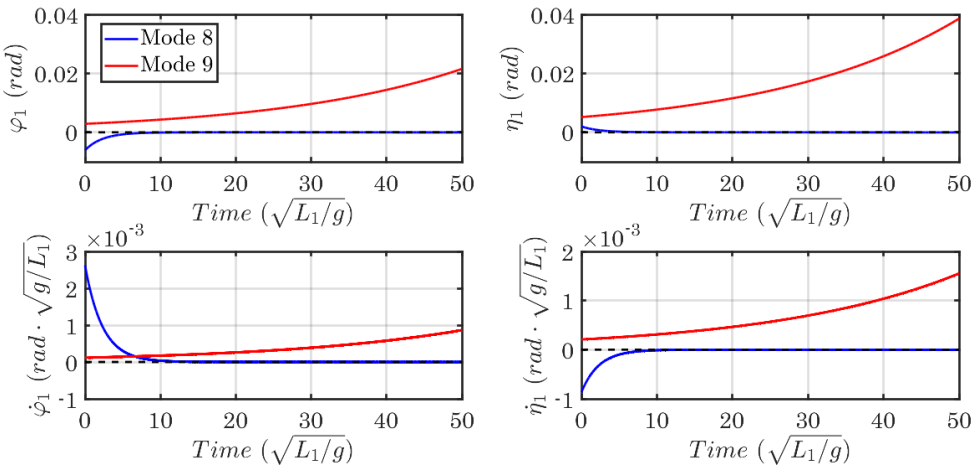

Figure 3.26: Transient disturbances of the lateral-directional state variables for the first kite.

Figures 3.26, 3.27 and 3.28 show the disturbances of the lateral variables for each of the kites respectively. Once more time, the results from the direct integration of the equations, are shown consequent with the linear approach ones. The very fast convergent and divergent nature predicted for both respective modes shown here, stated what the integration of the equations of motion now represent in these graphs.

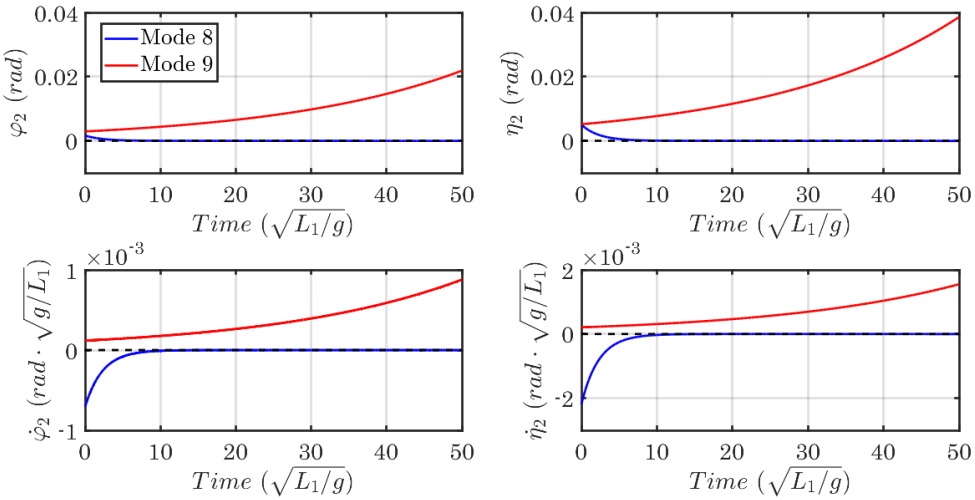

Figure 3.27: Transient disturbances of the lateral-directional state variables for the second kite.

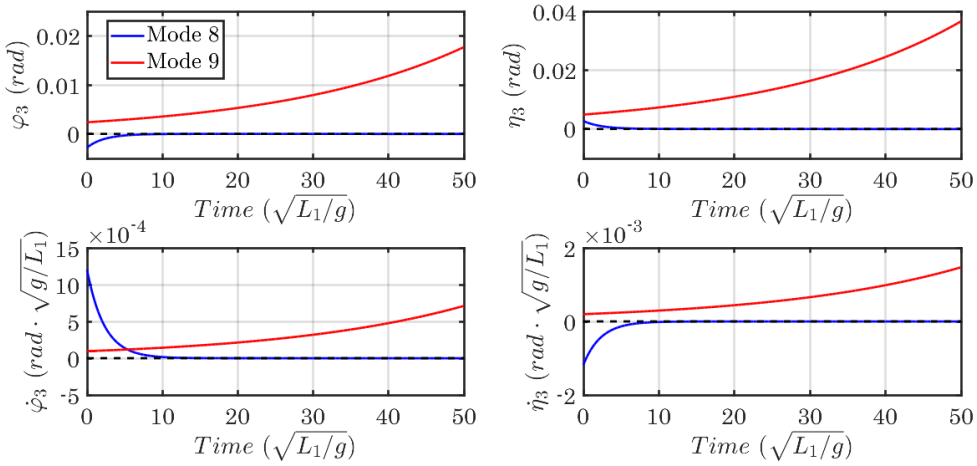

Figure 3.28: Transient disturbances of the lateral-directional state variables for the third kite.

3.7 Four-kites configuration

Analyzing results for the configuration with three kites, one could extract that modes appearing are constructed around the ones obtained for the first configuration with only one kite. In order to further evaluate this assumption, and to complete this work with robust conclusions, the cofiguration including four kites is proposed.

3.7.1 Equilibrium state

Longitudinal variables get for the equilibrium state are similar to those ones get for the configurations previously analized.

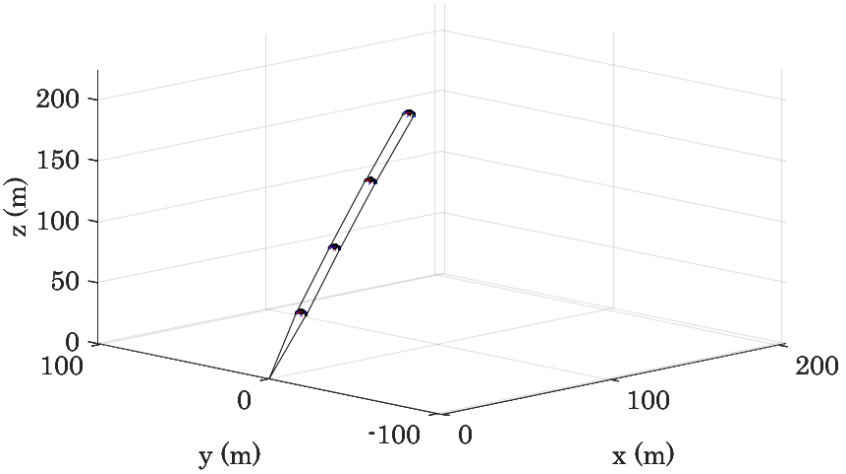

Figure 3.29: Sketch of the AWES four-kites configuration 3D equilibrium state.

The attack angles are, respectively, for each kite: $\alpha_1 = 11.83°$, $\alpha_2 = 14.53°$, $\alpha_3 = 18.22°$ and $\alpha_4 = 23.28°$. Being inside the limitations of the model, these obtained values assess for the correct equilibrium state. In addition, a relation between the values can be easily appreciated, noticing that the angle of attack is higher as the kite is placed in a higher position of the train.

3.7.2 Longitudinal dynamics

Linear stability analysis close to the equilibrium state

Solving the eigenvalues and eigenvectors problem defined by means of the Taylor expansion deployed from the equations of motion in the longitudinal direction, the ten eigenvalues collected in Table 3.20 are obtained. A simple inspection of the solutions, denote the existence of six oscillatory and four non-oscillatory modes, resulting all of them to be stable.

Mode	*Eigenvalue*	*Nat. Frequency,* $\omega_n \ [rad \cdot s^{-1}]$	*Period,* $T \ [s]$	*Time to half,* $t_{half} \ [s]$	*Cycles to half,* $N_{half} \ [cycles]$
$\lambda_{1,2}$	$-67.36891 \pm 13.52174i$	68.7125	0.46467	0.01029	0.02214
$\lambda_{3,4}$	$-56.12477 \pm 3.80806i$	56.25381	1.64997	0.01235	0.00749
$\lambda_{5,6}$	$-12.83483 \pm 12.41664i$	17.85793	0.48954	0.05582	0.10672
λ_7	-12.36091	12.36091	–	0.05608	–
$\lambda_{8,9}$	$-11.75115 \pm 5.55851i$	12.99948	0.05899	0.06543	0.05218
λ_{10}	-0.28677	0.28677	–	2.41708	–
λ_{11}	-2.1357	2.1357	–	0.32455	–
$\lambda_{12,13}$	$-4.34225 \pm 5.57364i$	7.06545	1.1273	0.15963	0.1416
$\lambda_{14,15}$	$-3.2951 \pm 4.88752i$	5.89453	1.28556	0.21036	0.16363
λ_{16}	-7.94075	7.94075	–	0.08729	–

Table 3.20: Eigenvalues from longitudinal dynamics.

The modes seem to behave similarly to those ones previously analized. In general, similarities in terms of natural frequency are found, which should be further investigated by evaluating their relative eigenvectors. In the same manner, the oscillatory modes are shown as very damped solutions, having daping ratio near to one. Their periods also behave similarly to modes appearing for simplier configurations. Time to half and cycles to half also present small values assessing for the very fast convergence nature of all the obtained modes.

Tables 3.21, 3.22 and 3.23 collect the eigenvectors referred respectively to each of the eigenvalues obtained. The first three modes, being oscillatory ones, behave in very similar ways. These three, are modes in which the four θ-derivatives are the predominant state variables. While for the first two modes, between these four variables, the dominant one is the angular velocity referred to the last kite, for the third eigenmode, it results to be the one referred to the third kite. Parallely, the fourth and fiveth modes perform in almost similar ways, but in this case presenting only three main degrees of freedom due to the θ-derivatives of the first three kites. Eighth, nineth and tenth modes (related to $\boldsymbol{v}_{12,13}$ and $\boldsymbol{v}_{14,15}$ respectively) are also modes for which the most relevant

variables are some of the θ-derivatives. Being $\dot{\theta}_1$ and $\dot{\theta}_2$ the two main degrees of freedom of the eighth and nineth modes, $\dot{\theta}_2$ and $\dot{\theta}_3$ are the ones for the last mode.

	$\boldsymbol{v}_{1,2}$		$\boldsymbol{v}_{3,4}$		$\boldsymbol{v}_{5,6}$		$\boldsymbol{v}_{7}$	
	Magn.	*Phase*	*Magn.*	*Phase*	*Magn.*	*Phase*	*Magn.*	*Phase*
γ_1	0.00015	87.65°	0.00027	148.37°	0.00086	158.29°	0.00143	180°
θ_1	0.00389	267.2°	0.00687	327.99°	0.02011	329.38°	0.03782	0°
γ_2	0.00021	125.55°	0.00026	269.84°	0.00126	77.66°	0.00187	0°
θ_2	0.0056	304.6°	0.00668	86.23°	0.02991	276.67°	0.06436	180°
γ_3	0.00027	158.68°	0.00028	54.82°	0.00119	17.29°	0.00052	0°
θ_3	0.00756	338.82°	0.00723	234.35°	0.03299	224.05°	0.03038	0°
γ_4	0.00037	189.8°	0.00045	182.53°	0.00069	314.01°	0.00114	180°
θ_4	0.01039	11.35°	0.01309	3.88°	0.0271	173.43°	0.00046	180°
$\dot{\gamma}_1$	0.01048	256.3°	0.01508	324.49°	0.01544	294.24°	0.01769	0°
$\dot{\theta}_1$	0.26717	75.85°	0.38645	144.11°	0.35904	105.33°	0.46744	180°
$\dot{\gamma}_2$	0.01437	294.2°	0.01477	85.96°	0.02253	213.61°	0.02314	180°
$\dot{\theta}_2$	0.38465	113.25°	0.3756	262.35°	0.53416	52.62°	0.79553	0°
$\dot{\gamma}_3$	0.01886	327.33°	0.01506	230.94°	0.02117	153.24°	0.00638	180°
$\dot{\theta}_3$	0.51916	147.48°	0.40688	50.47°	0.58909	0°	0.37551	180°
$\dot{\gamma}_4$	0.02537	358.45°	0.0251	358.65°	0.01225	89.95∘	0.01408	0°
$\dot{\theta}_4$	0.71387	180°	0.73648	180°	0.48401	309.38°	0.0057	0°

Table 3.21: Longitudinal eigenvectors (polar form).

	$\boldsymbol{v}_{8,9}$		$\boldsymbol{v}_{10}$		$\boldsymbol{v}_{11}$		$\boldsymbol{v}_{12,13}$	
	Magn.	*Phase*	*Magn.*	*Phase*	*Magn.*	*Phase*	*Magn.*	*Phase*
γ_1	0.00149	143.56°	0.33275	0°	0.03139	180°	0.00294	273.76°
θ_1	0.03406	327.98°	0.46312	180°	0.00809	0°	0.0886	160.57°
γ_2	0.00193	0.16°	0.36386	0°	0.0246	180°	0.00448	121.86°
θ_2	0.05888	205.32°	0.30438	180°	0.19538	180°	0.10621	52.08°
γ_3	0.00062	148.84°	0.39395	0°	0.00185	180°	0.00558	303.05°
θ_3	0.03258	70.28°	0.12132	180°	0.35539	180°	0.01991	324.13°
γ_4	0.00151	301.36°	0.44914	0°	0.1167	0°	0.00241	200.18°
θ_4	0.01364	220.96°	0.04613	0°	0.00765	0°	0.00669	102.26°
$\dot{\gamma}_1$	0.0194	298.24°	0.09542	180°	0.06705	0°	0.02078	41.68°
$\dot{\theta}_1$	0.44273	122.67°	0.13281	0°	0.01729	180°	0.62603	288.49°
$\dot{\gamma}_2$	0.02514	154.85°	0.10436	180°	0.05255	0°	0.03163	249.78°
$\dot{\theta}_2$	0.76538	0°	0.08729	0°	0.41728	0°	0.75042	180°
$\dot{\gamma}_3$	0.008	303.52°	0.11298	180°	0.00395	0°	0.03943	70.97°
$\dot{\theta}_3$	0.42356	224.97°	0.03479	0°	0.75901	0°	0.14069	180°
$\dot{\gamma}_4$	0.01957	96.04°	0.1288	180°	0.24924	180°	0.01706	328.1°
$\dot{\theta}_4$	0.17732	15.64°	0.01323	180°	0.01633	180°	0.0473	230.19°

Table 3.22: Longitudinal eigenvectors (polar form).

Sixth mode is presented as a mode in which the angular variables present in general terms, higher order of magnitude than their derivatives. For this mode, θ-variables loose relevance as higher is the relative position of the kites in the train, while γ-variables head in the opposite direction. In this way the most relevant variables here are θ_1 and γ_4. Regarding the remaining seventh mode, it results to behave like one in which the dominant variables are mainly the agular velocities $\dot{\theta}_2$ and $\dot{\theta}_3$, although its related angles, as well as γ_4 and its derivative, also accounts with some important relevance.

	$\boldsymbol{v}_{14,15}$		$\boldsymbol{v}_{16}$	
	Magnitude	*Phase*	*Magnitude*	*Phase*
γ_1	0.00599	212.67°	0.00137	0°
θ_1	0.11222	125.96°	0.00005	0°
γ_2	0.00297	89.66°	0.0022	0°
θ_2	0.12019	56.01°	0.08739	180°
γ_3	0.00759	310.17°	0.00345	0°
θ_3	0.02752	338.04°	0.08729	0°
γ_4	0.00383	211.66°	0.00528	180°
θ_4	0.0078	96.28°	0.01756	0°
$\dot{\gamma}_1$	0.0353	336.66°	0.01091	180°
$\dot{\theta}_1$	0.6615	249.95°	0.00036	180°
$\dot{\gamma}_2$	0.01751	213.65°	0.01751	180°
$\dot{\theta}_2$	0.70848	180°	0.69391	0°
$\dot{\gamma}_3$	0.04476	74.16°	0.02739	180°
$\dot{\theta}_3$	0.16224	102.03°	0.69317	180°
$\dot{\gamma}_4$	0.02258	335.65°	0.04194	0°
$\dot{\theta}_4$	0.04598	220.27°	0.13946	180°

Table 3.23: Longitudinal eigenvectors (polar form).

As forecastings predicted, studying the eigenvectors obtained, one can assess for the important existing similarities beween the modes with the ones obtained for previous configurations. In this way, due to these similarities and to avoid redundancy, it is decided not to obtain the results by means of the non-linear approach.

3.7.3 Lateral-directional dynamics

Linear stability analysis close to the equilibrium state

The twelve lateral-directional eigenvalues obtained are the ones collected in Table 3.24. Five of them are oscillatory while the other eight remaining ones, non-oscillatory modes. As for the three kites train, one mode becomes instable, thus leading to the global system lateral instability. Oscillatory modes present relative large periods, and very short values for t_{half} and N_{half}. This fact assess for the very rapid convergence of this modes, which essentially perform as critically damped solutions. On the other hand, for the non-oscillatory eigenmodes, different values of tim

e to half are found, resulting in pure convergent modes, which are differentiated by the order of the times spent by the perturbations to converge.

Mode	*Eigenvalue*	*Nat. Frequency,* $\omega_n \left[rad \cdot s^{-1}\right]$	*Period,* $T\ [s]$	*Time to half,* $t_{half}\ [s]$	*Cycles to half,* $N_{half}\ [cycles]$
λ_1	-106.93858	106.93858	–	0.00648	–
λ_2	-105.49133	105.49133	–	0.00657	–
λ_3	-104.50515	104.50515	–	0.00663	–
λ_4	-104.85097	104.85097	–	0.00661	–
$\lambda_{5,6}$	$-54.79743 \pm 0.46746i$	54.79942	13.44	0.01265	0.00094
$\lambda_{7,8}$	$-54.30142 \pm 0.47923i$	54.30353	13.11	0.01276	0.00097
$\lambda_{9,10}$	$-1.3268 \pm 0.13343i$	1.33349	47.09	0.52242	0.01109
λ_{11}	0.07592	0.07592	–	9.12997	–
$\lambda_{12,13}$	$-0.69724 \pm 0.1125i$	0.70626	55.85	0.99413	0.0178
λ_{14}	-0.2291	0.2291	–	3.02552	–
λ_{15}	-0.03018	0.03018	–	22.9671	–
λ_{16}	-0.1531	0.1531	–	4.52741	–

Table 3.24: Eigenvalues from lateral-directional dynamics.

	$\boldsymbol{v}_1$		$\boldsymbol{v}_2$		$\boldsymbol{v}_3$		$\boldsymbol{v}_4$	
	Magn.	*Phase*	*Magn.*	*Phase*	*Magn.*	*Phase*	*Magn.*	*Phase*
φ_1	0.00861	0°	0.00216	180°	0.00046	180°	0.00056	180°
η_1	0.00317	0°	0.0008	180°	0.00017	180°	0.0002	180°
φ_2	0.00166	0°	0.00831	0°	0.00218	0°	0.00447	0°
η_2	0.00055	0°	0.00316	0°	0.00083	0°	0.00169	0°
φ_3	0.00024	180°	0.00217	0°	0.00705	180°	0.00671	180°
η_3	0.0002	180°	0.00074	0°	0.00281	180°	0.00271	180°
φ_4	0.0002	180°	0.00038	180°	0.00484	0°	0.00365	180°
η_4	0.00018	180°	0.00033	180°	0.00218	0°	0.00143	180°
$\dot{\varphi}_1$	0.92088	180°	0.22826	0°	0.04762	0°	0.05868	0°
$\dot{\eta}_1$	0.33906	180°	0.08396	0°	0.01756	0°	0.02148	0°
$\dot{\varphi}_2$	0.17757	180°	0.87663	180°	0.22826	180°	0.46838	180°
$\dot{\eta}_2$	0.05855	180°	0.33337	180°	0.08665	180°	0.17761	180°
$\dot{\varphi}_3$	0.02598	0°	0.2286	180°	0.737229	0°	0.70378	0°
$\dot{\eta}_3$	0.02143	0°	0.07816	180°	0.29405	0°	0.2845	0°
$\dot{\varphi}_4$	0.02152	0°	0.04004	0°	0.50568	180°	0.38263	0°
$\dot{\eta}_4$	0.0193	0°	0.03435	0°	0.22816	180°	0.14976	0°

Table 3.25: Lateral-directional eigenvectors (polar form).

The first fourth modes, whose eigenvectors are shown in Table 3.25, present φ-derivatives as their most relevant magnitudes. While the yawing component of the angular velocity for the first and second kites are respectively the dominant variables of the first and second modes, the third and

fourth ones present as dominant variable the yawing component of the angular velocity referred to the third kite. The rolling components of the angular velocity also account some importance for these four modes. The fifth an sixth modes behave similarly to ones with only three degrees of freedom, being their relevant magnitues in descend order: $\dot{\varphi}_1$, $\dot{\eta}_1$ and $\dot{\varphi}_2$. Anyway, since η-derivatives also account for certain significance, the angular variables adopt values of almost two order of magnitude smaller.

	$\boldsymbol{v}_{5,6}$		$\boldsymbol{v}_{7,8}$		$\boldsymbol{v}_{9,10}$		$\boldsymbol{v}_{11}$	
	Magn.	*Phase*	*Magn.*	*Phase*	*Magn.*	*Phase*	*Magn.*	*Phase*
φ_1	0.01334	0.49°	0.01366	180.51°	0.11775	131.27°	0.29682	180°
η_1	0.00888	1.65°	0.00923	181.56°	0.25573	346.14°	0.41303	180°
φ_2	0.00641	119.2°	0.00564	330.66°	0.31224	185.74°	0.32081	180°
η_2	0.0034	44.09°	0.00234	212.77°	0.17432	325.23°	0.42056	180°
φ_3	0.00205	200.84°	0.00121	75.5°	0.05461	55.82°	0.31129	180°
η_3	0.00283	355.82°	0.00375	174.91°	0.2848	345.62°	0.41382	180°
φ_4	0.0008	167.07°	0.00078	77.2°	0.02017	188.24°	0.22237	180°
η_4	0.00326	3.42°	0.00369	177.9°	0.26134	340.49°	0.37174	180°
$\dot{\varphi}_1$	0.73089	180°	0.74204	0°	0.15702	305.52°	0.02253	180°
$\dot{\eta}_1$	0.48672	181.16°	0.5013	1.05°	0.34102	160.4°	0.03136	180°
$\dot{\varphi}_2$	0.35125	298.71°	0.30639	150.15°	0.41637	0°	0.02436	180°
$\dot{\eta}_2$	0.1863	223.61°	0.12715	32.26°	0.23245	139.48°	0.03193	180°
$\dot{\varphi}_3$	0.11251	20.35°	0.06553	254.99°	0.07283	230.08°	0.02363	180°
$\dot{\eta}_3$	0.15507	175.33°	0.20364	354.4°	0.37978	159.88°	0.03142	180°
$\dot{\varphi}_4$	0.04375	346.58°	0.04244	256.69°	0.0269	2.5°	0.01688	180°
$\dot{\eta}_4$	0.1785	182.93°	0.20032	357.39°	0.34849	154.75°	0.02822	180°

Table 3.26: Lateral-directional eigenvectors (polar form).

The seventh mode is an oscillatory mode for which all the state variables practically present the same relevance, with the exception of φ_3, φ_4 and their derivatives, whose values are one order magnitude smaller. Although similar values are adopted by the different variables, $\dot{\varphi}_2$ results to be the most relevant one. In parallel, the nineth mode behave in a very similar way, but in this case adopting similar magnitudes for all the different variables. In this way, the most important difference between these two modes is related to the relevance adopted by the yaw angles of the third and fourth kites and their derivatives for each one.

The tenth mode is a mode in which the angular velocities in roll and yaw have not practically any relevance in the motion of the system, being the yaw and roll angles the predominant variables. This fact, however, also present some exception, as the cases of φ_3 and η_4 could be. Anyway, the dominant variable of this mode is due to the yaw angle of the last kite. The eleventh mode presents η-variables as the most relevant ones, adopting all these four similar values, at least one order of magnitude higher than the rest of state variables. From the phyisical perspective, this mode can be understood as a convergent motion in which principally the rolling component of each different kite participate. In addition, the last mode seems to behave similarly to this eleventh mode. However, this mode can be understood as a convergent motion of the last kite in its yaw

component which couples with the roll component of the previous three kites.

Finally the eighth mode represents the previously stated unsteable mode. Here the phase angles of each variable state for this feature since they have all of them the same value. Furthermore, the predomint magnitudes are the respective yaw and roll angles for each of the kites, being their derivatives insignificant variables. Essentially, the mode can be understood as a divergent motion in roll of each kite which couples with their respective yawing motion.

	$\boldsymbol{v}_{12,13}$		$\boldsymbol{v}_{14}$		$\boldsymbol{v}_{15}$		$\boldsymbol{v}_{16}$	
	Magn.	*Phase*	*Magn.*	*Phase*	*Magn.*	*Phase*	*Magn.*	*Phase*
φ_1	0.29108	128.67°	0.29368	0°	0.08256	0°	0.09133	180°
η_1	0.24843	356.47°	0.2305	180°	0.5113	0°	0.35512	0°
φ_2	0.21265	215.86°	0.14911	0°	0.05788	0°	0.1024	180°
η_2	0.28465	329.08°	0.28681	180°	0.50235	0°	0.35091	0°
φ_3	0.46504	180°	0.04705	180°	0.02306	0°	0.19716	180°
η_3	0.13808	322.37°	0.35937	180°	0.48935	0°	0.30974	0°
φ_4	0.14862	11.22°	0.75815	0°	0.00968	0°	0.75533	180°
η_4	0.37026	347.45°	0.01007	0°	0.48482	0°	0.06078	0°
$\dot{\varphi}_1$	0.20558	299.5°	0.06728	180°	0.00249	180°	0.01398	0°
$\dot{\eta}_1$	0.17546	167.3°	0.05281	0°	0.01543	180°	0.05437	180°
$\dot{\varphi}_2$	0.15019	26.69°	0.03416	180°	0.00175	180°	0.01568	0°
$\dot{\eta}_2$	0.20104	139.91°	0.06571	0°	0.01516	180°	0.05372	180°
$\dot{\varphi}_3$	0.32844	350.83°	0.01078	0°	0.0007	180°	0.03018	0°
$\dot{\eta}_3$	0.09752	133.2°	0.08233	0°	0.01477	180°	0.04742	180°
$\dot{\varphi}_4$	0.10496	182.05°	0.17369	180°	0.00029	180°	0.11564	0°
$\dot{\eta}_4$	0.2615	158.28°	0.00231	180°	0.01463	180°	0.00931	180°

Table 3.27: Lateral-directional eigenvectors (polar form).

Non-linear stability analysis close to the equilibrium state

As for the longitudinal motion analysis occurs, some of the modes obtained are redundant from other configurations, so it is decided to avoid the non-linear study of the system equations of motion when perturbed in the directions of those modes. However, in this case, three modes gain some importance.

On the one hand, the seventh and nineth oscillatory modes are evaluated since they seem to behave differently from previous analyzed modes appearing in simplier configurations. Furthermore, to deploy the non-linear analysis of these modes, allows also to assess for how the results match or not with the ones obtained from the linear approach. Differently from previous sections, in order to make brief the explanations, in this case it is decided to represent together the variables of the first and second kites and, of the third and fourth ones, respectively. Figures 3.30 and 3.31 show respectively those resultant transients. Here, one can appreciate how both modes, being oscillatory, perform as practically pure critically damped solutions. These two are obviously underdamped modes but, remembering from data collected in Table 3.24, both modes present damping ratios

near to the unity ($\zeta = 0.99$). In these figures, while the continuous lines are referred to the first and third kites respectively, the dashed lines are referred to the second and fourth ones.

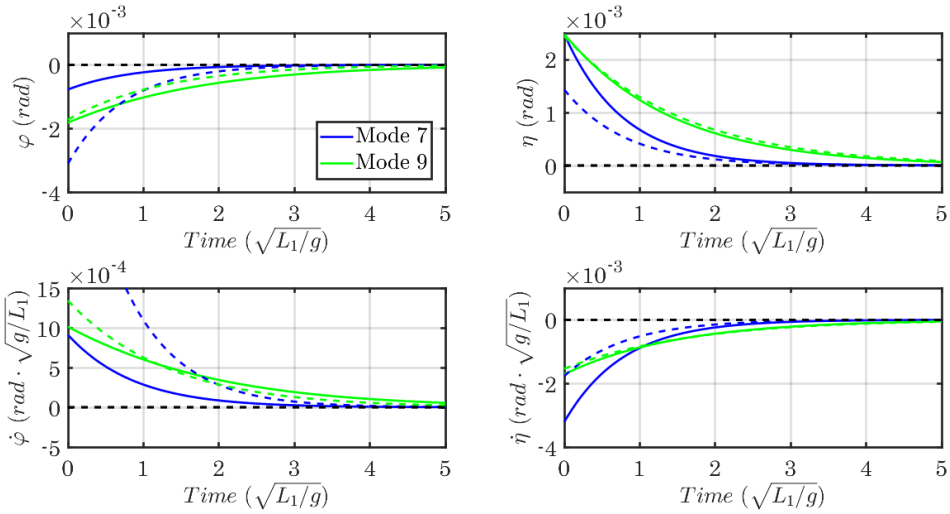

Figure 3.30: Transient disturbances of the lateral-directional state variables for the first and second kites.

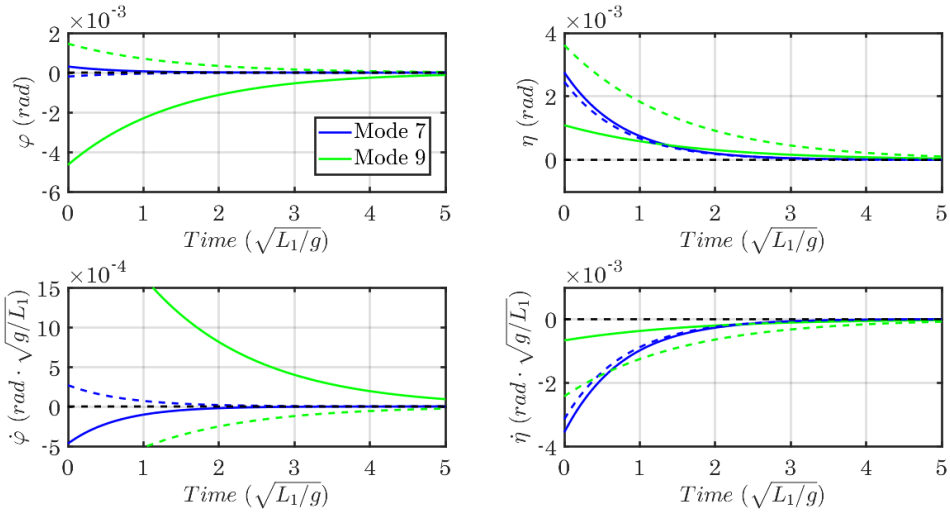

Figure 3.31: Transient disturbances of the lateral-directional state variables for the third and fourth kites.

On the other hand, the unstable mode transients are graphiclaly represented in Figure 3.32. Here, the lateral variables relative to each kite are all collected in the same figure. This fact essentially allows to determine that this mode affect in very similar ways the different kites, feature which especcially matchs with information provided when evaluating its relative eigenvector (see Table 3.26).

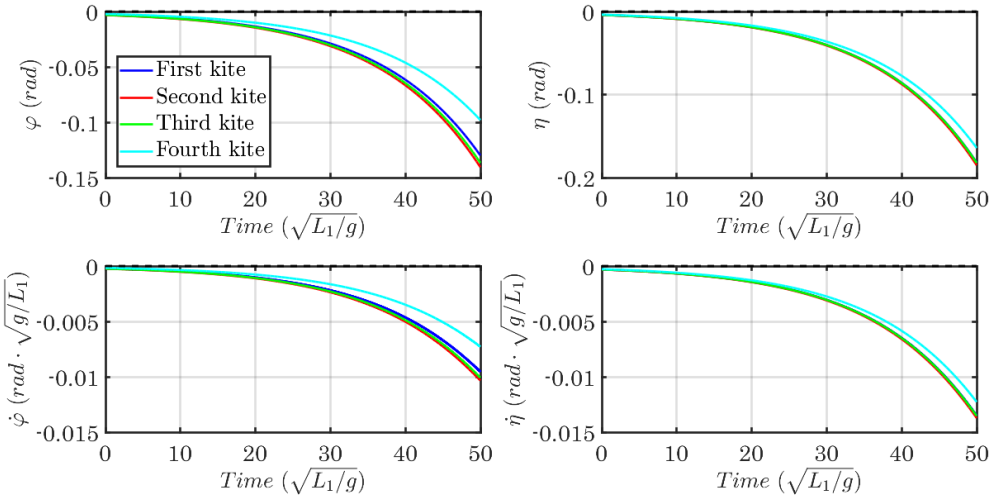

Figure 3.32: Transient disturbances of the lateral-directional state variables.

Chapter 4

Conclusions

As a summary, this section tries to collect all the conclusions which have been derived from the evaluations of the obtained results. In order to provide this work with some continuity, this section also will try to open new possible researches and investigations.

Kite Train model

The AWES model developed in Chapter 2 can be implemented for so many different rigid bodies, attached between them in a certain manner by means of two lines (as described in Section 2.1). This important aspect, allows to apply the model to many different systems.

Nevertheless, this work has been limited since only one type of lifting device has been considered. This is the case of power kites. The values selected for their geometrical aspects, stability and aerodynamic coefficients, and inertia properties, were obtained from the literature, as the real values of a power kite. Some of these parameters were changed by means of a parametric survey with the aim of getting stability for the whole systems with one and two kites. This parametric survey was performed also taking into account to maintain the order of magnitude of the different variables, and thus, the reliability of the results.

In general terms, it should be written three important statements:

- The physical model, as well as the developed MATLAB® code used for the simulations, are valid for any type of system with lifting devices which could be considered as a rigid bodies.
- The results obtained are only valid for a system using power kites as lifting devices.
- A parametric survey has been developed to get a stable equilibrium state. Although some parameters have been changed, the reliability of the results is maintained.

Equilibrium state

Physical attributes of the kites were selected to get a stable equilibrium position of the system. To get a configuration fulfilling this requirement, for the case with only one kite, it has been demonstrated that it is not a very difficult issue. The problem, however, is aggraveted when considering systems with more kites.

- Data selected only allows to obtain a stable quilibrium state for the cases with one or two kites. Systems with more than two kites, become unstable.

Normal modes

To evaluate the resultant normal modes from a general perspective is a very interesting matter. To study how the resultant modes behave when adding kites to the system, or how they are related between them following certain patterns, allow to understand the physics of the train of kites.

In general terms, some statements can be collected from the resultant eigenmodes. These are:

- In some cases, when adding kites to the train, the results incoorporate one more mode behaving in some determined way. This type of modes normally maintain their characteristics

in terms of being oscillatory or non-oscillatory ones. In other cases, the system does not present any more solution, leading to an introduction of an oscillatory mode instead of two convergent modes.

- The introduction of kites to the model, does not double the number of modes involved. Instead, modes appear following patterns, in terms of their most relevant variables and different other features.
- Any mode is not decoupled in terms of kites affected. Normally, they affect all the diffeerent kites in some determined way.
- The model assesses for the longitudinal stability of the system. Lateral instability is achieved when adding more than two kites to the train.

Longitudinal motion

The longitudinal modes from the analyses covered along this work, are represented in Table 4.1. In this table, the modes are represented written in different colors, and with a related number, depending on their performances. In this way, different colors and numbers refer for the modes which belong to the same family of modes, for which the system behaves in a determined manner. Each column collect the modes of each different configuration, being listed in the same order shown in tables where their relative eigenvalues were collected. All the modes represented in this table are stable modes.

$\mathbf{1-Kite}$	$\mathbf{2-Kite}$	$\mathbf{3-Kite}$	$\mathbf{4-Kite}$
Mode 1	Mode 1	Mode 1	Mode 1
Mode 2	Mode 3	Mode 1	Mode 1
Mode 3	Mode 2	Mode 3	Mode 3
Mode 4	Mode 5	Mode 2	Mode 3
	Mode 4	Mode 3	Mode 2
		Mode 4	Mode 5
		Mode 5	Mode 4
		Mode 4	Mode 4
			Mode 4

Table 4.1: Longitudinal modes due to the four different studied configurations.

Summarizing, the longitudinal modes of the train of kites are described as:

- Mode 1: These modes appears for the different configurations as oscillatory or non-oscillatory modes depending on the number of kites. When the system is composed by an odd number of kites, at least one mode is non-oscillatory, while the rest of them are oscillatory. In case that the train has an even number of kites, all the modes are oscillatory ones. As an example, for 1-kite configuration: $\lambda_1 = -55.21511$; for 2-kite configuration: $\lambda_{1,2} = -59.51309 \pm 8.65194i$; and for 3-kite configuration: $\lambda_{1,2} = -63.91835 \pm 11.73469i$ and $\lambda_3 = -55.19223$. From a physical perspective, these modes can be understood as very fast convergent rotational

motions of the kites around their respective $G_k x_B^k$, with their relative $\dot{\theta}_k$ as the predominant variables. The motion of the last kite is the one which governs.

- Mode 2: These modes appear in the different configurations in the same manner, being given by means of a real eigenvalue, as pure convergent solutions. From the physical meaning, the longitudinal motion of the system acts as a coupling of the two longitudinal variables, where γ_{N_k} is the dominant variable. As the number of kites increases, the importance of γ_1 is reduced. The opposite occurs for θ-variables, whose higher value is adopted always for the first kite, decreasing its value when one moves up in the train.

- Mode 3: These modes are given in a similar way to the Mode 1, being different the associated eigenvalues depending on the number of kites. For example, for 1-kite configuration: $\lambda_3 = -16.13033$; for 2-kite configuration: $\lambda_{3,4} = -14.19789 \pm 10.20032i$; for 3-kite configuration: $\lambda_{4,5} = -13.21619 \pm 11.8137i$ and $\lambda_{7,8} = -10.59361 \pm 5.02147i$; and for 4-kite configuration: $\lambda_{5,6} = -12.83483 \pm 12.41664i$, $\lambda_7 = -12.36091$, and $\lambda_{8,9} = -11.75115 \pm 5.55851i$. They present the angular velocities $\dot{\theta}$, for each different kite, as the predominant state variables. Concretely, they act as motions for which, $\dot{\theta}_2$, $\dot{\theta}_3$, $\cdots$ $\dot{\theta}_{N_k-1}$ are the dominant variables. In case with one kite, $\dot{\theta}_1$ is predominant, while for the configuration with two kites, $\dot{\theta}_1$ and $\dot{\theta}_2$ assume similar values.

- Mode 4: These modes are given by their correspondent eigenvalues, similarly to Mode 1. For example, for 1-kite configuration: $\lambda_4 = -12.28617$; for 2-kite configuration: $\lambda_{7,8} = -7.96668 \pm 3.60923i$; for 3-kite configuration: $\lambda_{9,10} = -4.61246 \pm 4.9406i$ and $\lambda_{12} = -7.65221i$. They have $\dot{\theta}_k$ as the predominant state variables. Differently from previous modes, in these ones the dominant angular velocities seems to be $\dot{\theta}_1$, $\dot{\theta}_2$, $\cdots$ $\dot{\theta}_{N_k-2}$. For the cases with one and two kites, the predominant agular velocity is the one of the first kite.

- Mode 5: These modes are all of the given by real eigenvalues. They act as coupled motions of the variables $\dot{\theta}_{N_k-1}$ and $\dot{\gamma}_{N_k}$. Moreover, in these modes, the variable $\dot{\theta}_{N_k-2}$, also present some relevance.

Lateral-directional motion

On the other hand, the lateral modes obtained for the different configurations are represented in Table 4.2. The system is, as stated, stable in lateral motion for the cases involving one or two kites. When adding more than two kites to the train, one of the modes becomes unstable, leading to the global instability of the system.

Summarizing, the lateral-directional modes of the Train of kites are described as:

- Mode 1: These colectives modes represent all of them convergent motions, being referred each one to each of the kites involved in the system. They present as dominant variable, the yaw angular velocity relative to each kite, although the respective $\dot{\eta}_k$ also adopts some relevance. For example, for 1-kite configuration, one mode exists, having $\dot{\varphi}_1$ as the dominant parameter; for 2-kite configuration, two modes appear, one governed by the motion of the first kite, and the other one, by the motion of the second kite, and so an so on. As the number of kites increases, the yaw and roll components of the angular velocity referred to the kites positioned bellow the kite which governs the motion, continue to present relevance in the mode. For cases with three and four kites, there are not any mode referred to the

$1-Kite$	$2-Kite$	$3-Kite$	$4-Kite$
Mode 1	Mode 1	Mode 1	Mode 1
Mode 2	Mode 1	Mode 1	Mode 1
Mode 3	Mode 2	Mode 1	Mode 1
Mode 3	Mode 2	Mode 2	Mode 1
	Mode 4	Mode 2	Mode 2
	Mode 5	Mode 4	Mode 2
	Mode 3	Mode 4	Mode 4
		Mode 4	Mode 3
		Mode 3	Mode 4
		Mode 3	Mode 5
		Mode 5	Mode 3
			Mode 5

Table 4.2: Lateral modes due to the four different studied configurations.

respective last kites, existing two ones in which the motion of the penultimate kite is the one which governs.

- Mode 2: These modes appear on the configurations, assiciated to the same number of eigenvalues, as number of kites is in the system. In this way, for 1-kite configuration, one eigenvector exists, $\lambda_2 = -52.40111$; for 2-kite configuration, two modes appear, $\lambda_3 = -54.089$ and $\lambda_4 = -53.36604$; for 3-kite case, three eigenvalues associated to two modes, a real negative one $\lambda_4 = -54.22995$, and a pair of conjugate complex ones $\lambda_{5,6} = -54.25194 \pm 0.4639i$; and for 4-kite configuration, two oscillatory modes, $\lambda_{5,6} = -54.79743 \pm 0.46746i$ and $\lambda_{7,8} = -54.30142 \pm 0.47923i$. All of them are coupled motions involving, in general terms, the first order derivatives of all the state angles. Principally, the motion of the first kite govers these modes.

- Mode 3: These modes appear associated to a pair of eigenvalues for all the configurations. With the exception of the 2-kite case, where an stable oscillatory mode appears, these eigenvalues are real, leading to the existance of two non-oscillatory modes. One of these modes becomes unstable for configurations with three and four kites. Anyway, they present as their predominant variables, η_1, η_2 $\cdots$, η_{N_k}, adopting all of them similar magnitudes. From the physical perspective they can be understood as motions in which the different kites rotates slowly around their longitudinal axis.

- Mode 4: These modes are not present in the configuration with one kite. They appear in the 2-kite configuration, with an unique convergent mode; for 3-kite case, with other three convergent modes; and for the 4-kite configuration, with two oscillatory modes. They present all the lateral variables with some similar importance, with the exception of φ_2, φ_3, $\cdots$, φ_{N_k} and their respective derivatives. From the physical perspective, they suposse a coupled motion of the first kite in roll and yaw, with the consequent rotational motion of the rest of kites arund their longitudinal axes.

- Mode 5: They are modes which again do not appear in the first studied case. In the rest of them, they act as pure convergent modes. For these ones, φ_{N_k} is the principal variable affecting the motion. The first-order derivatives does not present any relevance, leading to a slow convergent rotation in yaw of the last kite. All the remaining kites in the system adopt certain rotational rolling motion.

Controlability

As introduced in Chapter 1, the controlability of any AWES is a very important matter in order to get an optimal performance. The model considered is obviously a good approach, however it does not consider any control strategy.

- The results obtained covers the dynamics of the AWES for unmanned control conditions.

4.1 Future works

Regarding all the conclusions get, they propose some matters which need to be studied and evaluated in the future. They are:

- To develop a precise aerodynamic model for power kites which allow to easily obtained a correct stable model for a train with N_k kites. One of the problems that arise during the evaluation of the equilibrium of the system, has to do with the required change of some aerodynamic coefficients from the values obtained from the literature. This was performed by means of a parametric survey, due to the inexistence of an accurate aerodynamic model for power kites.
- Providing the tethers with inertia properties, aerodynamic drag and flexible effects. It has been demonstrated in previous works (see [2]), that including into the model the effect on drag, produced by the lines, helps to stabilize the system.
- Implementation of the physical model for other AWES. The introduction of other bodies as lifting devices could lead to assess for the validation of the model. Furthermore, many different configurations can be constructed to be compared with the performance of the Train of kites.
- Evaluation of the normal modes when incorporating higher number of kites to the train. Increasing the number of kites, to evaluate the patterns followed by the modes, become easier, leading to the development of a more complete analysis.
- Implementing controls to the Train of kites. To change the mechanical model of the actual lines used, by a model in which the tethers length change with time following a certain piloting law.

Bibliography

[1] Uwe Ahrens, Moritz Diehl, and Roland Schmehl. *Airborne wind energy*. Springer Science & Business Media, 2013.

[2] J Alonso-Pardo and G Sánchez-Arriaga. Kite model with bridle control for wind-power generation. *Journal of Aircraft*, 52(3):917–923, 2015.

[3] Cristina L Archer, Luca Delle Monache, and Daran L Rife. Airborne wind energy: Optimal locations and variability. *Renewable Energy*, 64:180–186, 2014.

[4] Antonello Cherubini, Andrea Papini, Rocco Vertechy, and Marco Fontana. Airborne wind energy systems: A review of the technologies. *Renewable and Sustainable Energy Reviews*, 51:1461–1476, 2015.

[5] Tarek N Dief, Uwe Fechner, Roland Schmehl, Shigeo Yoshida, Amr MM Ismaiel, and Amr M Halawa. System identification, fuzzy control, and simulation results for fixed length tether of kite power system.

[6] Ottmar Edenhofer, Ramon Pichs-Madruga, Youba Sokona, Kristin Seyboth, Patrick Matschoss, Susanne Kadner, Timm Zwickel, Patrick Eickemeier, Gerrit Hansen, Steffen Schlömer, et al. Ipcc special report on renewable energy sources and climate change mitigation. *Prepared By Working Group III of the Intergovernmental Panel on Climate Change, Cambridge University Press, Cambridge, UK*, 2011.

[7] Bernard Etkin and Lloyd Duff Reid. *Dynamics of flight: stability and control*, volume 3. Wiley New York, 1996.

[8] Lorenzo Fagiano and Mario Milanese. Airborne wind energy: an overview. In *American Control Conference (ACC), 2012*, pages 3132–3143. IEEE, 2012.

[9] Lorenzo Fagiano, Mario Milanese, and Dario Piga. Optimization of airborne wind energy generators. *International Journal of robust and nonlinear control*, 22(18):2055–2083, 2012.

[10] Uwe Fechner. *A methodology for the design of kite-power control systems*. PhD thesis, Ph. D. thesis, Delft University of Technology, 2016.

[11] Antonia V Herzog, Timothy E Lipman, and Daniel M Kammen. Renewable energy sources. *Encyclopedia of Life Support Systems (EOLSS). Forerunner Volume-'Perspectives and Overview of Life Support Systems and Sustainable Development*, 2001.

[12] Bas Lansdorp, Richard Ruiterkamp, Paul Williams, and Wubbo Ockels. Long-term laddermill modeling for site selection. In *AIAA, Modeling and Simulation Technologies Conference and Exhibit*, volume 2008, 2008.

[13] Rachel Leuthold, Sébastien Gros, and Moritz Diehl. Induction in optimal control of multiple-kite airborne wind energy systems. *IFAC-PapersOnLine*, 50(1):153–158, 2017.

[14] G Sánchez-Arriaga, M Garcia-Villalba, and R Schmehl. Modeling and dynamics of a two-line kite. *Applied Mathematical Modelling*, 47:473–486, 2017.

[15] IPCC SRREN. Renewable energy sources and climate change mitigation. *Special report of*, 2011.

[16] Michael Taylor, Kathleen Daniel, Andrei Ilas, and E Young So. Renewable power generation costs in 2014. *International Renewable Energy Agency: Masdar City, Abu Dhabi, UAE*, 2015.